MICROWAVE-ASSISTED SYNTHESIS OF II-VI SEMICONDUCTOR MICRO- AND NANOPARTICLES TOWARDS SENSOR APPLICATIONS

A Dissertation

by

RAVISH YOGESH MAJITHIA

Submitted to the Office of Graduate Studies of
Texas A&M University
in partial fulfillment of the requirements for the degree of

DOCTOR OF PHILOSOPHY

Approved by:

Chair of Committee,	Kenith E. Meissner
Committee Members,	Sarah E. Bondos
	Michael J. McShane
	Christie M. Sayes
Intercollegiate Faculty Chair,	Ibrahim Karaman

May 2013

Major Subject: Materials Science and Engineering

ABSTRACT

Engineering particles at the nanoscale demands a high degree of control over process parameters during synthesis. For nanocrystal synthesis, solution-based techniques typically include application of external convective heat. This process often leads to slow heating and allows decomposition of reagents or products over time. Microwave-assisted heating provides faster, localized heating at the molecular level with near instantaneous control over reaction parameters. In this work, microwave-assisted heating has been applied for the synthesis of II-VI semiconductor nanocrystals namely, ZnO nanopods and CdX (X = Se, Te) quantum dots (QDs). Based on factors such as size, surface functionality and charge, optical properties of such nanomaterials can be tuned for application as sensors.

ZnO is a direct bandgap semiconductor (3.37 eV) with a large exciton binding energy (60 meV) leading to photoluminescence (PL) at room temperature. A microwave-assisted hydrothermal approach allows the use of sub-5 nm ZnO zero-dimensional nanoparticles as seeds for generation of multi-legged quasi one-dimensional nanopods via heterogeneous nucleation. ZnO nanopods, having individual leg diameters of 13-15 nm and growing along the [0001] direction, can be synthesized in as little as 20 minutes. ZnO nanopods exhibit a broad defect-related PL spanning the visible range with a peak at ~615 nm. Optical sensing based on changes in intensity of the defect PL in response to external environment (e.g., humidity) is demonstrated in this work.

Microwave-assisted synthesis was also used for organometallic synthesis of CdX(ZnS) (X = Se, Te) core(shell) QDs. Optical emission of these QDs can be altered

based on their size and can be tailored to specific wavelengths. Further, QDs were incorporated in Enhanced Green-Fluorescent Protein – Ultrabithorax (EGFP-Ubx) fusion protein for the generation of macroscale composite protein fibers via hierarchal self-assembly. Variations in EGFP- Ubx·QD composite fiber surface morphology and internal QD distribution were studied with respect to

(i) time of QD addition (i.e., pre or post protein self-assembly) and

(ii) QD surface charge — negatively charged QDs with dihydrolipoic acid functionalization and positively charged QDs with polyethyleneimine coating.

Elucidating design motifs and understanding factors that impact the protein-nanoparticle interaction enables manipulation of the structure and mechanical properties of composite materials.

DEDICATION

I would like to dedicate this work to my parents and to four years of being on a roller coaster called Graduate School.

ACKNOWLEDGEMENTS

This dissertation is the product of four years of research supervised by probably the best PhD advisor a grad student can hope for. The contribution of Dr Kenith E. Meissner, my chair and my mentor, to this work and to my growth as an independent researcher has been profound. His technical advice, financial and moral support has played a big role in the completion of this dissertation. I am very grateful to have him coach me my way through grad school and shall forever be indebted to him.

I would like to acknowledge the contribution of all my committee members Drs Michael McShane, Christie Sayes and Sarah Bondos towards the completion of this work. Various portions of research undertaken in this dissertation were performed with their help and advice. I would personally like to thank all of them for their advice and help on my future career prospects.

A large portion of the experiments done as a part of this work would not have been possible without my colleagues and lab mates. I would particularly like to thank Jan Patterson and (soon to be Dr.) Sarah Ritter for the long hours spent in the lab. A shout out to all the members of the Meissner and McShane lab: Sina, Aishu, Dustin and Ashvin for their help and support during my years in grad school. I would also thank my undergrad mentee Jeffery Speich for his help with running experiments.

Additionally, I would like to thank the staff at MIC, MCF and the Dept. of Chemistry at Texas A&M, particularly Drs. Amanda Young, Yordanos Bisrat and Nattamai Bhuvanesh for their help with shared instrumentation used in this work

TABLE OF CONTENTS

Page

LIST OF FIGURES

LIST OF TABLES

1 INTRODUCTION

Semiconductors are materials whose electrical conductivities are intermediate between those of metals and insulators. A *semiconductor* can be broadly defined as a solid material with an electronic band structure consisting of a filled valence band and an empty conduction band at $T = 0$ K and an energy band-gap, E_g, greater than zero but less than about 3 to 4 eV.[1] In the past few decades, semiconductor materials have been studied extensively, finding numerous applications in modern-day electronic devices, which include transistors, diodes, thermistors, photovoltaic cells and sensors.

More recently, the advent of reliable production of *nanostructures*, defined as particles having at least one dimension below 100 nm, has opened a new frontier in materials science and engineering. The study of semiconductor nanostructures has especially garnered a lot of interest owing to potential applications in a wide range of areas, from semiconductor electronics to biomedical imaging. Applications of semiconductor nanostructures are a consequence of new physical phenomena, with regards to their optical and electronic properties, which differ considerably from their respective macroscopic counterparts.

Changes in optical or electronic properties are very evident in low-dimensional semiconductor nanostructures, such as one-dimensional (1-D) nanowires or zero-dimensional (0-D) nanoparticles. Such changes arise because the electronic wavefunctions, densities of states and energy levels in semiconductor crystals, are dependent on their physical dimensions. A three-dimensional macroscopic 'bulk' solid semiconductor crystal differs from a confined nanostructure with dimensions less than

100 nm in these respects.[1,2] For example, 0-D nanoparticles of cadmium or zinc chalcogens (AB, where A = Cd, Zn; B = O, S, Se, Te) exhibit size-tunable photoluminescence (PL) due to *quantum confinement* of electrons within the nanoparticle. Such nanostructures, which have diameters smaller than or comparable to their respective Bohr exciton radii, the average distance between an electron and a hole in the given material,[3] undergo separations of electronic energy levels in their conduction and valence bands leading to band-splitting. This situation is responsible for an increase in band-gap energies in these quantum confined nanoparticles, also known as *quantum dots (QDs)*, and leads to size-tunable PL.[4-6] Similarly, 1-D nanowires of ZnO, which possess a high ratio of surface to bulk energy states, exhibit enhanced PL[7] and piezoelectric properties[8] differing from their bulk counterparts.

Advances in technology for high precision synthesis of semiconductor nanostructures have enabled investigations for the origin of variations in the properties of semiconductor nanostructures and their applications in various fields of engineering. Numerous methodologies for synthesis of semiconductor nanostructures have been investigated in great detail in recent years with an aim to synthesize nanostructures in a controlled fashion at a large-scale while incurring low-cost. This is true for CdSe QDs[9-11] and ZnO nanowires[12-15], both of which belong to the II-VI semiconductor family. Optical and electronic properties of CdSe and ZnO nanostructures vary based on factors like size, shape, and surface functionality, in a fashion similar to other semiconductor nanostructures. Respective techniques for synthesis of CdSe QDs and ZnO nanowires aim to design nanostructures with properties which can be exploited for use in real-world

engineering applications. For example, synthesis of 1-D ZnO nanowire structures has led to research and design efforts towards their use in applications such as motion, force, chemical and UV sensors,[16-19] nanopiezo-generators,[8,20] and photovoltaic cells.[21] Similarly, carefully tuned PL properties of CdSe QDs have lent them to numerous applications in chemical and biological sensing,[22-24] optical multiplexing device design,[25] and as non-radiative probes for labeling and imaging.[26,27]

While notable advancements in synthesis of semiconductor nanostructures have been made in recent years, significant roadblocks for their wide-scale use still remain. This is especially true in the case of conventional wet-chemical or solution-based techniques used for synthesis of nanostructures. Solution-based techniques for generation of semiconductor nanostructures typically rely on chemistries which need an external source of energy for conversion of reaction precursors into product nanostructures. Such sources of heat, which usually consist of a hotplate or an oil or water bath, are slow and inefficient since they rely on convective heat transfer. In such reaction systems, the walls of the reaction vessel get hotter than the contents, resulting in decomposition of reagents or products over time. Additionally, temperature gradients which can exist in such systems, owing to reliance on convectional current for heat transfer, reduce the amount of control that can be exerted over the morphology of the product nanostructures Nanostructure morphology directly co-relates with the electrical and optical properties in case of semiconductor nanostructures and prevents large-scale production.

This dissertation seeks to introduce a microwave-assisted approach for solution-based synthesis of semiconductor nanostructures. In this study, microwave-assisted techniques have been applied for the generation of II-VI semiconductor nanocrystals, specifically, CdX (X = Se, Te) QDs and ZnO nanostructures, and have been shown to exhibit benefits in terms of control over nanostructure morphology and a shortened time of synthesis which leads to increased nanocrystal quality. Additionally, semiconductor nanostructures generated via microwave-assisted techniques have been used for design of optical sensors. Specifically this dissertation showcases the use of ZnO nanostructures for design of an optical humidity sensor. Also, design motifs for generation of a protein·QD nanocomposites, with potential optical biomolecule sensing, have been explored.

1.1 Microwave-assisted methods for colloidal synthesis

In principle, the preparations of nanoscale particles can be classified into two categories: physical and chemical techniques. Physical methods involve breakdown of bulk samples to generate nanostructures whilst chemical methods involve reaction between precursors for growth of desired nanostructures. Any process for synthesis of nanostructures requires a high degree of precision at the nanoscale and ideally should be versatile in terms of process scale-up and desirable nanostructure product variations. In addition, from a commercialization prospect, a fast processing time and low cost are always desirable. Benchtop wet-chemical techniques, while not without roadblocks, represent ver-satile approaches for synthesis of nanostructures, especially in case of the II-VI semiconductor family. Recent studies have shown applicability of organometallic

reactions for synthesis of CdSe QDs.[9-11] Similarly, hydrolysis reactions can be applied for generation of ZnO nanostructures.[13-15,17,28]

A key roadblock for nanostructure synthesis by wet-chemical approaches is the lack of accurate temperature control in thermally activated reactions, leading to variability in product nanostructure size and morphology. This stems from the typical use of convective heat to drive chemical reactions for generation of nanostructure products. While alternative approaches such as photochemical, sonochemical or electrochemical reactions exist, thermal activation for synthesis remains a favored choice owing to its versatility. A microwave-assisted heating approach circumvents the disadvantages encountered in convective reactions and is a potential tool for synthesis of II-VI semiconductor nanostructures.

The use of microwave irradiation is an efficient method for heating reaction mixtures. Microwave irradiation can heat a substance by dipole polarization and ionic conduction thereby interacting with reaction mixtures on a molecular level. At microwave frequencies, typically 2.45 GHz for laboratory equipment, energy is transferred to a reaction mixture every nanosecond. This is faster than molecular relaxation rates which typically are in order of tens of micro seconds (~10^{-5} seconds)[29]. This leads to faster and more localized heating of the reaction mixture without excess heat being supplied to the reaction vessel. Molecular heating of the reaction mixture by microwave-irradiation also permits an accelerated rate of reaction leading to shortened reaction times.[29,30] Further, temperature gradients inside a reaction mixture, which are typically encountered in convective systems, can be reduced by an adequately designed

microwave cavity, which would provide the reaction mixture with uniform microwave irradiation, potentially leading to higher product quality.

While the use of microwaves has obvious advantages, in terms of process parameter control and shorter reaction times, detailed studies showing its wide-scale applicability for synthesis of nanostructures remain to be done. Reaction parameters and design motifs for microwave-assisted nanostructure synthesis in solution-phase reactions would significantly differ from convective methods. For example, since microwaves heat a substance by dipole polarization, reaction mixtures in polar solvents, like water or alcohol, heat more rapidly than those in apolar solvents like toluene. Also, the presence of salts in reaction mixtures affects the rate of heating; mixtures with higher salt concentrations heat faster. Such effects can potentially lead to alternative reaction mechanisms unobserved in convective heating methods and can significantly affect nanostructure product morphology.

1.1.1 Single-mode microwave reactor for nanostructure synthesis

This dissertation studies the applicability of microwave-assisted heating for the generation of II-VI semiconductor nanostructures. Synthesis of semiconductor nanocrystals, namely, Cd-based QDs and ZnO nanostructures, is carried out in a single-mode microwave reactor (CEM Corp., North Carolina, USA) (Figure 1.1A). The microwave reactor consisting of a single-mode microwave cavity, created by a circular waveguide **(**Figure 1.1B), provides very uniform sample heating without any hot or cold spots **(**Figure 1.1C) that are typical for a domestic multimode microwave oven. Additionally, the single-mode microwave cavity is designed to provide a higher energy

density per unit volume of the sample allowing for an efficient preparative chemistry. The Discover® microwave reactor is also equipped with an Intellivent^{TM} pressure device which maintains and measures pressure up to 300 psi for high pressure reactions. The reactor also includes a non-contact IR temperature sensor to monitor temperatures up to 300 ^{o}C. The Discover® system can be either pre-programmed or operated dynamically, via the Synergy^{TM} software provided by the manufacturer, to control time, temperature, microwave power, and pressure for a given synthesis process. Overall the single-mode microwave reactor provides a safe and controlled environment for laboratory benchtop synthesis of nanostructures.

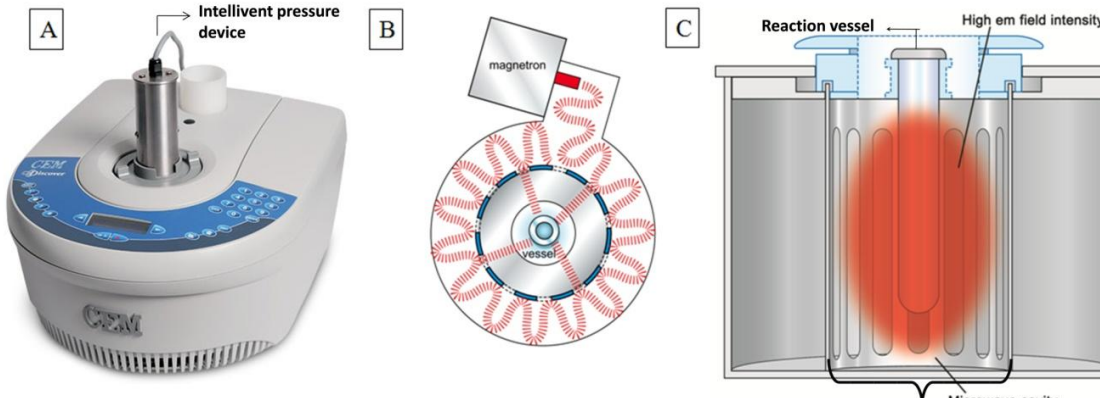

Figure 1.1 The CEM Discover® microwave reactor used in this work (A). Schematic diagram showing the top-view (B) and side-view (C) of the single-mode microwave cavity which provides high energy density microwaves for uniform heating. Illustration courtesy of CEM Corporation © 2006

1.2 Overview of the dissertation

This dissertation includes the use of microwave irradiation specifically for the generation of CdX (X = Se, Te) QDs and ZnO nanostructures. Detailed studies included

in this dissertation outline important considerations that need to be made for microwave-assisted synthesis of these II-VI semiconductors in solution-phase reaction systems. Studies involving changes in process parameters such as time, temperature, pressure and microwave power, for controlled synthesis of Cd-based QDs and ZnO micro and nanostructures, showcase the versatility of a microwave-based approach for synthesis of II-VI nanostructures. Furthermore, this study aims to demonstrate the applicability of II-VI semiconductors as platforms for optical sensing. The use of ZnO nanostructures synthesized in this work as reversible optical humidity sensors is demonstrated. Also, design motifs for an optically-active protein·QD composite fiber with potential biomolecule sensing applications have been studied.

Figure 1.2 shows a schematic flowchart outlining the goals and specific objectives of this dissertation. Chapters 2 and 3 of this dissertation discuss the application of microwave-assisted method for generation of ZnO micro and nanostructures. This includes a novel method for colloidal synthesis of 1-D ZnO nanopods by heterogeneous nucleation on 0-D ZnO nanoparticle 'seeds' in Chapter 3. Chapter 3 also demonstrates, for the first time ever, the application of ultra-small sub-20 nm ZnO nanostructures synthesized by a microwave-assisted approach as reversible optical sensors for chemical gas sensing – an important area of application for ZnO. Further, Chapter 4 describes one-pot microwave-assisted synthesis of CdSe, CdTe and CdSe(ZnS) core(shell) QDs, whose PL collectively spans the visible and NIR range of the electromagnetic spectrum. Chapter 5 discusses the application of CdSe(ZnS) QDs for generation of composite protein·QD fibers, with potential biomolecule sensing

applications, via bottom up self-assembly motifs. A final overview and potential areas for improvement of microwave-assisted synthesis of II-VI semiconductor nanostructures is presented in Chapter 6. Additional comments on specific applications for ZnO nanostructures and protein·QD composite fibers generated as part of this work are also included in Chapter 6.

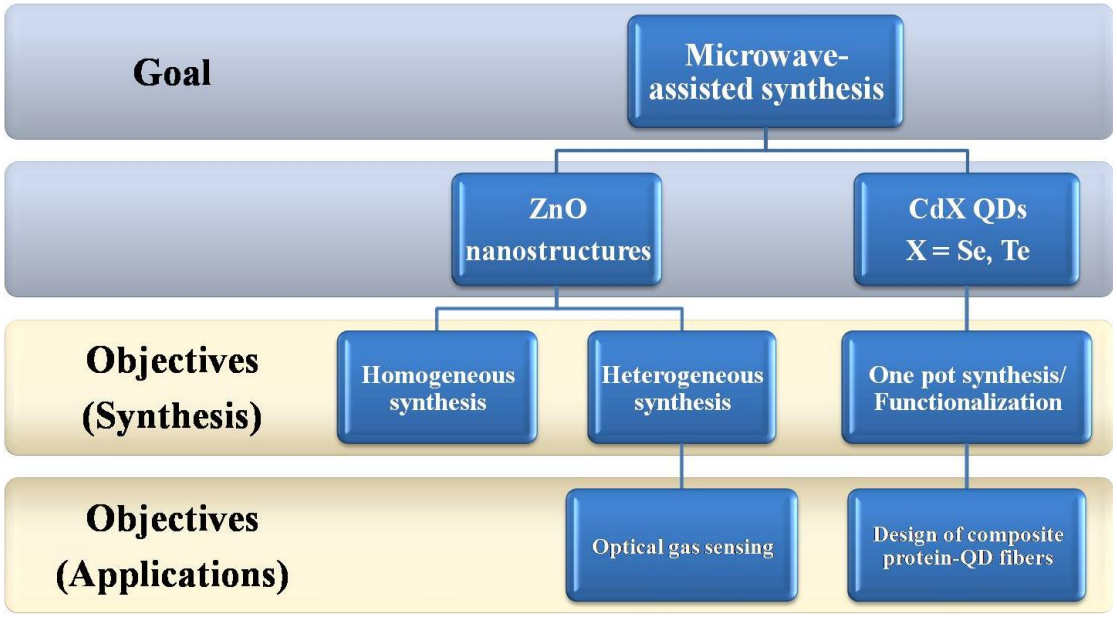

Figure 1.2 A schematic flowchart outlining the goals and objectives of this work.

2 SYNTHESIS OF ZINC OXIDE MICRO AND NANOSTRUCTURES BY A MICROWAVE-ASSISTED APPROACH

2.1 Introduction

Zinc Oxide (ZnO), a II-VI semiconductor, has a wurtzite crystal structure (Figure 2.1) with alternating planes composed of fourfold tetrahedral-coordinated O^{2-} and Zn^{2+} ions, stacked along the *c* axis. The oppositely charged ions produce positively charged (0001)-Zn and negatively charged $(000\overline{1})$-O polar surfaces, resulting in a normal dipole and spontaneous polarization along the *c* axis. The unit cell lattice constants are *a* = 3.25Å and *c* = 5.2Å with the ratio *c/a* ~ 1.60, close to the ideal value for a hexagonal cell of 1.633.

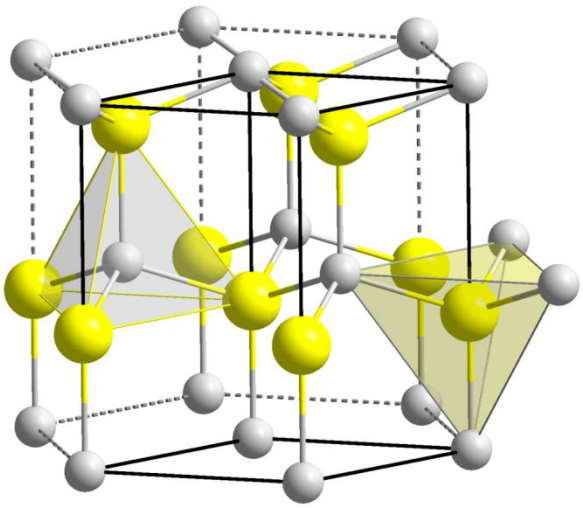

Figure 2.1 The crystal structure of ZnO (wurtzite) with coordination polyhedra.

ZnO has a very rich family of nanostructures, which includes nanorings, nanohelices, nanobows, nanopropellors, polyhedral cages, nanobelts, nanowires and nanorods.[31] Amongst these, 1-D micro and nanostructures of ZnO such as wires, rods, and belts are widely regarded as a very promising material system for a multitude of nanotechnology applications encompassing a wide range of disciplines. This interest is a consequence of the attractive intrinsic properties of ZnO: piezoelectricity, pyroelectricity, high isoelectric point, biocompatibility, a 3.37eV [~368 nm] direct band gap and a large 60 meV exciton binding energy resulting in PL at room temperature.[32-34] Such properties of ZnO have led to research and design efforts for synthesis of 1-D ZnO micro and nanostructures and advanced their application as field emission devices, energy harvesting devices,[35,36] and most notably as chemical gas sensors.[18]

Amongst various 1-D ZnO nanostructures, ones having *ultra-small dimensions,* defined as having at least one dimension less than 20 nm, are particularly interesting for engineering applications. Dimensions of ultra-small ZnO nanostructures assume particular significance with regards to their PL properties. Upon UV excitation, ZnO structures, bulk or nanoscale, exhibit two distinct PL bands.[33,37] PL in the UV region (370-390 nm), commonly referred to as near band-edge (NBE) emission, occurs due to excitonic emission whereas PL in the visible and NIR region (450-750 nm), commonly referred to as the deep-level (DL) emission, occurs due to deep-level defects in the ZnO crystal. Significant changes in PL properties are observed for 1-D ZnO having their smallest dimension ranging from 5-20 nm, i.e., ultra-small nanostructures. While still not quantum confined, ultra-small 1-D ZnO nanostructures in this size range possess a large

ratio of surface states as compared to larger nanostructures or bulk leading to alterations in their NBE and DL emissions.[38-40] While the precise role of surface states and their impact on PL of ultra-small ZnO nanostructures is still a topic of research,[34,41] the large surface area to volume ratio in ultra-small 1-D ZnO nanostructures is expected to promote device design, making engineering applications of ZnO nanostructures more viable.

2.2 Statement of problem for synthesis of ultra-small ZnO nanostructures

While ZnO nanomaterials have a host of potential engineering applications, challenges for reliable synthesis, especially in the case of ultra-small nanostructures, still remain. Issues for the generation of 1-D ultra-small ZnO nanostructures largely arise from the need for precise control over their diameters. ZnO growth is inherently anisotropic with preferential growth along the c-axis of the wurtzite crystal corresponding to the length of a 1-D nanostructure.[15] Thus generation of ultra-small ZnO nanostructures would rely on modifying inherent growth kinetics rather than simple process parameter variations, making control over the diameters more challenging.

Numerous methodologies for synthesis of ZnO micro and nanostructures have been previously studied at varying levels of detail. These methodologies can be broadly classified into two groups: (1) vapor processes such as thermal evaporation[42] and chemical vapor deposition (CVD),[43] and (2) solution-based processes[17] such aqueous hydrolysis[13-15,17,28] and electrochemical reactions.[44] Each of the above mentioned general methods has a unique set of advantages and disadvantages. Of these, solution-based methods, especially aqueous-based synthetic chemistries, are of particular interest

due to overall versatility and ease of synthesis as compared to vapor-phase methods.[15,17,28,45] Solution-based techniques offer the opportunity to synthesize ZnO micro and nanostructures colloidally. This differs from most vapor-phase techniques in which 1-D ZnO nanostructures (nanowires) grow from nucleation sites adhered onto substrates. Colloidally-generated ZnO structures are advantageous from an application standpoint such as chemical gas sensing. In sensor device design, colloidal micro and nanostructures provide more versatility in areas like tethering of the sensor element to signal readout transducers. Additionally, since colloidal structures are not physically connected to a 'growth' substrate, non-radiative pathways for carrier recombination, which are potentially detrimental to sensor response, are alleviated.

Colloidal synthesis of ZnO in aqueous solutions, which typically consists of a hydrolysis reaction with an alkali, leads to generation of ZnO microstructures.[17,46] As with other methods, growth of ZnO microstructures in aqueous methods, whether low temperature or hydrothermal, is inherently anisotropic with preferential growth along the c-axis of the wurtzite crystal.[15] Structural variation can be introduced by means of structure-directing agents such as polyethyleneimine,[15] (PEI) cetyltrimethylammonium bromide,[47] (CTAB) and ethylenediamine[48] (ED). Surfactants like PEI, CTAB and ED preferentially adsorb on certain surfaces of the ZnO crystal during growth and thereby impede or promote growth in the desired crystal directions. For example, PEI is known to promote growth along the c-axis of the wurtzite crystal, the length of a rod or wire-like structure, thereby increasing aspect ratios to ~125.[15] Such surfactants can be used to control ZnO microstructure morphology in colloidal wet-chemical techniques.

Hexamethylenetetramine (HMT), another additive, has also been widely used in aqueous synthesis of ZnO microstructures to control ZnO growth.[13-15,17,28] Unlike other additives, HMT controls ZnO crystal growth kinetically. HMT itself serves as a source of OH^- ions in solution by means of decomposition causing hydrolysis of Zn^{2+} salts to form ZnO crystals.[49,50] Thus, HMT can be used to control morphology of product ZnO microstructures using a combination of reaction parameters such as pH, temperature, precursor (Zn^{2+}) concentration, and HMT:Zn^{2+} ratio.[49]

While multiple studies have investigated colloidal generation of ZnO microstructures, generation of nanostructures remains challenging. Difficulty in synthesis of 1-D ZnO nanostructures, especially with ultra-small dimensions (sub-20 nm), arises from lack of control on the inherent anisotropic growth rates between the $< 0001 >, < 01\bar{1}0 > and < 2\bar{1}\bar{1}0 >$ growth directions. While the use of structure-directing agents like ED, which modify growth kinetics, for colloidal generation of ZnO nanorods with diameters of ~50 nm have been reported,[51] literature for colloidal generation of ZnO nanostructures is sparse and lacks a detailed design rationale.

2.2.1 Heterogeneous nucleation for colloidal synthesis of ZnO nanostructures

Heterogeneous nucleation is widely used for the generation of aligned ZnO nanowires on a variety of substrates. Zero-dimensional (0-D) ZnO nanoparticles, spin cast on a variety of substrates, such as single crystal Si or amorphous glass, can be used as nucleation sites for growth for large-scale synthesis of aligned ZnO nanowires.[14] The use of 0-D ZnO nanoparticles as ‘seeds’ for heterogeneous nucleation and growth of 1-D

nanostructures represents a unique approach for *colloidal* generation of ZnO nanostructures.

While colloidal heterogeneous nucleation seems like an obvious approach for synthesis of ZnO nanostructures, growth of 1-D ZnO nanostructures using 0-D seeds has been considered prohibitive. ZnO nanoparticles, when refluxed or heated in solution, tend to coalesce to form oligomeric chain-like aggregates.[52,53] Pacholski *et al.* demonstrated that sub-5 nm ZnO nanoparticles (seeds) can, upon refluxing for several hours, undergo an 'oriented attachment' wherein the crystal lattice planes of individual nanoparticles fuse together leading to formation of a single chain-like structure.[53] Oriented attachment leading to formation of larger aggregates is a major reaction pathway in ZnO,[53] similar to the phenomenon observed by Penn and Banfield in anatase and iron oxide nanoparticles.[54,55] This reaction pathway effectively competes with heterogeneous nucleation and growth in a reaction mixture consisting of a growth precursor solution and ZnO seeds. Formation of large aggregates in colloidal solution due to the oriented attachment of 0-D nanoparticles would deter the generation of 1-D nanostructures that are observed when seeds are physically adhered to a substrate.

2.2.2 Proposed solution and research objectives: microwave-assisted heterogeneous nucleation

Microwave-assisted heating, as emphasized in Chapter 1, is typically accompanied by reduced reaction times and accelerated rates of reaction and has potential to circumvent factors prohibiting colloidal heterogeneous nucleation. Nanostructure growth rates are expected to be very fast in microwave-assisted methods,

owing to highly localized molecular heating. This could presumably change the dynamics between the two competing mechanisms encountered in colloidal heterogeneous nucleation, that of 0-D ZnO nanoparticle oriented attachment and 1-D ZnO nanostructure growth, and promote colloidal heterogeneous nucleation.

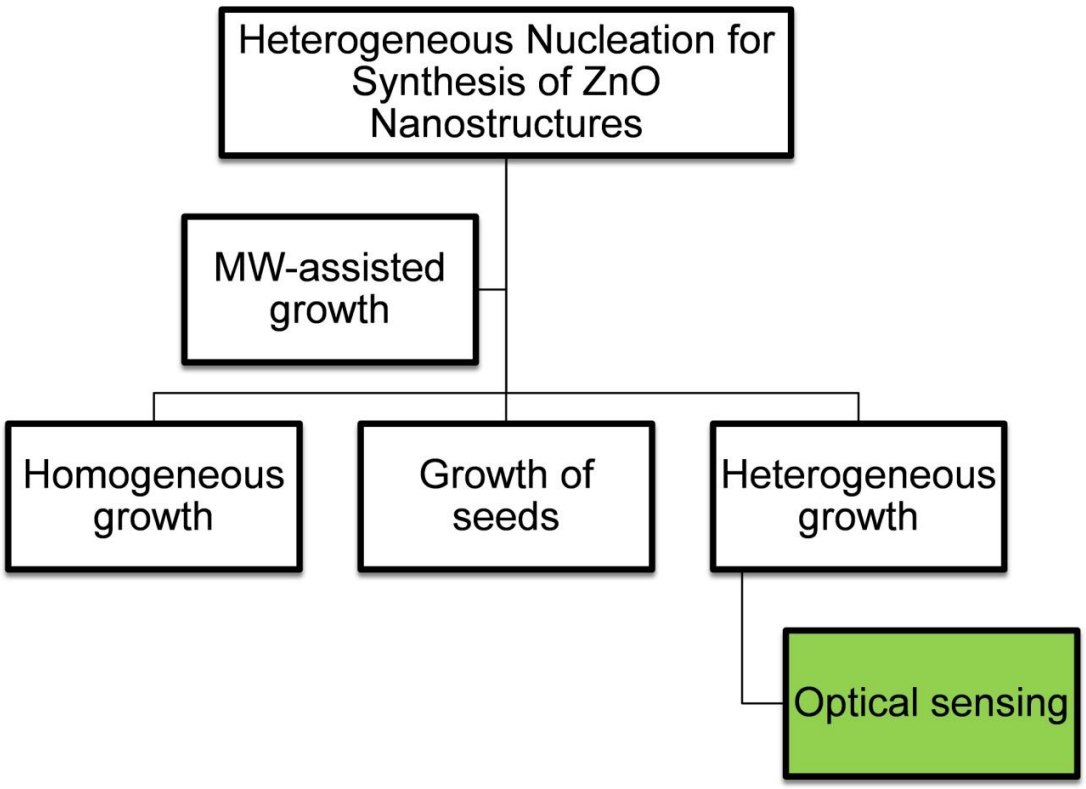

Figure 2.2 A schematic outlining goals and objectives for design and optical sensing applications with ZnO nanostructures.

This dissertation proposes the use of single-mode microwaves for the generation of ZnO nanostructures via heterogeneous nucleation. The following specific objectives, as shown in Figure 2.2, are outlined to achieve this goal:

Objective #1: Microwave-assisted homogeneous synthesis of ZnO microstructures

In this objective, ZnO microstructures will be synthesized homogeneously (i.e., without the use of nucleation seeds) using microwave-assisted heating via alkaline hydrolysis chemistry. Specifically, a reaction system consisting of Zn^{2+} salts and HMT will be studied to optimize reaction parameters for generation of ZnO microstructures in a microwave-assisted method. This reaction system was chosen because detailed literature for the generation of ZnO microstructures with Zn^{2+} salts and HMT via convective heating methods is available. However, a systematic investigation of the various factors and reaction parameters that affect ZnO crystal formation in a microwave-assisted reaction cannot be found in the literature and is desirable. Optimal reaction parameters for generation of ZnO structures, determined in this study, will be used for heterogeneous synthesis in subsequent objectives.

Objective #2: Generation of sub-5 nm ZnO nanoparticle 'seeds'

In this objective, 0-D sub-5 nm ZnO nanoparticles, to be used as seeds for colloidal heterogeneous growth of 1-D nanostructures, will be synthesized. Both convective heating and microwave-assisted heating approaches will be used for generation of ZnO seeds.

Objective #3: Colloidal heterogeneous nucleation for gas sensing applications.

An accelerated rate of reaction and consequently shorter reaction time obtained via microwave-assisted heating enables the use of otherwise inaccessible chemistries for nanoparticle synthesis. In case of ZnO, microwave heating would presumably allow the

use of nanoparticles as seeds for heterogeneous nucleation and subsequent growth of nanostructures. Such colloidal growth via heterogeneous nucleation for the synthesis of ZnO nanostructures would be studied, for the first time ever, as a part of this objective. It is expected that heterogeneous nucleation would lend itself to a high degree of control during the synthesis of ZnO nanostructures. Control over size and structural morphology of ZnO nanostructures would manifest itself in the optical properties of ZnO nanostructures. Ultra-small ZnO nanostructures generated via heterogeneous nucleation would lend themselves to optical gas sensing applications and is investigated in this objective.

2.3 Review of homogeneous synthesis of ZnO microstructures via convective methods

Colloidal homogeneous synthesis of ZnO microstructures with wet-chemical convective heating can be achieved via a numerous methodologies. The variations in methods for wet-chemical synthesis, in terms of temperature (i.e., low temperature or hydrothermal), precursor concentration, and the variety of precursors, has led to a rich family of reported ZnO microstructures.[12,17,46,49,56] In a given reaction system, various parameters play a complex and dynamic role,[57] making a coherent design rationale based on reaction mechanism and kinetics desirable. In this dissertation, synthesis of ZnO microstructures is achieved via aqueous hydrolysis using zinc nitrate hexahydrate ($Zn(NO_3)_2$) and HMT. This system was chosen for study given its wide-scale applicability for synthesis of ZnO microstructures in convectional-based systems.

Following sets of reaction occur during ZnO formation with $Zn(NO_3)_2$ and HMT:

HMT decomposes and supplies OH^- ions for reaction as so:-

$$C_6H_{12}N_4 + 6H_2O \rightarrow 6H_2CO + 4NH_3$$

$$NH_3 + H_2O \rightarrow NH_4^- + OH^-$$

Zn^{2+} ions react with the OH^- by two reversible competing mechanisms:-

$$Zn^{2+} + OH^- \leftrightarrows ZnO \downarrow + H^+$$

$$Zn^{2+} + 2OH^- \leftrightarrows Zn(OH)_2 \downarrow$$

HMT thermally decomposes into formaldehyde and ammonia and thereby serves as a slow source of OH^- ions in solution.[49,50] A controlled source of OH^- ions provided by HMT is a significant change from additives like NaOH and NH_3 which provide an instant change in pH (i.e., OH^- ion concentration) resulting in varied product morphology and reduced control over structure by means of other reaction parameters such as time and concentration.[49] HMT serves as a basic buffer in the above reaction system by controlling the source of OH^-ions and there by allows greater control over the ZnO structure.[50]

For convection systems, it has been proposed that the decomposition kinetics of HMT are pH dependent, and it has a faster rate of decomposition at an acidic pH.[49] This changes the rate of availability of OH^-ions in solution which directly affects the precipitation or the nucleation phase. Thermodynamically, a slightly acidic pH favors the presence of Zn^{2+} ions in solution,[58] which\h are in equilibrium with a ZnO precipitated phase.[58] In alkaline conditions with a pH greater than 10, $Zn(OH_4)^{2-}$ is the favored dissolved species which precipitates as $Zn(OH)_2$.[49,59]

Temperature and HMT:Zn^{2+} concentration ratios play a key role in determination of the precipitation (nucleation) phase in convectionally heated systems. McBride *et. al.* have shown that under alkaline conditions at room temperature, $Zn(NO_3)_2$ precipitates as $Zn(OH)_2$ with a wulfingite crystal structure.[56] However, even at alkaline pH, wurzite crystals of ZnO can be directly precipitated from the same solution upon heating at ~65 °C.[56] Such ZnO structures are prone to twinning: multiple lattices growing from a common junction (typically defects). It has been argued that both ZnO and $Zn(OH)_2$ phases can exist simultaneously under a given set of temperature and pH conditions.[49] At a near neutral pH and temperature of ~ 65 °C, a 1:1 ratio of HMT:Zn^{2+} will form ZnO particles via an initial precipitation of amorphous $Zn(OH)_2$. As the ratio of HMT increases, direct precipitation of wurzite ZnO crystals is favored.[59] While the exact mechanism of precipitation (nucleation) and subsequent growth of ZnO with HMT has been widely debated,[12,49,50,56,58-60] microstructure morphology obtained in a specific HMT-Zn^{2+} reaction system depends largely on whether the, ZnO precipices first or $Zn(OH)_2$ precipitates first, or whether they compete with each other.

Structural morphology of ZnO micro and nanostructures is further determined by subsequent growth mechanism and reaction kinetics. The mechanism for growth of ZnO particles in convection systems is determined, to a large extent, by the initial precipitation (nucleation) phase. In the case of direct ZnO precipitation, crystal growth is thought to occur by nanoparticle aggregation: organized growth of ZnO by assembly of nanoparticles prominently along the c-axis of the wurzite crystal.[12,49,60] In case of $Zn(OH)_2$ precipitation, ZnO is formed by the dissolution-reprecipitation of

$Zn(OH)_2$.[56,60] It is argued that combination of both mechanisms prevails in cases where both phases (i.e., ZnO and $Zn(OH)_2$) occur simultaneously.[49,60] Reaction kinetics, controlled by levels of supersaturation, can also significantly alter structural morphology obtained for a given set of parameters.[12,49] Low levels of supersaturation are favored by low temperatures (55-75 °C), and low Zn^{2+} concentrations promote heterogeneous nucleation where polyhedral crystals are formed.[49] High levels of supersaturation favored by higher Zn^{2+} concentration or high temperatures change the overall reaction kinetics to promote spherulitic structures.[49]

Given the dynamic and complex interaction between various reaction parameters, factors such as temperature, pH, time of reaction, Zn^{2+} concentration, and HMT:Zn^{2+} ratio can be used to control structure morphology.[12,49,50,56,58-62] Each of these factors, which affect the reaction mechanism and reaction kinetics, would manifest differently in a microwave-based system as compared to a convectionally heated system. A detailed study of synthesis of ZnO microstructures in a microwave-assisted process has been undertaken in subsequent sections in this chapter.

2.4 Materials, methods and design of experiments

In this work, ZnO microstructures have been synthesized in a single-mode microwave reactor, equipped with an Intellivent pressure device. An aqueous reaction mixture consisting of pure analytical reagent grade zinc nitrate hexahydrate ($Zn(NO_3)_2 \cdot 6H_2O$, 99%, Sigma-Aldrich) and HMT (hexamethylenetetramine, $C_6H_{12}N_4$, 99%, Sigma-Aldrich) was prepared. A 2 ml total reaction volume, with each precursor measured at desired concentrations, was placed in a glass vessel capable of withstanding

pressures of up to 300 psi and heated in the single-mode microwave cavity of a CEM Discover® system. Samples, after the desired heating times, were cooled using a compressed air flow around the heating vessel. The resulting product ZnO microrods were centrifuged and washed once with methanol before materials characterization.

Reaction parameters, namely, reaction time, reaction temperature, precursor concentration (Zn^{2+} salt and HMT), and precursor ratio (HMT:Zn^{2+}), as shown in Figure 2.3, have been studied in detail in subsequent sections. For each study, the effect on the structural morphology of the product ZnO microstructure was observed after varying each reaction parameter with the all other parameters being kept constant. Consequently, reaction conditions most ideally suited for generation of microstructures in a microwave-based system were determined. Scanning Electron Microscopy (SEM) including Energy Dispersive X-Ray Spectroscopy (EDS) and Powder X-Ray Diffraction (XRD) were used to study the morphology and chemical composition of ZnO microstructures.

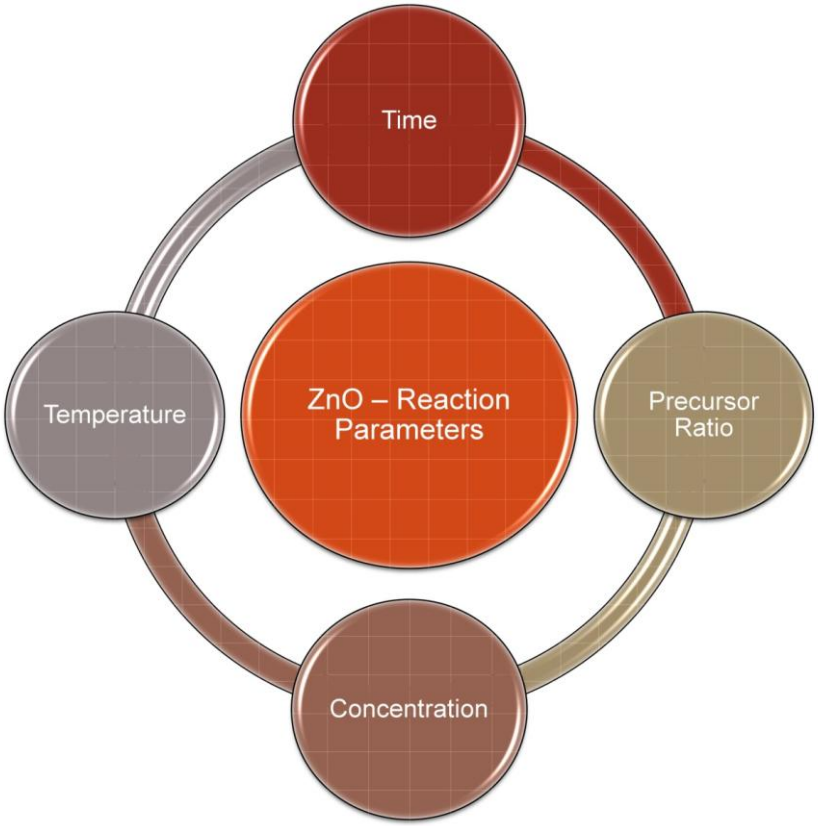

Figure 2.3 The important reaction parameters for the homogenous synthesis of ZnO microstructures studied in this work.

2.5 Effect of reaction time & temperature

A notable disadvantage with convectional colloidal aqueous methods for synthesis of ZnO microstructures is the long time scale required for synthesis, typically spanning a few hours. This is not only unfavorable for commercialization, but in conjunction with low temperatures typically used in benchtop convectional methods, long reaction times can introduce defects and thereby compromise the quality of the resulting ZnO crystals.[63] ZnO crystal synthesis can be carried out by hydrothermal

methods where, unlike low temperature synthesis, reaction is carried out at temperatures near or above the boiling point of water in a closed reaction vessel under pressure. While raising temperature has been shown to provide higher levels of supersaturation[49] and alternate structural morphologies of ZnO micro and nanostructures,[12] time required for synthesis with convectional hydrothermal method still remains fairly long.

A single-mode microwave-assisted hydrothermal synthesis approach, a high temperature aqueous solution method operated under pressure combined with single-mode microwaves for heating, can be utilized to produce high quality ZnO crystals. An accelerated rate of reaction achieved in a microwave-assisted reaction would significantly shorten the reaction time needed for synthesis of ZnO microstructures consequently producing high quality ZnO crystals. To test this hypothesis and determine the amount of time required for synthesis of ZnO microstructures in the CEM Discover® system, a time evolution experiment was conducted. For this, an aqueous equimolar reaction mixture consisting of $Zn(NO_3)_2$ and HMT was prepared with each precursor measured at 25 mM concentration. A moderate precursor concentration of 25 mM was chosen for an initial study, after consulting literature on generation of ZnO microstructures using convectional-heating, as it tends to promote the formation of rod-like microstructures.[49] The reaction mixture was heated and maintained at 170 °C for the desired amount of time ranging from 2 to 20 minutes. An initial temperature of 170 °C was chosen based on the maximum allowable safe pressure buildup in the reaction vessel. The reaction required ~100 seconds of ramping time to reach the desired set point of 170 °C. This time was not included in the hold times reported in subsequent sections.

The morphological evolution of ZnO microstructures for various times ranging from 2 to 20 minutes, synthesized under the experimental conditions described above, is shown in Figure 2.4. The following key observations can be made:

- ZnO microstructures undergo a morphological evolution over 20 minutes of reaction time. Microstructures synthesized at reaction times of 2 minutes exhibit large variations in morphology (Figure 2.4A), which includes irregular sheet-like structures and rods (Figure 2.4B) as well as tripods and tetrapods (Figure 2.4C). The variations in morphology seen in ZnO microstructures at short reaction times of 2 minutes are reduced at longer times of 10 and 20 minutes. At reaction times of 10 minutes, only tetrapods and tripods are observed, as seen in Figure 2.4D and Figure 2.4E, respectively. At reaction times of 20 minutes, a mixture containing tripods and a large proportion of rods is generated, as seen in Figure 2.4F. The ZnO microrods formed after 20 minutes of reaction time are 1.45 ±0.1 μm long and 0.38±0.06 μm in diameter.

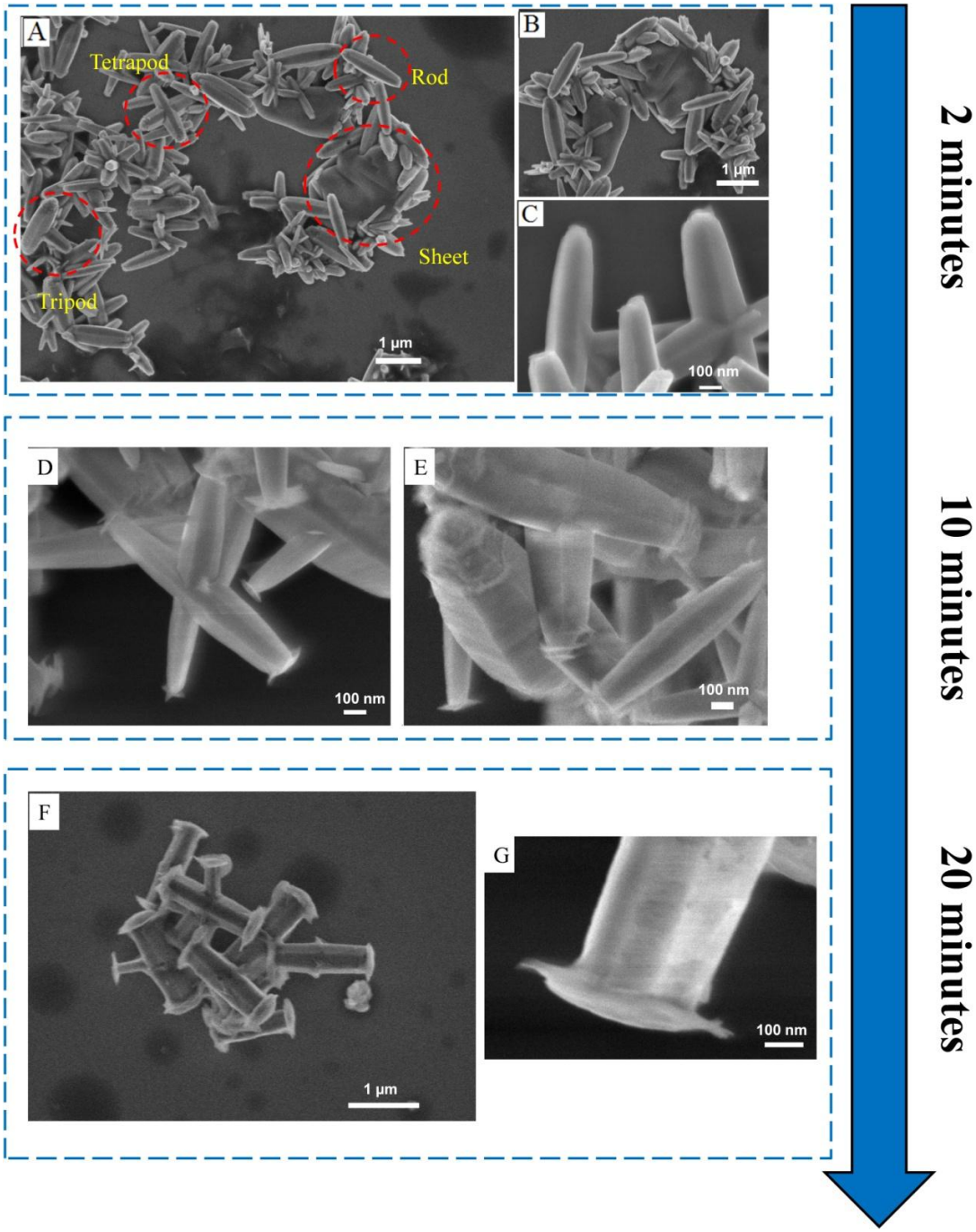

Figure 2.4 SEM images of ZnO microstructures formed hydrothermally by heating 25 mM of an equimolar mixture of HMT:Zn^{2+} at 170 °C for various times.

- The decrease in the complexity and variety of ZnO microstructures is accompanied by an initiation of cap formation along the longer axes of rods and tripods. Distinct caps perpendicular to the longest axes of rods, with diameters slightly larger than that of the rods themselves (0.5±0.08 μm), are observed on microstructures generated after 20 minutes of reaction time, as seen in Figure 2.4G. Such cap formation is gradual, and caps are not observed on tripods and tetrapods generated after 2 minutes of reaction time, as seen in Figure 2.4C. Caps are also not as well developed for structures obtained after 10 minutes of heating as they are for the ones obtained after 20 minutes.

2.5.1 Discussion of ZnO microstructure morphology

The effect of an accelerated rate of reaction in a microwave-assisted system manifests itself in the evolution of structural morphologies as seen in Figure 2.4. While a temporal evolution in microstructure morphology is commonly observed in synthesis with convectional-heating methods,[12] a drastic variation over just 20 minutes of reaction time, as is observed in this work, has not been reported. Additionally, the morphological evolution of the ZnO microstructures is accompanied by a unique, gradual cap-like formation along the longer axes of rods and tripods. Caps are not observed on microstructures during initial the phase of the reaction (Figure 2.4C) but are well developed on microstructures obtained after 20 minutes (Figure 2.4G).

SEM images using secondary and backscattered electrons, as seen in Figure 2.5A and Figure 2.5B, respectively, show a marked difference in relative contrast between the ZnO microrods (obtained after 20 minutes of heating) and the caps on their ends. In

SEM, images generated by detection of secondary electrons, which are ejected within a few nanometers from the sample surface due to inelastic scatter, show contrast based on morphological features offering high resolution. On the other hand, images generated using backscattered electrons, which originate from the volume of the sample, exhibit contrast between areas with different chemical compositions. Areas containing heavy elements with high atomic numbers generate backscattered electrons more strongly than light elements (i.e., low atomic number) and thus appear brighter on an image generated by backscattered electrons.[64] Thus, the differential contrast between the caps and microrods on the image generated using backscattered electrons (Figure 2.5B) indicates that the caps have a different chemical composition.

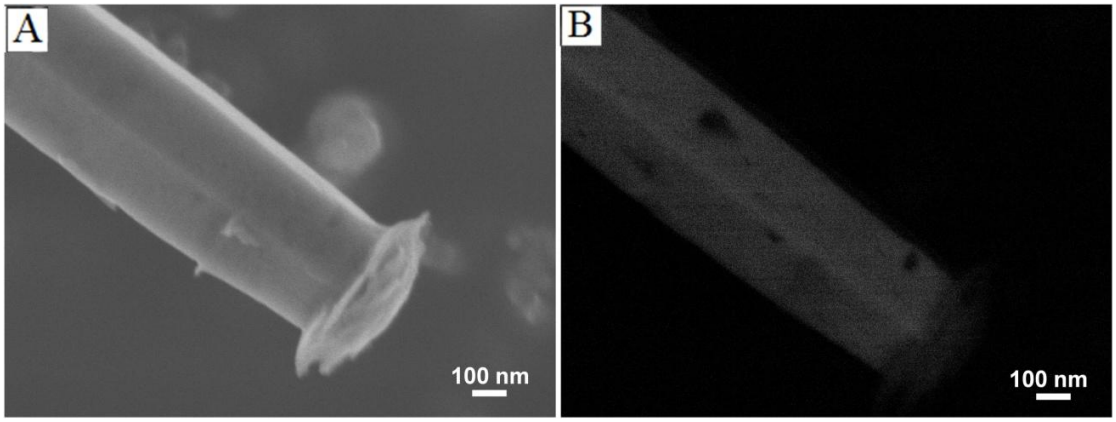

Figure 2.5 SEM images of a ZnO microrods obtained using secondary electrons (A) and backscattered electrons (B) show a difference in contrast between the microrod and the cap indicating a difference in electron density or crystal phase.

The chemical composition of ZnO microstructures, generated after 20 minutes of reaction time, were further analyzed by EDS and Powder XRD. EDS, a complementary

technique in SEM which detects energies of X-rays generated by a sample upon excitation with an electron beam, can be used for elemental analysis and mapping of the ZnO microstructures. The fundamental principle behind the characterization capabilities of EDS is that each element has a unique atomic structure allowing the emission of a unique set of X-ray energies.[64] EDS of ZnO microstructures generated at 20 minutes of reaction time qualitatively shows the presence of trace amounts of Si inside the ZnO microstructures, as seen in Figure 2.6. The peak corresponding to carbon, seen in Figure 2.6, is attributed to the carbon tape used during sample preparation. A quantitative analysis and elemental mapping of the ZnO microrods is challenging owing to the low resolution (~1 μm) of the EDS detector in the JEOL JSM-7500 FE-SEM used in this work. EDS can also be performed in conjunction with transmission electron microscopy (TEM) and would typically offer better resolution for elemental mapping. However, TEM is not feasible for microstructures with diameters greater than 100 nm.

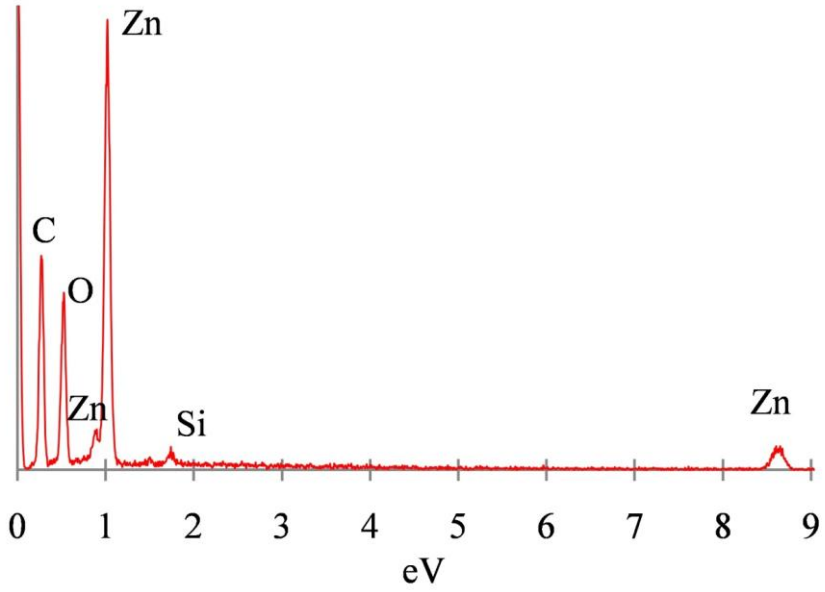

Figure 2.6 An EDS spectrum for ZnO microstructures generated at 20 minutes of reaction time showing presence of Si in caps of ZnO microstructures.

Powder XRD of ZnO microstructures confirms the presence of Si in ZnO microstructures generated at 20 minutes of reaction time. Powder XRD fingerprinting, used in this work, can provide information about crystal structure and chemical composition of the desired sample.[64] For XRD measurements, a Bruker D8 Bragg-Brentano diffractometer (CuKα radiation; 40 kV, 40 mA) fitted with LynxEYE detector was used for data collection. Diffraction data was collected from 10° - 70° 2θ with a 0.015° step size. Figure 2.7 shows powder XRD patterns for samples obtained after different times of heating at 170 °C. ZnO microstructures obtained after 2 and 10 minutes of reaction time can be indexed to wurzite ZnO (JCPDS # 01-079-2205) (Figure 2.7A and Figure 2.7B, respectively). However, microstructures obtained after 20 minutes

of heating have peaks corresponding to hydrated zinc silicate hydroxide ($Zn_2Si_2O_7 \cdot H_2O$) (JCPDS# 01-075-1320) in addition to wurzite ZnO. (Figure 2.7C)

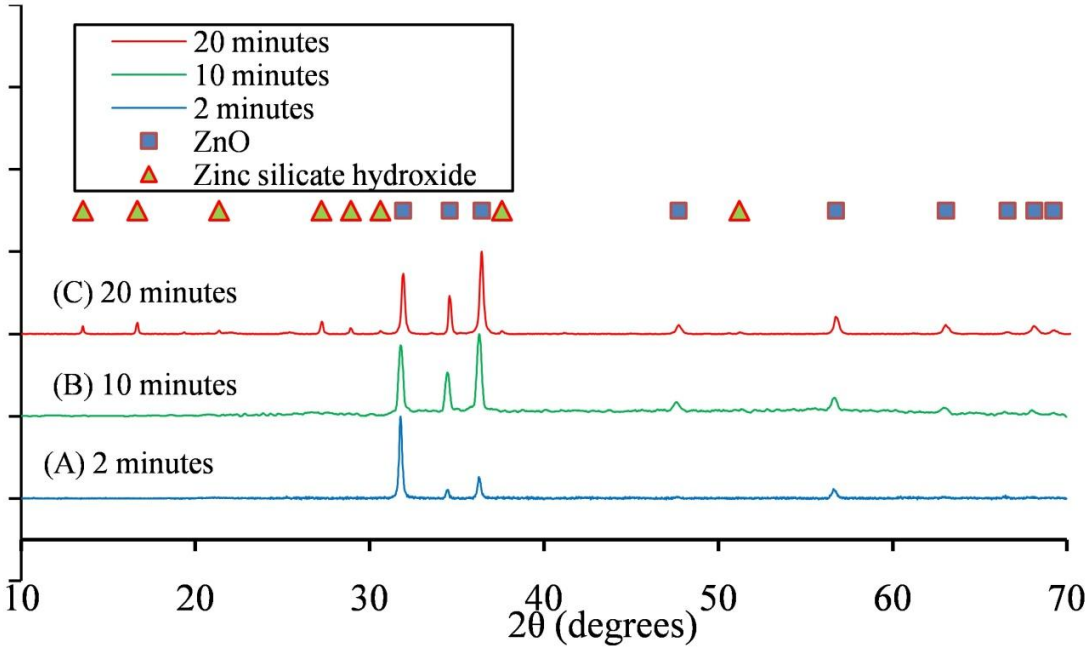

Figure 2.7 Powder XRD plots of ZnO microparticles generated with microwaves for a period of (A) 2, (B) 10, and (C) 20 minutes.

2.5.2 Mechanism of ZnO microstructure generation

In convectional-heating methods, the growth mechanism for ZnO microstructures is determined by the initial precipitation (nucleation) phase. In case of direct ZnO precipitation, which is to be expected in a system consisting of an equimolar mixture of HMT and $Zn(NO_3)_2$ heated to a temperature of 170 °C [49], crystal growth is thought to occur by nanoparticle aggregation: organized growth of the ZnO crystal by assembly of nanoparticles prominently along the c-axis of the wurzite crystal.[12,49,60]

Consistent with this, on a HMT-Zn^{2+} system under neutral pH conditions and hydrothermal parameters, Vergès *et al.* have reported evidence showing that ZnO nanoparticles attach amongst themselves to form large microstructures over time.[51] The tripod and tetrapod microstructures observed in various samples at all time points of the reaction in this work typically occur in ZnO microstructures generated by direct ZnO precipitation. Direct ZnO precipitation from an aqueous solution promotes twinning, growth of multiple lattices from a common junction with individual crystals growing along their c-axes tetrahedral to each other,[56] and leads to generation of tripod and tetrapod microstructures repeatedly observed during the various stages of the reaction.

For convectional-heated chemical baths, Govender *et al.* have reported the presence of a kinetically-controlled dissolution-recrystallization ripening process which follows the nucleation and growth during later stages of a solution-phase reaction.[17] Such a phase, considered to be as a part of a ripening mechanism occurring due to consumption of initial reagents, occurs via dissolution of ZnO crystal back in the solution as $Zn(OH)_2$ which subsequently recrystallizes to form new 1-D ZnO microrods. The morphological evolution of ZnO microstructures observed in Figure 2.4, leading to generation of a high proportion of ZnO microrods, could be attributed to an accelerated cyclic dissolution-recrystallization process made possible by localized molecular heating of the reaction mixture in the microwave cavity.

Further evidence for a dissolution-recrystallization mechanism comes from the presence of Zn silicates in the caps of ZnO microstructures, seen in samples after 20

minutes of microwave heating. Zinc silicate hydroxide (a.k.a. hemimorphite) can form by the action of $Si(OH)_4$ on $Zn(OH)_2$ as follows: [62,65]

$$Zn(OH)_2 + Si(OH)_4 \rightarrow Zn_2Si_2O_7 \cdot H_2O \downarrow$$

The glass test tubes used for heating Zn^{2+} and HMT precursors in the single-mode microwave cavity in the CEM Discover® system used here can serve as a source of $Si(OH)_4$ up to 900 ppm (8.3 mM) at 200°C.[66,67] Thus, a gradual formation of caps seen on rods and tripods could be due to a reaction between the $Si(OH)_4$ impurities and $Zn(OH)_2$ which is formed due to the dissolution-recrystallization process. Ideally, the formation of such zinc silicates is undesirable and can be avoided by using lower reaction temperatures. Figure 2.8 shows ZnO microrods and tripods generated by a 25 mM equimolar mixture of $Zn(NO_3)_2$ and HMT at 100 °C. At this temperature, $Si(OH)_4$ concentration should be less than 500 ppm (4.6 mM) which should reduce or eliminate cap formation, as observed in Figure 2.8. The formation of zinc silicate hydroxide during the later stages of the reaction at higher temperatures of 170 °C serves as a marker to indicate the presence of $Zn(OH)_2$ and provides evidence for the dissolution-recrystallization mechanism

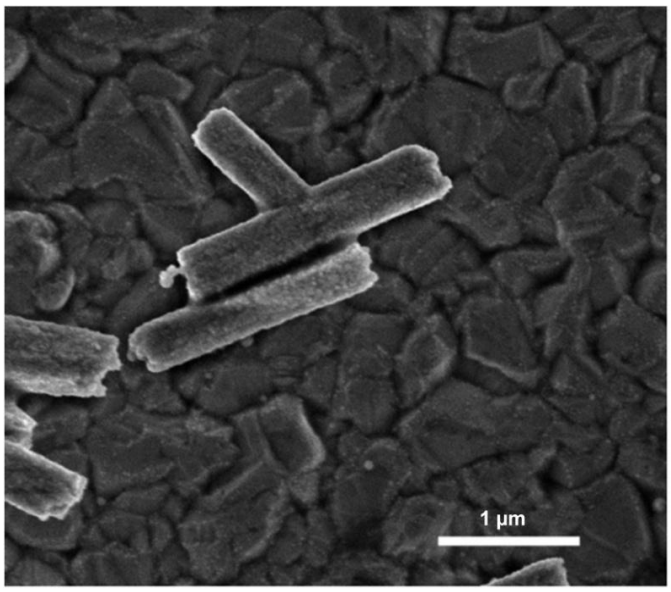

Figure 2.8 SEM image of ZnO microstructures synthesized by 25 mM equimolar mixture of $Zn(NO_3)_2$ and HMT at 100 °C for a period of 20 minutes.

Figure 2.9 shows a schematic representing the growth mechanism that occurs in the microwave-assisted hydrothermal process for synthesis of ZnO microstructures. Twinned ZnO microstructures, in the form of tetrapods and tripods, are initially formed by direct ZnO precipitation. Subsequently, ZnO microstructures undergo a reversible dissolution and recrystallization process via formation of $Zn(OH)_2$, leading to formation of 1-D ZnO microrods. In the system discussed here, irreversible formation of zinc silicate hydroxide effectively competes with and consequently disallows the recrystallization process from $Zn(OH)_2$ to ZnO. Therefore, if the reaction were to proceed for a long duration of time, all ZnO microstructures should convert to zinc silicates via $Zn(OH)_2$ formation. This conversion indeed happens when the reaction is

allowed to continue for a period of 3 hours. At 3 hours all ZnO microstructures are converted into films, as observed in Figure 2.10A, which consist of zinc silicates, as confirmed by EDS shown in Figure 2.10B.

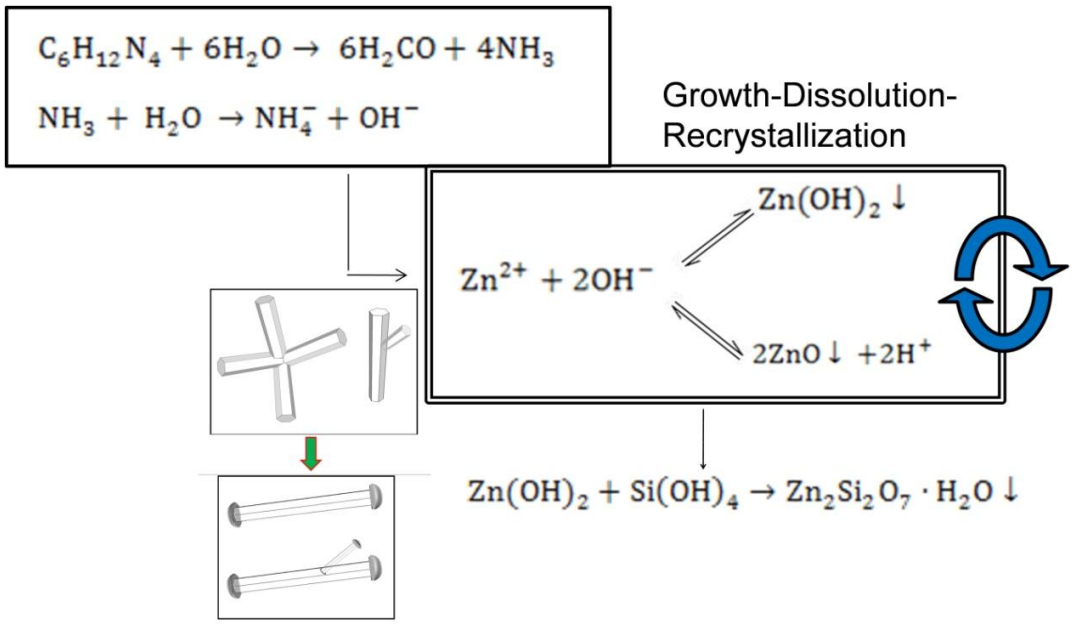

Figure 2.9 A schematic diagram showing the reaction mechanism of generation of ZnO microstructures generated by microwave-assisted heating.

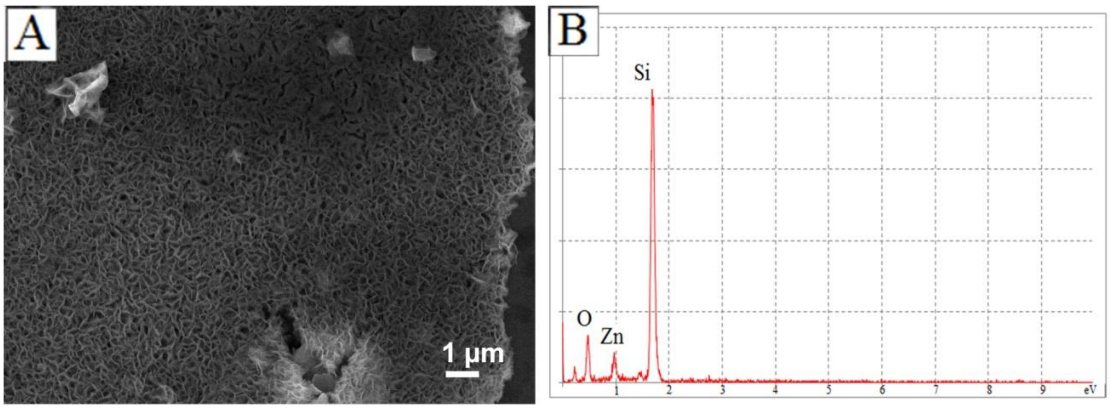

Figure 2.10 SEM image of zinc silicate films generated after a period of 3 hours with microwave-assisted heating.(A) EDS confirms the chemical composition of the films. (B)

2.6 Effect of precursor concentration

The study of ZnO microstructures generated at hydrothermal conditions, 170 °C, and equimolar concentrations of $Zn(NO_3)_2$ and HMT precursors was performed for different concentrations ranging from 10 to 100 mM. Reactions were carried out for a period of 20 minutes as they yield larger proportions 1-D rod-like structures. ZnO microrods with lengths of 1.36 ± 0.13 µm and diameters of 0.28 ± 0.06 µm were observed in the lower precursor concentration of 10 mM, as observed in Figure 2.11A. Tripods seen in the samples synthesized at 25 mM Zn^{2+} concentration were not seen at the lower concentration of 10 mM. At higher precursor concentrations of 100 mM, complex spherulitic structures were observed (Figure 2.11B). In convectional-heating systems, ZnO is known to have a tendency to form spherulitic structures at high levels of supersaturation favored by high Zn^{2+} concentrations (>40 mM).[49] This trend is

consistent with microstructures generated in microwave-assisted methods as observed in Figure 2.11.

It is interesting to note the occurrence of zinc silicate caps relative to changes in precursor concentration. At 10 mM precursor concentrations, ZnO microrods have caps perpendicular to their longest axes, similar to the 25 mM samples, along with rings along their longest edges (Figure 2.11A, marked in red). However, caps associated with microstructures at lower Zn^{2+} concentrations are not seen for microstructures generated at 100 mM concentration (at 20 minutes of reaction time). Absence of caps for high Zn^{2+} concentration samples can be possibly explained by the lower relative concentration of $Si(OH)_4$ in this case.

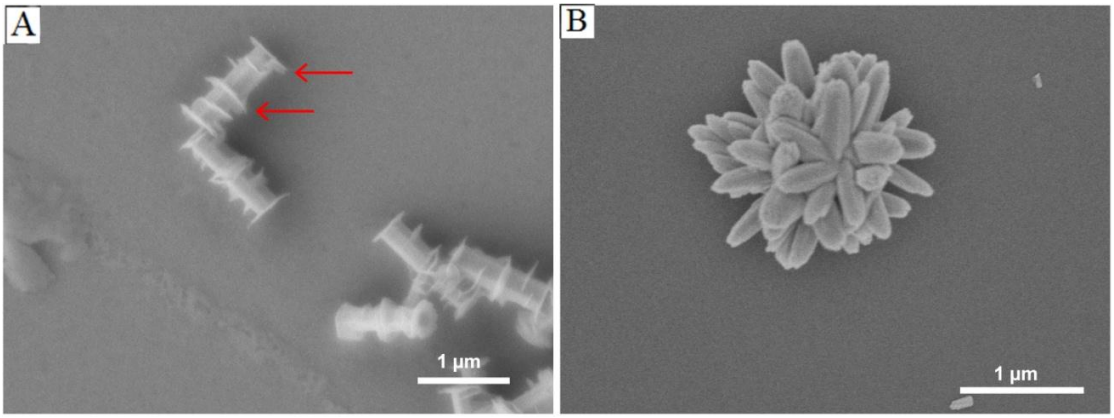

Figure 2.11 ZnO microstructures formed by hydrothermal treatment of an equimolar mixture of $Zn(NO_3)_2$ and HMT at 170 ^{0}C for a period of 20 minutes at concentrations of 10 mM (A) and 100 mM (B). Red arrows show zinc silicate rings formed on ZnO microstructures.

2.7 Effect of precursor (HMT:Zn^{2+}) ratio

As noted earlier in section 2.3, under experimental conditions of near neutral pH as is the case in this work, the ratio of HMT:Zn^{2+} plays a significant role in determining ZnO microstructure morphology.[49] At equimolar concentrations and low temperatures (<100 °C), ZnO is formed via an initial precipitation phase of $Zn(OH)_2$.[59] Increasing HMT concentration increases the amount of OH^- ions in solution but reduces the rate of availability due to screening effects. This results in a higher initial ZnO precipitation.[59] The effect of changing the HMT:Zn^{2+} ratio has been explored in hydrothermal experimental conditions employed in this work via microwave heating. Zn^{2+} concentration was kept constant at 25 mM while varying the concentration of HMT. ZnO microstructure morphology was observed after 20 minutes of reaction time.

A mixture of micron-sized rods and tripods was observed for all ratios at 25 mM Zn^{2+} concentration. The lengths, rod diameters, and cap diameters were measured for the 1-D rods as shown in Table 2.1. Decreasing the HMT concentration to 12.5 mM (thereby decreasing the HMT: Zn^{2+} ratio to 0.5) significantly increases the length of microrods to 2.37 ± 0.17 μm as compared to an equimolar ratio. Rod diameters also become larger at 0.44 ± 0.04 μm for microrods generated at an HMT:Zn^{2+} ratio of 0.5. The aspect ratio (length/diameter) of microrods generated at lower HMT:Zn^{2+} ratios varies very little, from 5.3 for a ratio of 0.5 to 3.81 for an equimolar ratio. Zinc silicate caps perpendicular to the longest axis of rods also become larger, at 0.72 ±0.08 μm with a decrease in HMT concentration. An increase in HMT concentration to 50 mM (HMT:Zn^{2+} ratio of 2) has exactly the opposite effect, in that microrod length and diameters decrease. However, the

magnitude of dimensional change from microrods generated at equimolar, in this case, is less than that observed for HMT:Zn^{2+} ratio of 0.5.

Ratio (HMT:Zn^{2+})	HMT conc. (mM)	Length (µm)	Rod Diameter (µm)	Cap Diameter (µm)
2	50	1.4 ± 0.15	0.35 ± 0.08	0.43 ± 0.09
1	25	1.45 ± 0.1	0.38 ± 0.06	0.5 ± 0.08
0.5	12.5	2.37 ± 0.17	0.44 ± 0.04	0.72 ± 0.08

Table 2.1 Dimensions of microrods generated after 20 minutes of microwave-heating with varying ratios of HMT:Zn^{2+} at 170 °C. Concentration of $Zn(NO_3)_2$ salt is kept constant at 25 mM.

Varying the HMT:Zn^{2+} ratio changes the pH of the reaction mixture. The initial pH of the reaction mixture, before heating, decreases from 7 to 6.5 by decreasing HMT concentration in solution from 50 mM to 12.5 mM. Reactions carried out at a slightly acidic pH of 6.5, obtained by decreasing HMT concentration to 12.5 mM, increases the length and cap diameter of ZnO microrods considerably. Larger caps, resulting due to increased generation of zinc silicates, indicate a higher concentration of $Zn(OH)_2$ formed during structural evolution of microstructures by the dissolution-recrystallization mechanism. The recrystallization of $Zn(OH)_2$ back to ZnO crystals would favor axial growth along the c-axis of the wurzite ZnO, resulting in longer microrods. Thus, lower HMT:Zn^{2+} ratios help in generation of longer 1-D rods, as observed in this work. An increase in the length of the ZnO rods however, does not translate into an increase in aspect ratio. An attempt to generate ZnO nanowires, defined as structures having an

aspect ratio of greater than 10, was unsuccessful even upon further reduction of the HMT:Zn^{2+} ratio. There is a lower limit to the concentration of HMT that can be used for reliable microrod generation. No crystalline microstructures were observed below ratios of 0.2, or 5 mM of HMT when 25 mM Zn^{2+} was used.

2.7.1 Effect of precursor ratios at different concentrations

The effect of varying the HMT:Zn^{2+} ratio was also studied at a lower overall concentration of Zn^{2+} salts of 10 mM. This study was undertaken to verify that the longer ZnO microrods observed at 12.5 mM HMT and 25 mM $Zn(NO_3)_2$ are indeed due to a lower HMT:Zn^{2+} ratio of 0.5, and not just a function of low HMT concentration in the reaction mixture. Lengths of microrods generated at HMT:Zn^{2+} ratios of 0.5, 1 and 5 (i.e., 5, 10, and 50 mM HMT with $Zn(NO_3)_2$ kept constant at 10 mM) were measured. Lengths of microrods increase with decreasing ratio of HMT:Zn^{2+}. As shown in Figure 2.12, ZnO microrod length increases from 1.1 ± 0.34 μm at a HMT:Zn^{2+} of 5 to 2.52 ± 0.58 μm at a ratio of 0.5. This trend is similar to the one observed for 25 mM Zn^{2+} salt concentration, indicating that the ratio of HMT:Zn^{2+} is the driving force behind variation in microrod length.

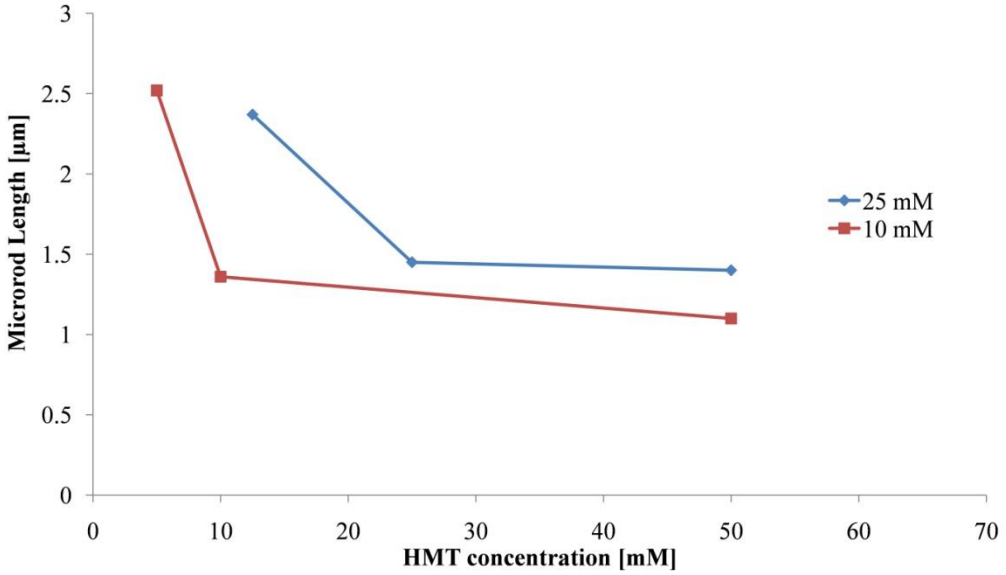

Figure 2.12 Variation in ZnO microrod length with change in HMT concentration (HMT:Zn^{2+} ratio) at 25 mM (blue) and 10 mM (red) $Zn(NO_3)_2$ concentrations. HMT:Zn^{2+} ratios of 0.5, 1, 2 and 5 were chosen for this study.

2.8 Lessons learnt from homogeneous synthesis of ZnO microstructures

In this chapter, synthesis of high quality ZnO microstructures by means of a microwave-assisted hydrothermal process is demonstrated, and the reaction mechanism for the growth of ZnO microstructures is analyzed. An accelerated rate of reaction obtained using microwaves lends to a morphological evolution of ZnO microstructures in a very short reaction time span. Similar to a convectional-heated system, a dissolution-recrystallization mechanism dictates the generation of 1-D ZnO microrods (and tripods) via formation of $Zn(OH)_2$. Results presented in this work also show presence of zinc silicate caps on ZnO microstructures. In the current system, longer reaction times could be used for the synthesis of nanofilms of hemimorphite (zinc

silicate hydroxide), a material with interesting optoelectronic properties.[65] The generation of zinc silicates can be avoided at lower temperatures (~100 °C). However, high-quality faceted ZnO microstructures were generated only at higher temperatures of 170 °C. Detailed studies on precursor concentration and precursor ratio show that a lower HMT:Zn^{2+} ratio tends to generate longer and larger diameter microstructures.

Reaction parameters for generation of ZnO structures via heterogeneous nucleation were determined based on the studies carried out so with homogeneous synthesis of microstructures. An equimolar HMT:Zn^{2+} precursor ratio at 25 mM precursor concentration was determined as the initial starting point for generation of ZnO structures via heterogeneous nucleation. A high reaction temperature of 170 °C, was chosen owing to generation of high quality crystals at that temperature. Additionally, the generation of impurities in the form of zinc silicates imposes an upper limit on the reaction time at around 20 minutes.

3 COLLOIDAL SYNTHESIS OF ZINC OXIDE NANOSTRUCUTRES VIA HETEROGENOUS NUCLEATION FOR OPTICAL SENSING

Colloidal synthesis of ZnO nanostructures is challenging owing to the inherent growth anisotropy of ZnO. In homogeneous aqueous synthesis methods, ZnO structures tend to generate microstructures as observed in Chapter 2. Generation of 1-D ZnO nanostructures would require modification of the inherent nucleation or crystal growth kinetics. Reports in the literature have shown that structural variation in the ZnO micro and nanostructures can be introduced by means of structure-directing agents such as PEI,[15] CTAB, [47] and ED[48,68]. While such structure-directing agents have been shown to affect growth kinetics, generation of ultra-small 1-D ZnO nanostructures, defined as having at least one dimension below 20 nm, remains challenging for solution-phase methods.

3.1 Background

The study of colloidal synthesis of ultra-small ZnO nanostructures is of interest from two key aspects. Firstly, nanostructures generated colloidally, as opposed to being adhered on a substrate when generated via vapor-phase processes like chemical vapor deposition,[43] offer more versatility in terms of device design for subsequent engineering applications. This is most evident in the design of chemical gas sensors, a potential area of application for ZnO nanostructures. ZnO micro or nanostructures suspended in solution can be readily spin-cast or dried in desired amounts on a sensor readout element to generate reliable devices. The properties of such a sensor device would solely depend on the sensing mechanism of ZnO structures and not be affected by the substrate. ZnO

nanostructures that grow from nucleation sites on a substrate, as is the case with all vapor transport processes[42,43] and non-colloidal wet-chemical approaches,[13-15,46] are provided with non-radiative pathways for carrier recombination. This is detrimental to sensitivity and consequently disfavors the use of ZnO nanostructures as materials for chemical gas sensing.

Secondly, dimensions of ultra-small ZnO nanostructures assume significance with regards to their physicochemical properties. Ultra-small sub-20 nm ZnO nanostructures have a high surface area to volume ratio. The ratio of surface area to volume for a 15 nm diameter nanorod is ~17 times that of a 250 nm microrod, most commonly observed in homogeneous synthesis in chapter 2. A higher surface to volume ratio correlates to a larger ratio of surface states to bulk (volume) states and particularly affects the PL properties of ZnO.

3.1.1 Effect of size on PL of ZnO

Upon UV photoexcitation, ZnO structures, bulk or nanoscale, exhibit two distinct PL bands.[33,37] PL in the UV region (370-390 nm), commonly referred to as near band-edge (NBE) emission, occurs due to excitonic emission whereas PL in the visible and NIR regions (450-750 nm), commonly referred to as the deep-level (DL) emission, occurs due to deep-level defects in the ZnO crystal. For study of PL properties, ZnO nanostructures can be divided into three regimes according to their smallest dimensions, namely, a) sub-10 nm, b) between 10-20 nm, and c) above 20 nm.

The Bohr exciton radius for ZnO is reported to be ~2.34 nm.[69] Sub-10 nm ZnO nanostructures approaching the Bohr exciton radius (category a) are known to exhibit

quantum confinement effects.[70-72] Multiple reports have shown a blue-shift in the NBE PL of sub-10 nm ZnO nanostructures with respect to bulk (smallest dimension above 20 nm, category c), indicating quantum confinement effects in ZnO nanostructures in that size regime.[70,71,73] While nanostructures in the 10-20 nm size regime (category b) are not quantum confined, they have been explicitly shown to have an effect on the NBE PL of ZnO nanostructures.[38,39] A key feature of NBE PL in ZnO, collected at temperatures ~4 K, is the presence of an asymmetric surface excitonic (SX) band which peaks at ~3.367 eV (368.2 nm). The SX band, sometimes also referred to as the I2 peak according to the Meyer Notation,[74] features a long tail below 3.367 eV and has been assigned to an event related to an exciton binding to surface-related states.[38,39,75,76] In addition to the SX band, two more peaks at 3.36 eV (I6, 369 nm) and 3.357 eV (I9, 369.3 nm) are commonly observed over the broad tail of the SX band in the NBE PL of ZnO at low excitation intensities. The I6 and I9 peaks are attributed to recombination from neutral donor-bound excitons and are collectively referred to as D^0X peaks.[38,39,75,76]There is ample evidence in literature that the SX band becomes more dominant with respect to I6 and I9 D^0X peaks as the dimension of the nanostructures reduces.[38,39,41] The SX band broadens at lower energies for ultra-small nanostructures (i.e.,: sub-20 nm including categories b and c as defined above), thereby becoming the most dominant feature of the NBE PL of ZnO nanostructures when collected at low temperatures.[41]

A large ratio of surface states to bulk (volume) states also affects the visible DL emission in ZnO nanostructures. The nature and origin of visible PL in ZnO

nanostructures is more complex than the NBE PL. Various reports have shown that the visible PL for ZnO spans almost the entire visible spectrum.[33,37] Visible PL in ZnO is commonly attributed to the recombination of an electron-hole pair from defect localized states (typically associated with the surface) with energy levels deep in the band gap, resulting in lower energy emission. The chemical nature of these DL emissions is widely debated in the literature and is still a topic of research.[33,34,37,77] However, given the co-relation of such DL emission to surface defects, changes in the visible PL are to be expected for ultra-small nanostructures of ZnO.

3.1.2 Generation of ZnO nanostructures via heterogeneous nucleation

Interest in the generation and study of ultra-small ZnO nanostructures originates from their potential applications and novel optical properties as discussed above. However, as aforementioned, there are very few reports available in the literature on the generation of such nanostructures, especially using colloidal solution-phase approaches. One notable study by Liu *et al.* reports on the generation of quasi 1-D nanostructures with diameters in 10-30 nm range by varying ratios of ethylenediamine, a structure-directing agent, and Zn precursors.[68] However, the methodology reported by Liu *et al.* for generation of ZnO nanostructures exhibits very little control over morphology and necessitates very long reaction times, anywhere between 1 and 12 days, for generation of ZnO nanostructures.

Multiple studies have demonstrated solution-phase growth of 1-D ZnO nanostructures adhered onto substrates via heterogeneous nucleation using sub-5 nm ZnO nanoparticles as seeds.[13-15,46] In this, ZnO nanowires grow along the c-axis of the

wurzite crystal on substrates containing 0-D ZnO seeds by consumption of Zn precursors present in the growth solution surrounding the substrate. However, the use of such 0-D seeds in solution for colloidal synthesis of ZnO nanostructures is considered to be prohibitive (see section 2.2). Previous attempts to use sub-5 nm seeds for colloidal generation of ZnO nanostructures using convectional heating by Chen *et al.* resulted in generation of a mixture of micro and nanostructures with very little control over diameters of the generated structures.[78]

As described earlier in section 2.2, microwave-assisted heating is a potential tool for colloidal generation of ZnO nanostructures via heterogeneous nucleation. An ultra-short reaction time for nucleation and fast crystal growth, as already observed during homogeneous synthesis of ZnO microstructures in chapter 2 could potentially allow the generation of ultra-small ZnO nanostructures during microwave-assisted heating. This hypothesis for generation of ZnO nanostructures is explored in subsequent sections. For this, sub 5-nm ZnO seeds are synthesized, using both convectional and microwave-assisted approaches. The seeds are subsequently used in a reaction mixture containing a growth solution, a mixture of Zn^{2+} salt and HMT, and heated in a single-mode microwave cavity in the CEM Discover® system. Reaction conditions and parameters used for generation of ZnO nanostructures are similar to the ones studied for homogeneous synthesis in chapter 2.

3.2 Generation of 0-D ZnO seeds

Numerous methodologies for the synthesis of ZnO seeds, sub-5 nm 0-D nanoparticles, are available in the literature. Literature for generation and study of opto-

electronic properties of ZnO nanoparticles can be traced back to the seminal reports by Bahnemann *et al.* outlining chemistries for generation of 0-D ZnO nanoparticles.[52] Synthesis methodologies by Bahnemann *et al.*, which include a method for precipitation of ZnO by rapid alkaline hydrolysis that was further modified by Spanhel *et al*[79] and Hasse *et al*,[80] are the basis of ZnO nanoparticle synthesis in this work. In the following sections, two different approaches for the synthesis of sub-5 nm ZnO nanoparticles have been employed. This includes a standard convectional-heating methodology, as outlined in the literature, and a modified microwave-assisted approach. Additionally, the ZnO nanoparticles are quantitatively characterized for size by use of their optical properties.

3.2.1 Size determination of ZnO nanoparticles by optical absorption

Quantum confinement in semiconductor nanostructures, resulting due to excitons being physically squeezed into dimensions approaching the electron wavefunction, is typically associated with an enhancment in the bandgap consequently leading to changes in the optical properties of the nanostructures as compared to the bulk. Quantum confinement effects have been reported in ZnO nanostructures having dimensions below 10 nm, approaching the Bohr exciton radius of 2.34 nm. [70,71,73] Quantum confined ZnO nanostructures exhibit a blue-shift in their NBE PL when compared to bulk. A corresponding blue-shift in the onset of absorbance, due to band-gap enhancement, is also observed for quantum confined ZnO nanostructures. For monodisperse samples, the position of the absorption onset can be used for determination of particle size using the effective mass model estimation as previously reported by Searsonet *et al*.[71,72]

The shape of the absorption edge, for a direct band gap semiconductor like ZnO, is solely due to the electronic transition from the top of the valence band to the bottom of the conduction band.[2] The absorption coefficient, α, is given by

$$\boldsymbol{\alpha = \frac{C(h\nu - E_g^{bulk})}{h\nu}}$$

Equation 3.1

where C is a constant, hν is the photon energy, and E_g^{bulk} is the bulk bandgap of ZnO(3.37 eV or 368 nm). However, for quantum confined nanostructures, the band-gap is larger than E_g^{bulk} and can be modeled as a function of nanoparticle radius, r, as so:

$$\boldsymbol{E^* = E_g^{bulk} + \frac{\hbar^2 \Pi^2}{2er^2}\left(\frac{1}{m_e m_0} + \frac{1}{m_h m_0}\right) - \frac{1.8e}{4\Pi\epsilon\epsilon_0 r}}$$

Equation 3.2

Where E^* the the band-gap pf the nanoparticle in eV, m_e and m_h are the effective mass of the electron and the hole respectively, m_0 is the free electron mass, ϵ is the relative permittivity, ϵ_0 is the permittivity of free space,ħ is the reduced Planck's constant, and e is the charge on an electron. Assuming $\lambda_{onset} = hc/E^*$, a relationship between absorption onset and nanoparticle diameter can be obtained. Since the effective masses for the electrons and holes in ZnO are relatively small (m_e = 0.26, m_h = 0.59),[71] band-gap enlargements and the corresponding blue-shift in absorption onset wavelength can be observed for particle radii of less than 4 nm. Figure 3.1 shows estimated values of

absorption onset (in nm) for ZnO nanoparticles as a function of their radii, exhibiting the expected blue-shift of absorption onset from the bulk value of 368 nm.*

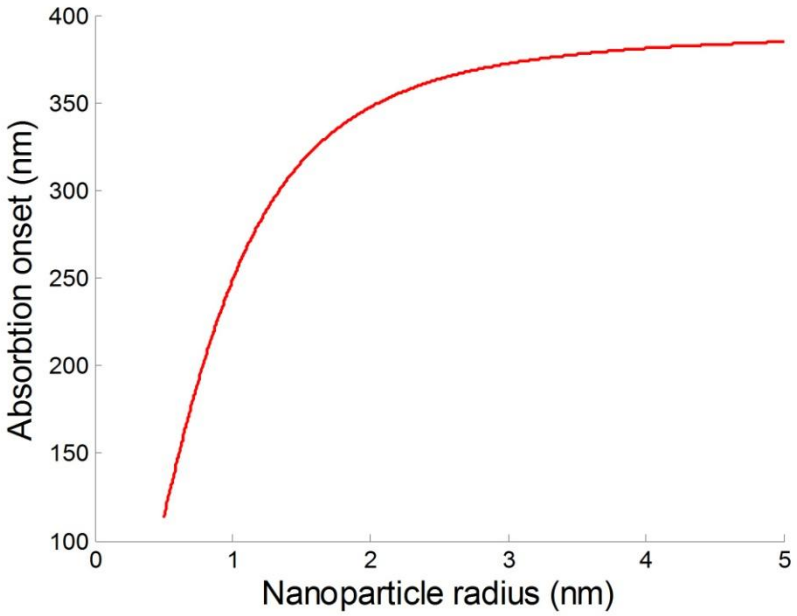

Figure 3.1 Effective mass model calculations showing the relationship between absorption onset and nanoparticle radius for quantum confined ZnO nanoparticle.

3.2.2 Materials and methods: synthesis of ZnO nanoparticles via convectional heating

ZnO nanoparticles (seeds), to be used in a subsequent reaction mixture for colloidal heterogeneous nucleation, were synthesized via standard convectional-heating by alkaline hydrolysis of Zn^{2+} precursor using a modified procedure originally reported by Hasse *et al*.[80] For this, 125 ml of 10 mM zinc acetate solution ($Zn(CH_3COO)_2 \cdot 2H_2O$, >98%, Sigma-Aldrich) in methanol was hydrolyzed by quick addition of 65 ml

* Estimated ZnO nanoparticle radii vis-à-vis absorption onset values can be found in Appendix A

of 30 mM NaOH while stirring vigorously. The reaction mixture was then refluxed at ~60 °C, on a hot plate, for a period of 2 hours.

ZnO seeds, synthesized as above, were imaged via TEM using a JEOL 1200 microscope operated at a 100 kV acceleration voltage. TEM images, as shown in Figure 3.2A, indicate that spherical ZnO nanoparticles were generated by the hydrolysis reaction. Figure 3.2B shows the particle size distribution, as observed by TEM. ZnO nanoparticles are 4.1±0.8 nm in diameter. Also, High Resolution TEM (HR-TEM) images taken using a FEI Technai F20 operated at 200 kV, shown in Figure 3.2 inset, indicate that the ZnO nanoparticles are single wurzite crystals

PL and UV-visible absorbance measurements were also carried out on the ZnO seeds for size determination. PL measurements were carried out with a PTI QuantaMaster™ having a Xe Arc lamp excitation at 315 nm. ZnO seeds show NBE emission centered at 360 nm accompanied by a broad green DL emission, as shown in Figure 3.3 (red). The NBE emission from the seeds is blue-shifted as compared to the bulk bandgap for ZnO (3.37 eV or 368 nm), indicating presence of quantum confinement effects. UV-visible absorption measurements (Hitachi U-4100) show a first exciton peak at 341 nm supporting the existence of quantum confinement effects in the ZnO seeds. (Figure 3.3, blue) Based on effective mass model calculations (Figure 3.1), the absorption onset of ~365 nm observed in UV-Visible absorption measurements corresponds to particle diameter of ~4.2 nm, which agrees closely with TEM measurements.

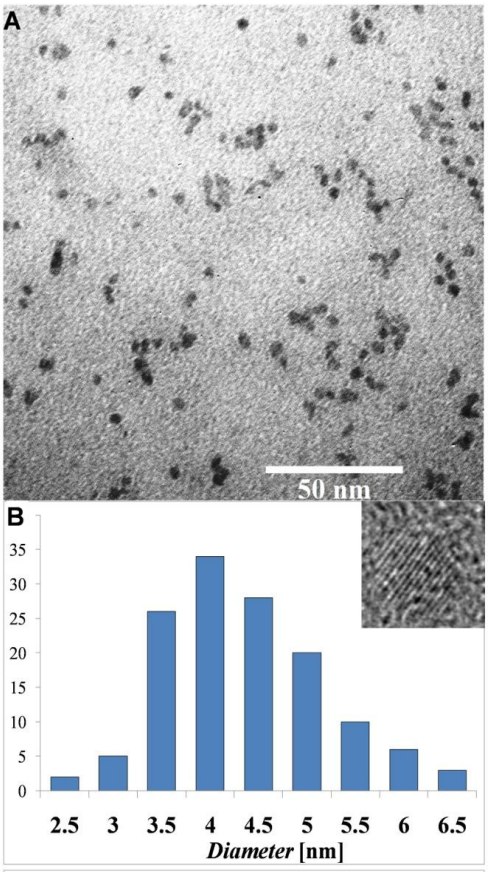

Figure 3.2 TEM image of ZnO nanoparticles used used for colloidal heterogeneous synthesis. (A) Size distribution of ZnO nanoparticles with an average diameter of 4.1 ±0.8 nm. (B) HR-TEM image showing a single ZnO nanoparticle. (B, inset)

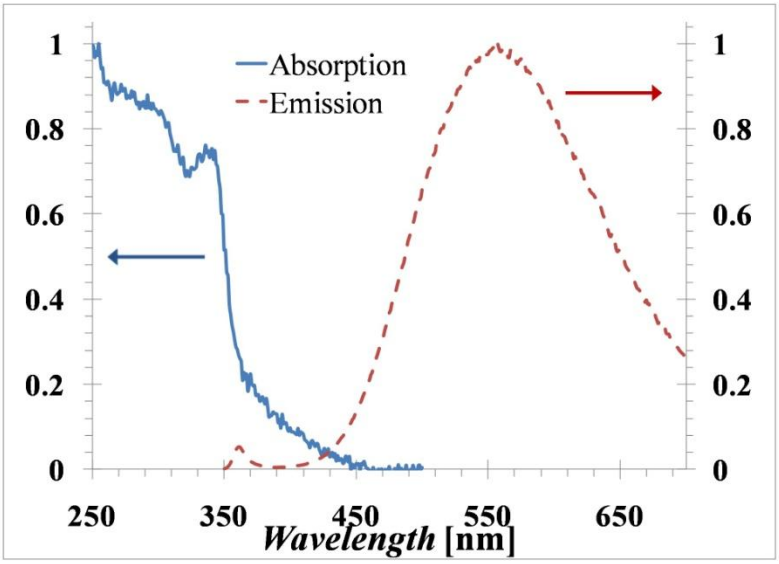

Figure 3.3 UV-visible absorption (blue) and PL spectra (red) of ZnO seeds generated via convectional-heating.

3.2.3 Materials and methods: synthesis of ZnO nanoparticles via microwave-assisted heating

A modified alkaline hydrolysis approach using microwave-assisted heating was also used for the generation of 0-D ZnO seeds. For this, 13 ml of 30 mM NaOH was quickly injected into 25 ml of 10 mM zinc acetate solution in methanol, initially chilled to 4 °C, and heated rapidly to 60 °C in a single-mode microwave cavity. The reaction mixture was refluxed for varying amounts of time ranging from 3.5 minutes to 20 minutes. Figure 3.4 shows the UV-visible absorbance measurements for ZnO seed samples generated at various time points. After 3.5 minutes of refluxing, ZnO seeds with an absorption onset of 331 nm were generated. This, according to the effective mass

model (Figure 3.1), corresponds to a size of ~3.4 nm in diameter.[†] A slight enlargement of seed diameter is observed with an increase in reflux time. After 10 and 20 minutes of reflux, ZnO seeds with an absorption onset of 338 nm and 345 nm, respectively, are generated (Figure 3.4). These correspond to diameters of ~3.6 nm and ~3.9 nm, respectively. The microwave-assisted approach thus offers high precision size-tunability for generation of ZnO seed nanoparticles. However, an attempt to generate nanoparticles (seeds) with even smaller diameters with identical recipes at lower reflux times was unsuccessful. At reflux times shorter than 3.5 minutes, Zn^{2+} salts are not completely hydrolyzed, as evidenced by a highly scattering milky white reaction mixture. Variation in precursor concentration or use of a different solvent could potentially be used to generate smaller ZnO nanoparticles using microwave-assisted approach and remains for future studies.

[†] Estimated nanoparticle radii values for various absorption onset can be found in Appendix A

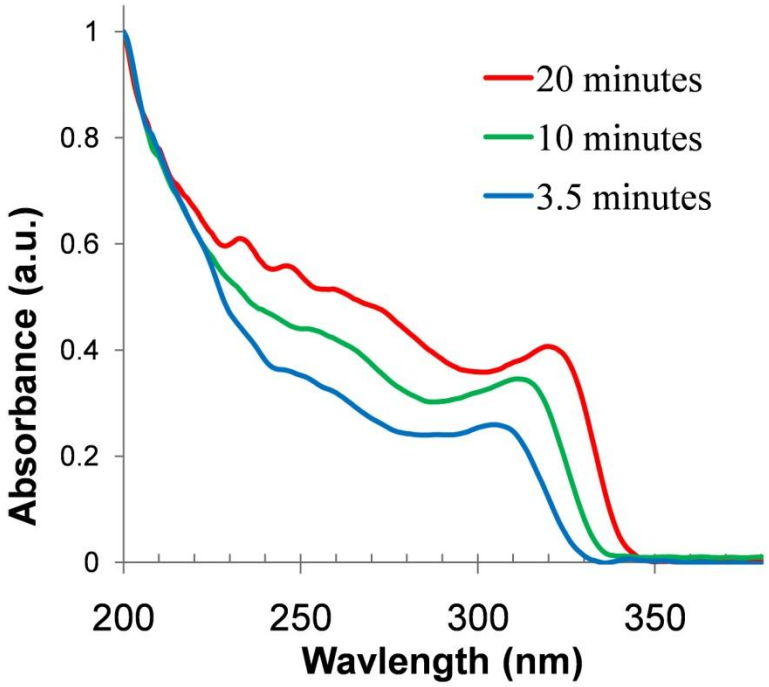

Figure 3.4 UV-Visible absorption spectra for ZnO seeds generated via microwave-assisted heating.

3.3 Generation of ZnO nanostructures via heterogeneous nucleation

3.3.1 Experimental method for generation of ZnO nanostructures

For generation of ZnO nanostructures via heterogeneous nucleation, an aqueous reaction mixture consisting of a precursor growth solution and ~4 nm ZnO seeds, synthesized by convectional heating as outlined in the preceding section, was heated to hydrothermal conditions by microwave-irradiation in a single-mode microwave cavity of a CEM Discover® system. Reaction parameters for generation of nanostructures were determined by studies performed for homogeneous synthesis of ZnO microstructures. Specifically, the precursor growth solution used for generation of nanostructures

consisted of an aqueous equimolar mixture of $Zn(NO_3)_2$ and HMT at concentration of 25 mM. A 2 ml volume of the growth mixture was mixed with 100 µL of 4 nm ZnO seeds, at 2.9 µM concentration. The mixture was vortexed for a period of 30 seconds and heated to 170 °C in a 10 ml glass test tube under 100-150 psi of pressure. The reaction mixture required 50 to 60 seconds to reach the set point temperature of 170 °C where it was held for varying times from 2 to 20 minutes, as desired. The reaction mixture was subsequently cooled rapidly by flowing cold air into the microwave cavity. ZnO nanostructures generated in the reaction mixture were centrifuged and washed in methanol before materials characterization.

3.3.2 Nanostructure characterization

SEM images of ZnO nanostructures generated in the reaction mixture heated to hydrothermal conditions at 170 °C for a period of 20 minutes are shown in Figure 3.5. ZnO nanopods, multi-legged structures with ultra-small individual leg diameters, of 15.44 ± 1.89 nm, are generated in the reaction. SEM images indicate that ZnO nanopods consist of a varying number of legs with up to 5 individual legs isolated on a single nanopod, as shown in Figure 3.5B. Individual legs of the nanopod have lengths of 250-300 nm, giving them a fairly large aspect ratio in the range of 15-20. It is interesting to note the absence of any cap-like aggregates on the ends of individual legs of the nanopods, as were observed for microstructures during homogeneous synthesis in absence of ZnO seeds, generated after 20 minutes of reaction time at temperatures of 170 °C.

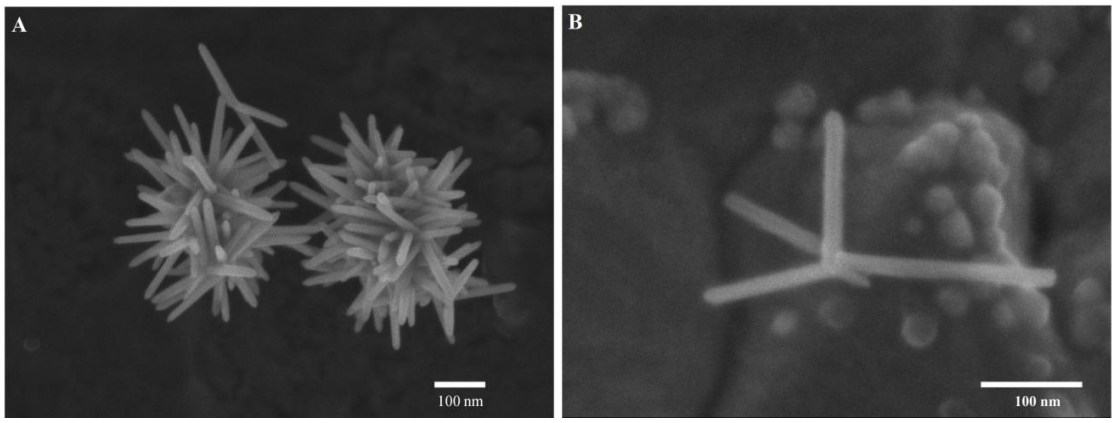

Figure 3.5 A SEM image of a cluster of ZnO nanostructures generated by heterogeneous nucleation on ZnO seeds. (A) An individual five-legged nanostructure. (B)

Powder XRD studies were performed on ZnO nanopods to analyze the crystallinity of the structures. For XRD measurements, a Bruker-AXS D8 Advanced Bragg-Brentano geometry X-ray Powder Diffractometer (CuKα radiation; 40 kV, 40 mA) fitted with LynxEYE detector was used. A XRD pattern of the ZnO nanopods, shown in Figure 3.6, can be indexed to the wurzite ZnO phase (JCPDS # 01-079-2205), as expected. No peaks for zinc silicates were observed for nanopods generated after 20 minutes, consistent with the lack of caps on SEM images.

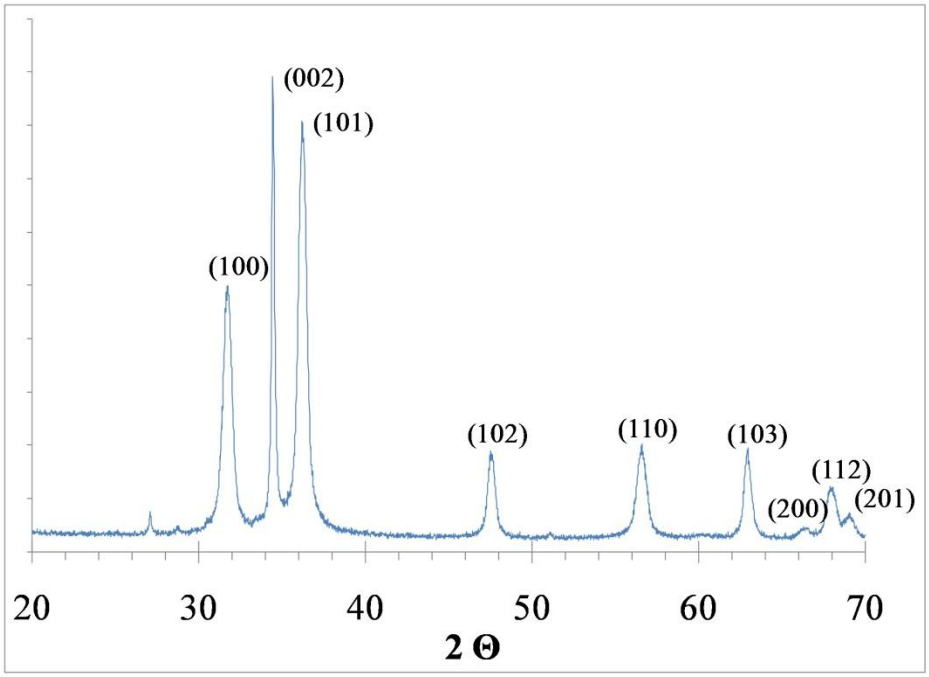

Figure 3.6 An X-Ray diffractogram obtained for ZnO nanopods. Variation in peak widths corresponding to (100), (101) & (002) planes indicate an anisotropy in crystal size.

A key feature of note in the XRD pattern is the variation in full-width at half maximum (FWHM) between various peaks, especially at 31.7, 34.5 and 36.25 2Θ angles. The peak at 34.5 2Θ, corresponding to the (002) plane of the wurzite crystal, is noticeably sharper than the peaks at 31.7 and 36.25 2Θ, which correspond to the (100) and (101) planes, respectively. Peak broadening in powder XRD is typically observed for monocrystalline materials without defects in cases when crystallite size is below 100 nm.[81] In such cases a Rietveld analysis performed on the diffractogram, after deconvolution of the instrument response, can give a quantitative measure of crystallite

size. Rietveld analysis employs a fundamental parameter approach to fit a theoretical peak profile to a measured peak profile given a known crystal structure. For a known crystal structure and its corresponding powder XRD pattern typically reported by the Joint Committee on Powder Diffraction Standards (JCPDS), variation in peak widths of individual crystal planes measured for a given sample can be co-related to crystallite size in the corresponding direction.

Crystal plane	2Θ	Crystal Size (nm)
(100)	31.7	11.81 ± 0.08
(002)	34.5	40.19 ± 0.3
(101)	36.25	12.68 ± 0.05
(102)	47.56	15.62 ± 0.34
(110)	55.56	11.65 ± 0.48
(103)	62.92	18.93 ± 0.52
(200)	66.35	12.2 ± 0.06
(112)	67.93	12.65 ± 0.25
(201)	69.07	7.96 ± 0.31

Table 3.1 Crystal size estimations obtained via Rietveld analysis of X-Ray diffractogram for different crystal planes of ZnO nanopods.

A Rietveld Analysis of the XRD pattern obtained for ZnO nanopods, observed in Figure 3.6, was performed on TOPAS software (v4) using a fundamental parameter approach. Crystal size values were measured from peak widths estimated using integral breadth measurements. Fitting individual peaks in the XRD pattern with the fundamental

parameter approach showed that crystallite sizes along the (100) and (101) planes, 31.7° and 36.25° 2Θ respectively, were ~11-12 nm (Table 3.1). These values match closely with individual leg diameters of the ZnO nanopods, as would be expected for a monocrystalline wurzite ZnO crystal.

A sharp peak at 34.5° 2Θ which corresponds to the (002) plane for wurzite ZnO has an estimated crystallite size of ~40 nm. (Table 3.1) Crystallite sizes ZnO is known to have three types of fast growth directions including the ±[001] direction.[82] A sharper (002) peak in the XRD pattern of the ZnO nanopods, indicating a larger crystal size along the [002] direction, thus corresponds to growth along the length of the individual legs of each nanopod structure. This is confirmed by HR-TEM images of individual nanopod legs shown in Figure 3.7. Interplanar spacing along the length of individual legs of ZnO nanopods corresponds to the (002) d-spacing for wurzite ZnO (0.52 nm). It is important to note that the crystal size perpendicular to the (002) plane, estimated from the XRD pattern, is smaller than the length of individual nanopod legs observed on TEM roughly by a factor of 5. Estimation of crystal sizes from XRD patterns can result in values smaller than the actual nanoparticle sizes, as measured by TEM, due to presence of crystal defects such as line dislocations and grain boundaries. As predicted by lower crystal size values, line defects are present in individual legs of ZnO nanopods along the [002] direction, as observed in HR-TEM images shown in Figure 3.8. Defects however do not exist in the [100] or [101] direction and give an accurate measure of nanoparticle size in those directions. An anisotropic peak broadening observed in the XRD pattern of

the ZnO nanopods is thus co-related to nanoparticle size and gives a quantitative measure of individual leg diameters in ZnO nanopods.

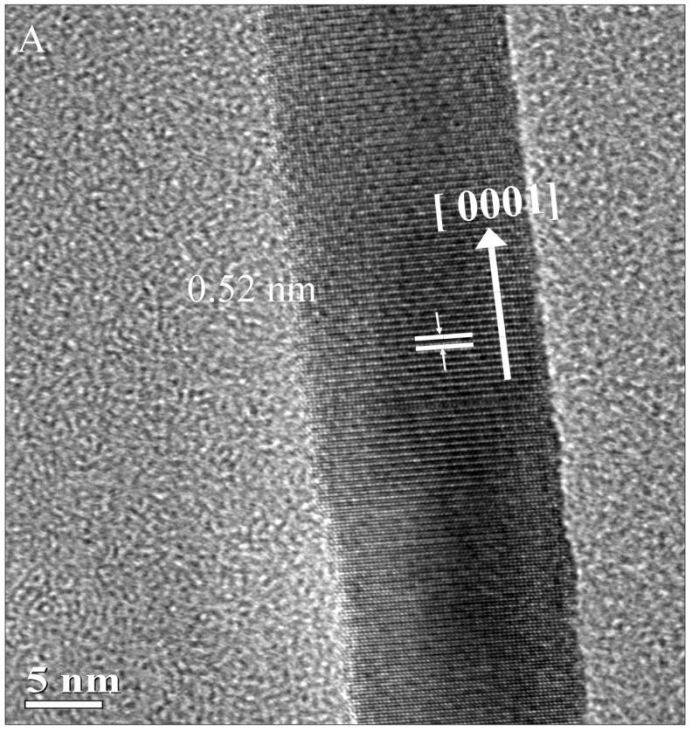

Figure 3.7 A HR-TEM image showing an individual leg of a ZnO nanopod growing along the [0001] direction.

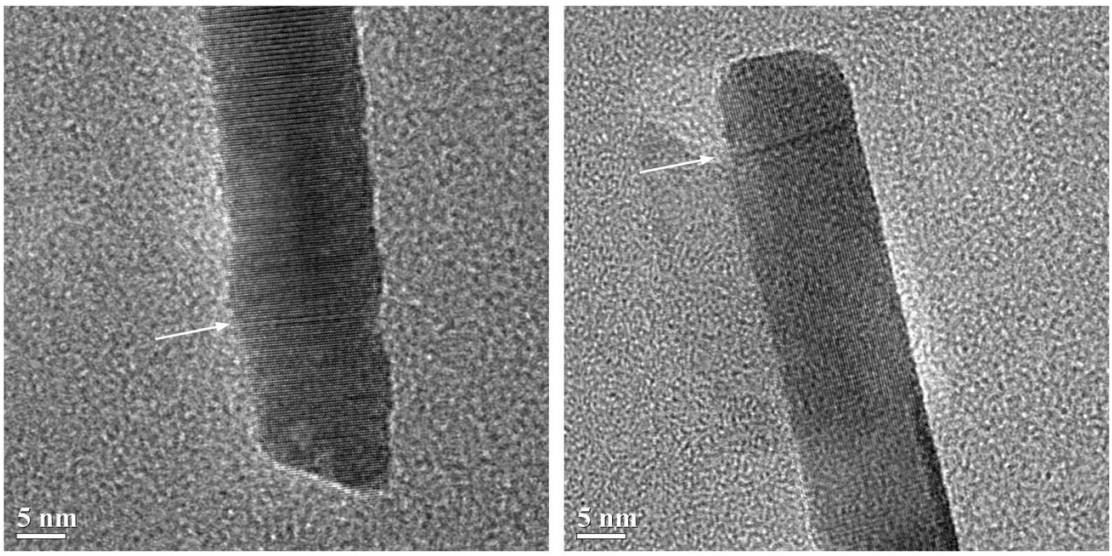

Figure 3.8 HR-TEM images of individual legs of ZnO nanopods show line defects in the [002] growth direction.

Additional characterization of the ZnO nanopods, as a whole, was performed using HR-TEM using a FEI Technai G20 operated at 200kV. ZnO nanopods generated after 20 minutes of reaction time were dropcast on 200 mesh Cu TEM grids pre-coated with a carbon film. (Electron Microscopy Sciences, Hartfield, PA) Figure 3.9A shows a low magnification TEM image of one nanopod consisting of three individual legs. The structure has a 'hole' between the individual legs indicating that individual legs were fused together. HR-TEM images of the nanopod, as shown in Figure 3.9B, reveal that while individual nanopod legs are monocrystalline growing along the [002] direction, the nanopod as a whole is a polycrystalline structure with visible grain boundaries between individual legs. Such observations, in conjunction with the fact that ZnO

nanopods possess a varying number of legs, as observed in numerous SEM images like in Figure 3.5, suggest that individual ZnO nanorods were fused together in a random orientation after they individually grew from the ZnO seeds to form nanopods. To further explore this hypothesis, ZnO nanostructures were synthesized at shorter reaction times of 2, 10 and 15 minutes and their morphological evolution was observed via TEM.

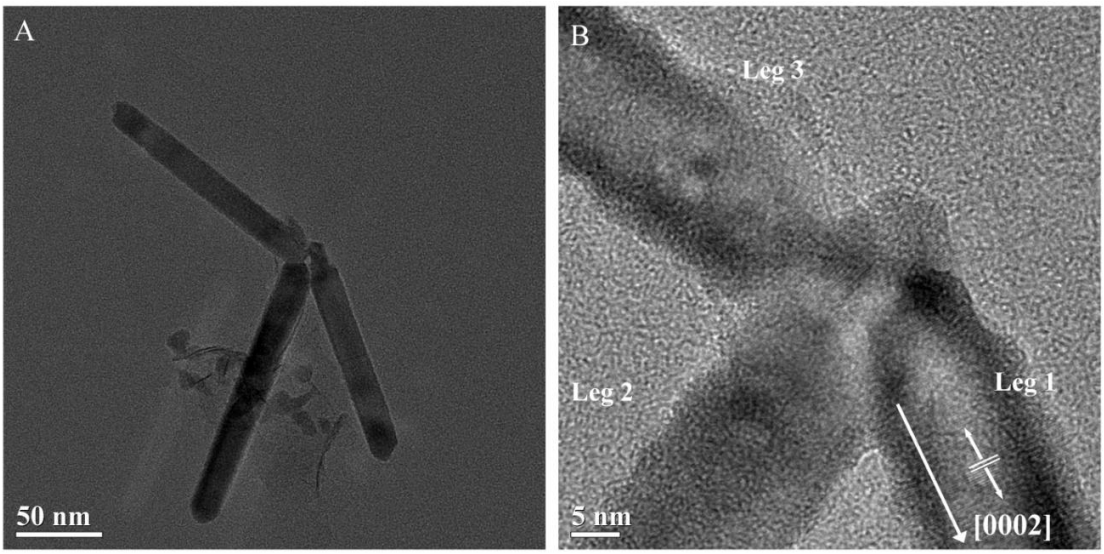

Figure 3.9 A low magnification TEM image of a single ZnO nanopod with 3 legs whith a 'hole' in the center. (A) All legs of the nanopod are joined with visble grain boundaries and each leg grows along the [002] direction. (B)

3.3.3 Mechanism of generation ZnO nanopods via heterogeneous nucleation

To understand the mechanism of generation of ZnO nanopods via heterogeneous nucleation, the temporal evolution in the morphology of ZnO nanopods was studied. For this, ZnO nanopods at various time points of 2, 10 and 15 minutes were generated and imaged via TEM. A bright field JEOL 1200 TEM, operated at 100 kV, was used for this

study. ZnO nanostructures generated at desired time points were dropcast on 400 mesh Cu grids, as before, and were imaged at numerous locations across multiple grids to get accurate size measurements. At least 25 measurements were taken for all sizes reported in this section.

At a reaction time of 2 minutes, ZnO nanorods with diameters of 36.7 ± 7.9 nm were observed alongside sub-5 nm ZnO seeds as shown in Figure 3.10A. TEM images suggest that nucleation from ZnO seeds and growth of ZnO nanopods is incomplete and ongoing at this stage in the reaction. Also, no multi-legged nanopods were observed. At a reaction time of 10 minutes, multi-legged nanopods, shown in Figure 3.10B, with individual leg diameters of 36.3 ± 20.9 nm were observed alongside nanorods, indicating an ongoing crystal growth phase. Appearance of multi-legged structures in TEM images at this stage of the reaction indicates initiation of an 'oriented crystal attachment' phase. Such oriented crystal attachment, in which crystal planes of individual single crystal nanorods fuse with each other to form polycrystalline nanopods, becomes dominant as nanopods with increasing number of individual legs are observed more frequently after 15 and 20 minutes into the reaction. An important feature to note is that after 15 minutes of reaction time, diameters of individual legs of the nanopods, seen in Figure 3.10C, are focused down to 12.4 ± 2.2 nm. A size focusing of leg diameters as reaction time proceeds, shown in Figure 3.10D, seems to occur concurrently with the oriented attachment phase and yields nanopods with leg diameters of ~15 nm after 20 minutes of reaction time.

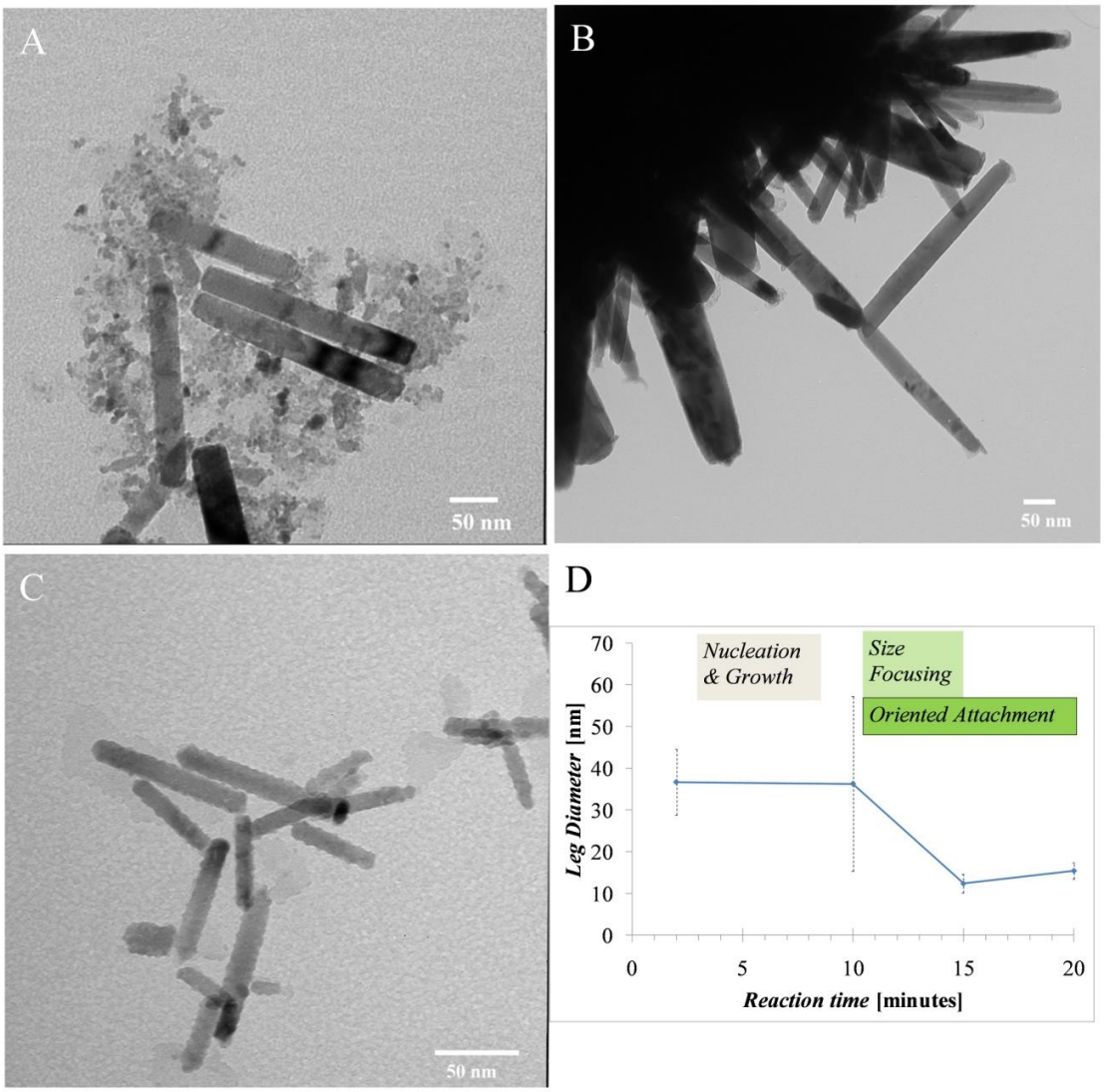

Figure 3.10 TEM images of ZnO nanostructures synthesized at (A) 2, (B) 10 and (C) 15 minutes of reaction time. A gradual temporal evolution from single nanorods (and unreacted seeds) to nanopods with small leg diameters is observed. The temporal evolution observed in individual leg diameters of ZnO nanopods (D) indicates that after an initial nucleation and growth phase to form nanorods, a concurrent size focusing and oriented attachment is observed leading to generation of multi-legged nanopods.

As discussed earlier in section 2.2, a key obstacle to the nucleation and growth of ZnO nanostructures via heterogeneous nucleation colloidally is the presence of an

alternate competing reaction pathway in the form of oriented attachment of 0-D ZnO seeds. Oriented attachment of ZnO seeds leading to formation of large aggregates would be prohibitive for heterogeneous nucleation and formation of 1-D nanostructures. However, such attachment is usually a very slow process, typically taking several hours.[53] In this work, the temporal evolution observed during the course of the reaction for generation of nanopods suggests that 1-D ZnO nanorods nucleate and grow from 0-D ZnO seeds initially and then subsequently undergo 'oriented attachment' as has been previously observed for sub-5 nm nanoparticles by Pacholski *et al*.[53]

The microwave-assisted hydrothermal approach, used for generation of the nanopods, has been shown to accelerate the rate of reaction and shorten time required for generation of ZnO crystals in Chapter 2. The accelerated rate of reaction for nucleation and growth of ZnO nanostructures, obtained via heterogeneous nucleation, presumably changes the dynamics between the two competing mechanisms of 1-D nucleation and growth versus oriented attachment of nanostructures. Heterogeneous nucleation and growth of 1-D ZnO nanorods is seemingly promoted over oriented attachment which eventually takes place leading to fusion of nanorods and generation of multi-legged nanopods.

3.4 Optical properties of ZnO nanopods

The ultra-small dimensions of the ZnO nanopods generated in this work lends to potentially interesting PL properties for reasons previously discussed in section 3.1.1. Such PL properties could also provide an ideal platform for design of optical gas sensors, an area which has not been studied in the literature. In this section PL properties

of ZnO nanopods, generated after 20 minutes of reaction time using the microwave-assisted approach discussed above, have been studied.

ZnO nanopods having smallest dimensions of ~15 nm are not expected to have quantum confinement effects. In order to confirm this, UV-visible absorption measurements were performed on the ZnO nanopods and ZnO microrods (generated via homogeneous synthesis in Chapter 2). UV-visible measurements were carried out in a Hitachi U-4100 UV-Vis-NIR spectrophotometer using an integrating sphere. Indeed, the absorption spectrum of ZnO nanopods, as observed in Figure 3.11, is similar to that of 250 nm ZnO microrods and consistent with bulk ZnO.

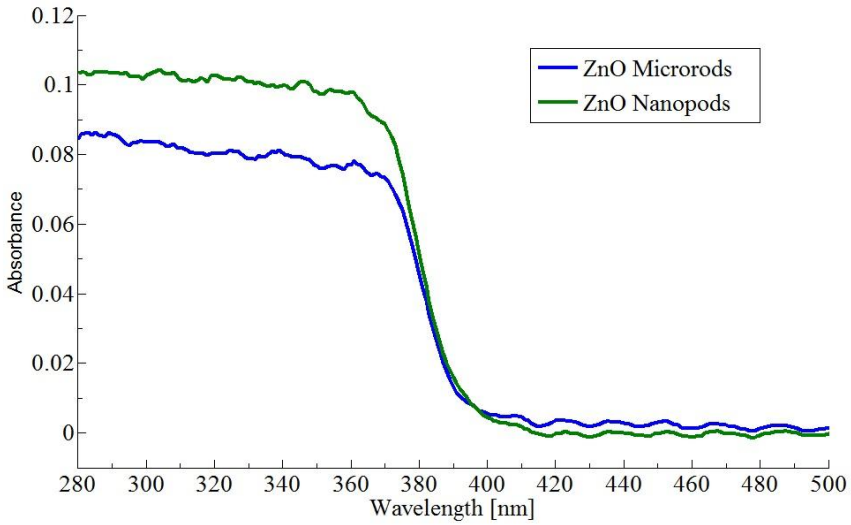

Figure 3.11 A plot showing UV-visible absorption spectra for ZnO nanopods and microrods.

As observed in the absorption curves in Figure 3.11, UV excitation above the bulk band-gap, 3.37 eV or 368 nm, would be well suited for excitation for a PL study of

the nanopods. However, ZnO nanopod samples are highly scattering even at excitation wavelengths of 350 nm. Sample scatter can be attributed to a large leg span of individual nanopods, measured from individual leg tips, which can exceed over 1 μm. Sample scatter impedes the study of PL properties of ZnO by contributing to a large background. This issue can be circumvented in two different ways:

1. Use of a high fluence excitation source, such as a UV laser or
2. Study of PL properties at low temperatures, liquid N_2 temperatures or lower.

Each of the above approach was used in the study of PL properties of ZnO nanopods generated in this work. PL measurements were carried out on a PTI QuantaMaster™ with a Xe arc lamp excitation source at liquid nitrogen temperatures and a customized optical system designed around a tunable doubled Ti:Sapphire femtosecond-pulsed laser (Coherent Mira 900, 140 fs pulse width, 78 MHz repetition rate, tunable range 700-900 nm). While the use of a high fluence Ti:Sapphire laser, at 350 nm excitation, for PL study at room temperature (RT) is preferred for optical gas sensing applications, enhanced PL that would be obtained during low temperature studies with the Xe arc lamp excitation offers the possibility to study the NBE PL of the ZnO nanopods. A detailed discussion of PL properties of the ZnO nanopods with both optical systems is included in subsequent sections.

3.4.1 Low temperature PL studies on ZnO nanopods

Low temperature PL measurements were performed on a PTI QuantaMaster™, which was equipped with a liquid nitrogen dewar. The dewar, designed to fit in a standard cuvette holder, has quartz windows for excitation and PL detection. For PL

studies at 77 K, a solid or liquid sample can be placed inside a NMR tube which fits into the dewar filled with liquid N_2. For this study, a quartz NMR tube with ZnO nanopod samples dried inside was placed in the dewar and excited at 350 nm (slit width 5 nm) with a Xenon arc lamp. An appropriate long-pass filter was used on the detector side (Hamamatsu R928 PMT) to reduce the amount of scatter in the system.

Upon excitation, the PL spectra of ZnO nanopods show a large defect-related DL emission in the orange-red region of the visible spectrum, as can be observed in Figure 3.12. The defect-level band for the ZnO nanopods is very broad with a peak at ~615 nm and FWHM greater than 140 nm. Similar orange-red DL emission has previously been observed for nanosized ZnO needle-like structures generated via vapor-phase processes.[33,83] Physically, such orange-red emission can be attributed to donor-acceptor transitions involving Zn vacancy complexes.[84]

An enhanced PL in the ZnO nanopods at liquid N_2 temperatures allows the study of NBE PL of the ZnO nanopods. The NBE PL of the nanopods is weak with peak intensity, at 374 nm, only ~12% the intensity of the DL peak at 615 nm. A low NBE PL is to be expected from nanopods owing to a very high surface area. A large surface area, consequently leading to a large number of surface states, quenches the NBE PL in favor of low energy visible DL emission.

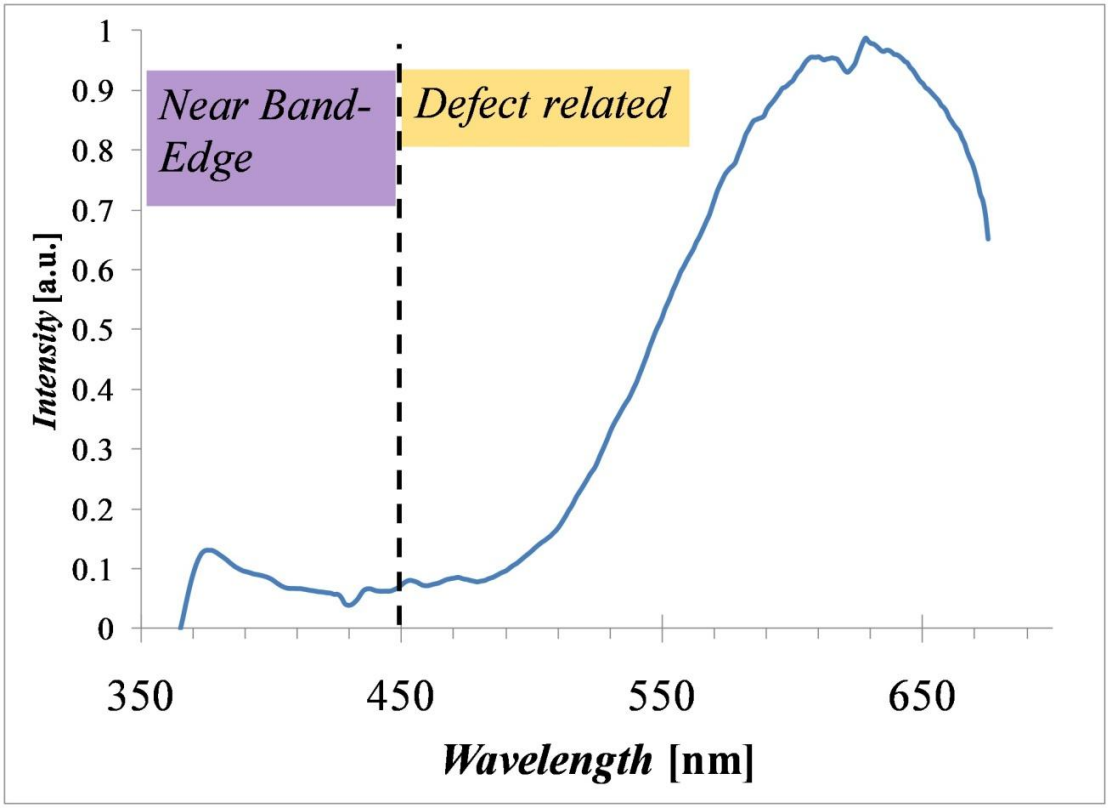

Figure 3.12 PL spectrum of ZnO nanopods used in this work obtained at 77 K. ZnO nanopods exhibit broad orange-red defect-related PL in addition to a NBE PL at 373 nm when excited above band-gap energies at 350 nm.

3.4.2 Room temperature PL studies with Ti:sapphire laser excitation

A customized optical system, shown in Figure 3.13, was designed for study of room temperature PL of the nanopods. The room temperature PL study here enables the application of ZnO nanopods for chemical gas sensing studied in subsequent sections. The optical system for room temperature PL study is designed around a Ti:Sapphire femtosecond-pulsed laser excitation source (Coherent Mira 900, 140 fs pulse width, 78 MHz repetition rate) tuned to 700 nm. The fundamental laser light was frequency doubled via a Type I BBO crystal to excite the sample at 350 nm. An Acton 2300i

Spectrometer fitted with a Pixis 100 CCD camera was used as the detector and placed at a 90° angle to the excitation light. The sample chamber consisted of a 10 mm path length cuvette holder An appropriate short pass filter on the excitation side and a long pass filter on the detector side were used to reduce the amount of scatter. To further help alleviate light scatter, the excitation beam was focused using a 75 mm plano-convex lens to a ~2 mm spot at the sample, which was dried inside a quartz cuvette. Details about additional functionalities such as a tunable humidifier, which were introduced in the system for gas sensing studies, will be discussed in subsequent sections.

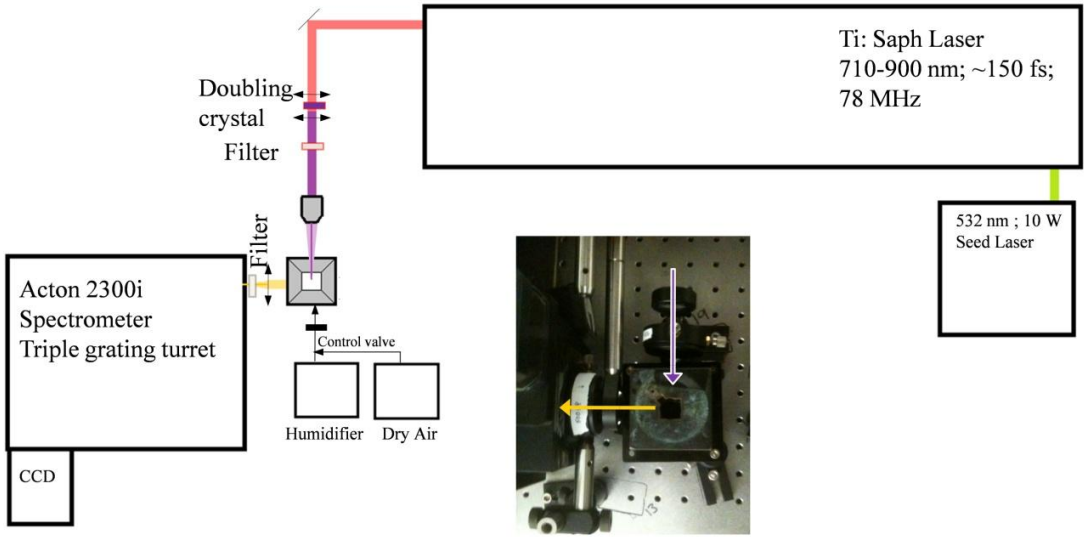

Figure 3.13 A schematic of the optical system designed around a Ti:Sapphire laser for PL and humidity studies on ZnO nanopods used in this work.

Figure 3.14 shows the DL emission of the ZnO nanopods collected at room temperature in the system designed as above. A small red shift of ~15 nm, less than 10% of the FWHM, was observed in the center wavelength of the defect band collected at

room temperature when compared to spectra obtained at liquid nitrogen temperatures. Also, no detectable NBE PL, above the background scatter, was observed at room temperatures.

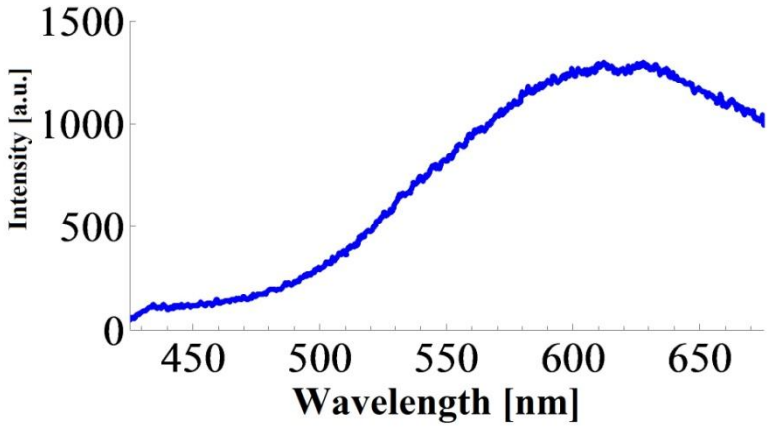

Figure 3.14 DL emission of ZnO nanopods obtained at room temperature with a Ti:Sapphire excitation at 350 nm.

3.5 Optical gas sensing with ZnO nanopods

3.5.1 Background

Chemical gas sensing is an important area of application for ZnO nanostructures. Typically, gas sensors using 1-D ZnO nanostructures are configured as resistors whose conductance is altered by charge-transfer processes occurring at and near their surfaces in response to changes of the local environment. [18,85-87] It is well known that molecular oxygen adsorbed onto the surface of ZnO forms active surface complexes that act as electron acceptors leading to generation of an electron depletion region.[87,88] The width of such a depletion region in ZnO nanostructures is sensitive to ambient gases and can

cause changes in conductance of the nanostructures.[18,89] Proportionally, changes in electrical conductance are larger for ultra-small ZnO nanostructures where the width of the depletion region is comparable to the dimensions of the nanostructures, thus imparting higher sensitivity in response to ambient gases.[89,90]

One of the biggest challenges with electrical gas sensors is the integration of the nanostructured sensor element into device design. Inconsistencies during device fabrication while making electrical contacts with the sensor element can lead to variations in device performance. Monitoring the PL response instead of electrical conductance provides an alternative motif for chemical gas sensing with ZnO nanostructures. Optical motifs for gas sensing with ZnO nanostructures offer a distinct advantage over electrical readouts; optical sensing can be done remotely without the need for tethering or tedious device fabrication. PL intensity of ZnO nanostructures, especially the DL emission band in the visible range of the electromagnetic spectrum, caused by deep-level donor-acceptor transitions that occur due to defect-related surface states,[33]can be used for gas sensing. Similar to electrical conductance, donor-acceptor transitions at and near the surface of ZnO nanostructures are affected by changes in the width of the electron depletion region caused in response to changes in the ambient environment of the ZnO nanostructures. Consequently, this alters the PL of ZnO nanostructures providing an optical signal for chemical gas sensing.

Optical gas sensing with ZnO nanostructures has not been studied in any amount of detail in the literature. A few recent reports have explored the nature of the PL response from larger 1-D ZnO nanostructures, with smallest dimensions exceeding 50

nm, to gases like NO_2, ethanol and humidity.[91-94] These studies, however, employed ZnO nanostructures grown on substrates. As aforementioned in section 2.2, nanostructures for optical sensing should ideally be synthesized colloidally as structures grown on substrates can provide non-radiative pathways for carrier recombination which is detrimental to their sensitivity.

ZnO nanopods, with ultra-small sub-20 nm dimensions, generated in this work colloidally possess a higher ratio of surface states as compared to larger nanostructures, thereby providing a platform for design of such optical gas sensors with potentially increased sensitivity. The strong defect-level PL observed in the colloidally synthesized ZnO nanopods makes them ideal candidates as optical chemical gas sensors. As a proof of concept, application of colloidally grown ultra-small ZnO nanopods to optical humidity sensing has been explored in this work. Humidity, while itself not environmentally relevant, would produce a response similar to reducing gases like CO and CO_2 and would serve to determine the applicability of ZnO nanopods as optical gas sensors.

3.5.2 Experimental details for optical gas sensing with ZnO nanopods

The optical system described in Figure 3.13 was used for humidity sensing experiments described in this section. ZnO nanopods, dried inside a quartz cuvette, were exposed to varying levels of humidity using an in-house designed tunable humidifier. The humidifier design consisted of mixing 100% humid air, generated by a wet-air column, with 0% humidity dry air. The humidity, after mixing, could be monitired and tuned from 20 – 90% relative humidity (RH) by varying the flow rates of 0% and 100%

lines. Flow rates were controlled by rotameters, Omega FL 4213-V and FL 4214-V for dry air and 100% RH humid air, respectively. Total air flow inside the sample chamber was maintained at ~7 liters per minute (LPM).

For humidity sensing, PL of the ZnO nanopods collected at room temperature was integrated across the entire defect band, 450-690 nm, and monitored in response to changes in humidity. ZnO nanopods were found to undergo quasi-reversible photobleaching when excited at 350 nm. The integrated PL intensity of the defect band of ZnO nanopods decreased by ~36% of its original value upon continuous excitation for a period of 5 minutes with 350 nm light at a fluence of ~475 mW/cm^2, as observed in Figure 3.15. Reports of similar photobleaching effects have been previously observed with ZnO nanoparticles and can be attributed to reversible charging of ZnO during photoexcitation.[95] While the decay in the PL intensity seemingly stabilizes after ~4 minutes of continuous excitation, a loss in PL signal is not ideal for gas sensing studies.

In order to circumvent this problem, the use of a periodic excitation scheme was explored for sensing studies. Periodic excitation involved illumination of the sample for an 'on' time of 1 second followed by a recovery 'off' time of 20 seconds. Upon periodic photoexcitation of the ZnO nanopod sample, the decay in PL intensity was found to reduce dramatically, resulting in a loss of only ~15% after 5 minutes, as shown in Figure 3.15. The laser light fluence used during the 'on' time was ~475 mW/cm^2. It should be noted that a majority of the decay of the PL signal during periodic photoexcitation occurs over the first two minutes of excitation (13% decay) with subsequent stabilization in signal intensity.

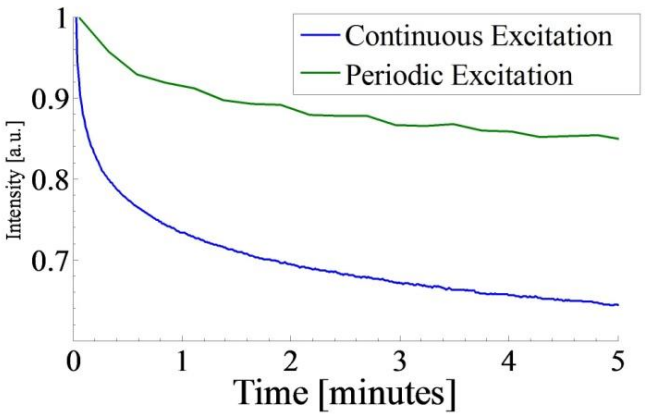

Figure 3.15 Decay of of PL signal in ZnO nanopods with continuous and periodic excitation at excitation fluence of 475 mW/cm^2.

Additionally, it was found that the fluence of the excitation laser light has a significant impact on signal decay. Upon reducing the laser fluence from ~475 mW/cm^2 to ~160 mW/cm^2, the total loss in PL signal intensity reduced ~2 fold after 5 minutes of continuous excitation, as shown in Figure 3.16. For periodic excitation at a lower excitation fluence of ~160 mW/cm^2, the signal decay averaged ~0.375% per minute indicating stable PL for lower excitation fluence. To reduce artifacts in measurement of changes in optical signal due to such quasi-reversible photobleaching effects, a periodic excitation scheme with 1 second exposure every 20 seconds at a laser light fluence of ~160 mW/cm^2 was used for humidity sensing experiments.

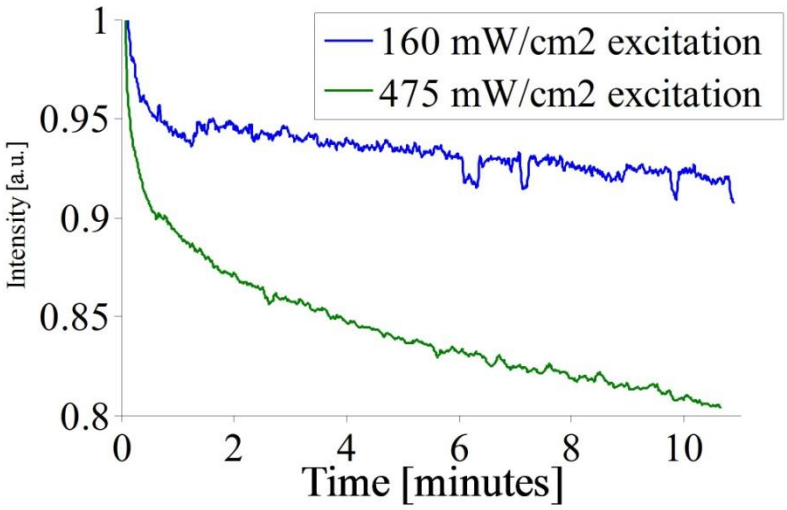

Figure 3.16 Decay of PL signal in ZnO nanopods with continuous excitation at an excitation fluence of 475 and 160 mW/cm^2.

3.5.3 Optical humidity sensing with ZnO nanopods : results

Prior to each experiment, ZnO nanopods dried inside a quartz cuvette were stabilized under dry air (flow rate ~1.5 LPM) for a period of 30 minutes. For each experiment, the stability of the PL signal, using a periodic excitation scheme as described above, was confirmed for an initial period of 5 minutes. The sample was subsequently exposed to varying degrees of humidity, in a random fashion, for a period of 25 minutes per humidity level. The flow rate during this time period was kept constant at ~7 LPM. Each humidity level was followed by exposure to dry air at ~1.5 LPM for 25 minutes to allow for stabilization of the local sample environment for subsequent experiments.

The defect-level PL intensity of the ZnO nanopods was found to increase upon exposure to humid air. The maximum change in integrated PL intensity, observed after a 25 minute exposure to humid air, varied from a 30% increase for 85% RH to 8% increase for 22% RH, as shown in Figure 3.17. It is important to note that the humidity response dynamics of the ZnO nanopod sensor showed two distinct phases. An initial rapid increase in total signal intensity upon exposure to humidity lasted for ~2 minutes and accounted for ~60% of the total response observed at the end of 30 minutes. This was followed by a phase exhibiting a slower increase in PL signal. Results also indicated the increase in the PL intensity was completely reversible upon exposure to dry air.

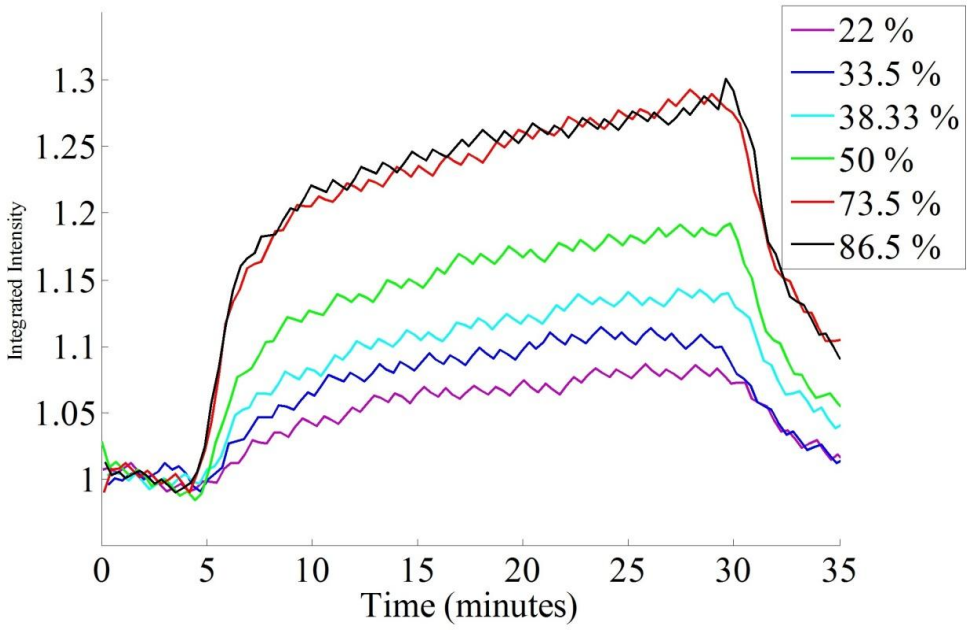

Figure 3.17 Response of defect-related PL intensity integrated from 450- 690 nm of the PL spectra of ZnO nanopods to variations in ambient levels of humidity.

It is noteworthy that sensor dynamics observed for changes in PL signal are similar to the dynamics observed in ZnO nanostructure gas sensors interrogated via changes to electrical conductance in response to reductive gases such as ethanol vapor.[18] Given the ultra-small dimensions of the ZnO nanopods, the electron depletion layer caused by adsorption of ambient oxygen, ionized as O^- or O^{2-}, on the surface is comparable to the diameters of the nanopods. The depletion layer model postulated for ZnO nanostructures with such ultra-small diameters predicts the electrical sensitivity, as measured by percent change in electrical conductance, in response to changes in the ambient chemical environment to be higher than that for structures with larger (>50 nm) diameters.[89] In analogy to higher electrical sensitivity stemming from the increased ratio of surface states to total available states in these types of nanostructures, the PL of the nanostructures will also be impacted by this phenomenon and produce highly sensitive optical gas sensors. Indeed this is observed in the calibration curve for observed optical responses, a plot of maximum observed response in PL intensity versus % RH. The calibration curve follows a sigmoid curve with the sensor saturating at >75% RH, as seen in Figure 3.18. Sensitivity of the ZnO nanopods sensor defined as Δ(maximum response in PL intensity)/Δ(RH) shows a linear behavior in the range of 22 – 70% RH with a 0.4% increase in optical intensity per % change in RH. ZnO nanopods synthesized in this work show a larger dynamic range and enhanced optical sensitivity (by a factor of ~5) in response to ambient humidity changes as compared to similar studies on larger nanostructures.[93] Such enhanced sensitivity most likely arises due to a

large ratio of active surface states contributing to DL emission in the ZnO nanopods with ultra-small diameters.

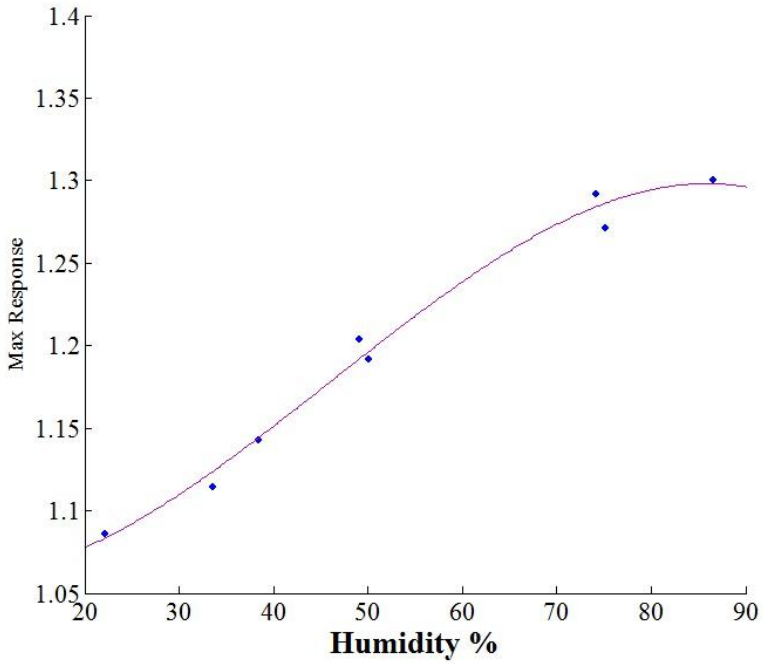

Figure 3.18 A calibration curve for maximum response at various levels of humidity for optical humidity sensing with ZnO nanopods.

3.6 Summary and conclusions

In this work a novel method for colloidal synthesis of ZnO nanopods with ultra-small dimensions via microwave-assisted heterogeneous nucleation under hydrothermal conditions was demonstrated. ZnO nanopods with ~15 nm individual leg diameters were synthesized using ~4 nm ZnO nanoparticle seeds in as little as 20 minutes of reaction time. Individual legs of each ZnO nanopod were shown to be single crystals with growth taking place along the c-axis or [0001] direction.

The applicability of microwave-assisted synthesis for generation nanostructures, as demonstrated in this work, is a direct consequence of localized molecular heating in a microwave-assisted reaction. A microwave-based heating methodology favors nanostructure growth over undesirable reaction pathways, such as oriented nanoparticle attachment, and consequently allows the use of 0-D nanoparticles as 'seeds' for colloidal heterogeneous nucleation for generation of nanostructures. Additionally, a shortened reaction time and high degree of control over critical nanoparticle dimensions lends commercial viability to the use of microwaves for nanoparticle generation. The design motifs presented in this work, for generation of ultra-small ZnO nanostructures, can be extrapolated and utilized for synthesis of similar metal-oxide nanomaterials such as iron oxide or titanium dioxide. Microwave-assisted methods thus provide a viable alternative to convectional-based heating methods for generation of metal oxide nanoparticles.

ZnO nanopods exhibit broad orange-red defect-related PL in addition to a NBE emission at 373 nm when excited above band-gap energies. ZnO nanopods generated in this work can be used as optical humidity sensors by monitoring changes in intensity of the defect-related PL in response to variations in ambient humidity levels. As optical humidity sensors, ZnO nanopods with ultra-small dimensions exhibit a large dynamic range and high sensitivity to changes in ambient humidity levels. The sensitivity of the optical sensors to humidity was approximately 5x greater than previous reports using larger nanostructures.

Results shown in this work indicate that ZnO nanostructures with ultra-small dimensions have potential to serve as sensitive room temperature optical sensors for

environmentally-relevant chemical gases like NO_2 and CO. Further studies exploring sensor dynamics, specifically response times, calibrations and sensor device design, remain to be done.

4 MICROWAVE-ASSISTED SYNTHESIS OF CADMIUM-BASED QUANTUM DOTS

In the previous chapters, the applicability of microwave-assisted synthesis for generation of ZnO nanostructures, a II-VI semiconductor, was demonstrated. The use of a microwave-assisted approach is unique because of its ability to heat reaction mixtures at a molecular-level. This consequently offers a high degree of control over synthesis, in terms of nanostructure size, and can lead to alternate reaction mechanisms unavailable by convectional heating as was demonstrated in the generation of 0-D and 1-D ZnO nanostructures. In this chapter, a microwave-assisted approach has been applied for the generation of another II-VI semiconductor nanocrystal - cadmium-based quantum dots (QDs). The generation of QDs is a first step for the generation of a protein·QD nanocomposite, which is studied in Chapter 6.

4.1 Background

Zero-dimensional quantum confined cadmium chalcogenide semiconductor nanocrystals, a.k.a. QDs, have recently generated considerable interest as photoluminescent entities that can span the visible-near IR range. They possess many useful optical properties including size-tunable and high quantum yield PL, high resistance to photobleaching, long-term photostability, high UV absorption, narrow emission, and a large effective Stokes shift which make them appealing for use in areas of biomedical research. Such optical properties of QDs have led to notable applications in chemical and biological sensing,[22-24] optical multiplexing device design,[25] and as non-radiative probes for labeling and imaging.[26,27]

Much of the interest in applications with QDs has evolved because of the rapid development in benchtop synthesis of highly monodisperse nanocrystals of cadmium chalcogenides. Colloidal synthesis of Cd-based QDs, CdX (X = S, Se and Te), has been exhaustively studied and can be currently found in the literature.[9-11,96-106] Most methods for synthesis of QDs involve an organometallic reaction in a heating bath consisting of an instant nucleation phase, a high temperature reaction between a Cd^{2+} and Se^{2-} or Te^{2-} precursor, and a growth phase which is primarily controlled by reaction temperature and time.[10,96,98,104,107] The synthesis reaction involves the use of additive ligands like phosphonic acids (most commonly tetradecylphosphonic acid) or amines (most commonly hexadecylamine) and phosphines (most commonly trioctylphosphine) which assist in solubility of the Cd^{2+} and Se^{2-} or Te^{2-} precursors, respectively. Broadly, two categories of solvents are typically used for organometallic synthesis. These include (a) coordinating solvents like trioctylphosphine oxide(TOPO)[9-11,99,100] or fatty acids like stearic acid (SA)[101,102] and (b) non-coordinating solvents like 1-octadecene (ODE).[103,104]These methods produce monodisperse QDs with a high degree of control over sizes, between diameters of 20-100 Å, which consequently determines their band structure and optical properties. Size control during synthesis of QDs can be achieved by individual or a combinatorial variation of reaction parameters like time, temperature, and precursor or ligand concentration.[106,108] Further, passivation of the CdSe or CdTe cores with a wider bandgap inorganic semiconductor shell, like ZnS,[99,100,109,110] has been shown to produce QDs exhibiting a high quantum yield (~50%).

4.2 Microwave-assisted synthesis of QDs

The use of microwave irradiation, as opposed to convectional heating, for generation of QDs using organometallic chemistries, similar to the ones described above, has been previously studied by Ziegler *et al.*[111] and Washington *et al.*[112] Microwave-assisted synthesis of QDs is cleaner than the use of heating baths with less unreacted reactants in the final product, eliminating the need for significant post-processing steps.[113] Reaction with the use of microwaves is faster than convectional-heating methods, as would be expected, and produces monodisperse QDs with high quantum yields. In this work a single-pot microwave-assisted approach has been employed for the synthesis of CdSe, CdTe and CdSe(ZnS) core(shell) QDs, whose PL collectively spans the visible and NIR range of the electromagnetic spectrum. QDs generated as part of this work have been used for nanotoxicology studies[114] and studies related to generation of a protein·QD nanocomposite[115] (as discussed in Chapter 6).

4.2.1 Synthesis of CdSe and CdSe(ZnS) QDs by a microwave-assisted approach

CdSe QDs were synthesized in this work using previously reported organometallic chemistries adapted for microwave-assisted use. For synthesis, 51.4 mg of cadmium oxide (CdO, 99.99%, Alfa Aesar) was dissolved in a mixture of 223.3 mg tetradecylphosphonic acid (TDPA, 98%, Alfa Aesar) and 3.77 g of tri-*n*-octylphosphine oxide (TOPO, 99%, Aldrich). The mixture, a solid (powder) phase at room temperature, melts when heated above 170 °C. To dissolve the cadmium oxide and generate Cd^{2+} ions, the precursor mixture was heated, in a single-mode microwave cavity of the CEM Discover® microwave reactor, to a temperature of 300 °C under an inert argon

atmosphere for a period of 30 minutes. A selenium stock solution was prepared separately by dissolving 41.1 mg of Se powder (99 %,Aldrich) in 2.4 ml of tri-n-octylphosphine (TOP, 99%, Aldrich) by vigorous stirring. The Se stock was injected into the prepared Cd precursor, maintained at 300 °C, resulting in instant nucleation of CdSe nanocrystals. Subsequent growth of CdSe crystals to a desired size, and consequently PL wavelength, was achieved by a combination of hold temperatures and times.

A

B

Temperature (^{0}C)	Heating time (in minutes)	Emission wavelength (in nm)
210	1	475
250	1	535
270	2	550
270	4	620

C

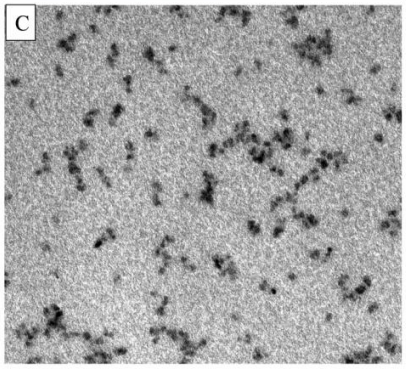

D

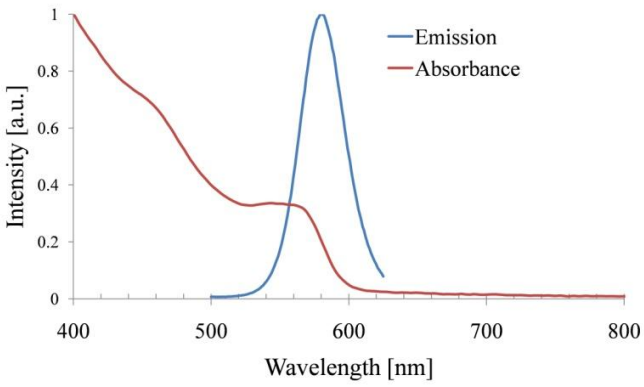

Figure 4.1 CdSe QDs produced by microwave-assisted methods used in this work with PL spanning the entire visible range (A). Critical reaction parameters used during the synthesis of QDs (B). TEM images of the QDs (C) and absorption and PL spectrum of a typical QD sample (D).

Figure 4.1A shows the range of CdSe QDs generated in this work. QDs with an emission maximum from 475 nm to 620 nm, spanning almost the entire visible range of

the electromagnetic spectrum, can be generated by varying the hold times and temperatures as shown in Figure 4.1B. Smaller QDs, ~2 nm in diameter, which emit in the blue range of the visible spectrum can be generated by using lower hold temperatures of ~210 °C and shorter hold times.‡ On the other hand, larger CdSe QDs, with ~620 nm emission maximum, can be generated at higher temperatures of ~270 °C and longer hold times. Figure 4.1C shows a representative TEM image of CdSe QDs produced by microwave heating.

A microwave-assisted approach for QD generation was found to result in high sample quality in terms of size polydispersity. The as-produced QD samples have a very narrow emission FWHM of ~30-35 nm, as shown in the emission spectrum in Figure 4.1D, without employing any tedious size selective precipitation techniques. Such accurate size-focusing can be attributed to uniform heating within the single-mode microwave cavity and short heating times required for the growth of the CdSe crystal. Indeed, the use of longer heating times, in an attempt to generate larger CdSe nanocrystals, resulted in 'defocusing' of the sample increasing polydispersity and consequently the PL FWHM. The heating times and temperatures for CdSe nucleation and crystal growth, as shown in Figure 4.1B, have been optimized for generation of CdSe QDs in a microwave-assisted reaction.

Passivation of the CdSe or CdTe cores with growth of a wider bandgap inorganic semiconductor shell, like ZnS,[99,100,109,110] is a typical practice which has been shown to increase PL quantum yield and prolong nanoparticle stability. In the

‡ For generation of 475 nm emitting QDs, 3.77 g of hexadecylamine was used as the solvent instead of TOPO

microwave-assisted approach used in this work, a ZnS shell can be grown on the CdSe cores using a single-pot approach. For this, a mixture of Zn and S precursors, 1.6 ml of dimethylzinc (DMZ, 1M in heptane) and 0.42 ml of hexamethyldisilathiane (HMDS, Aldrich), dissolved in 6.3 ml of TOP was injected rapidly into the reaction mixture right after growth of CdSe cores. The growth of the ZnS shell was allowed to carry on for a period of ~30 minutes at a temperature of 200 °C. The process of ZnO shell growth is confirmed by an increased quantum yield, discussed in following paragraphs, and also resulted in a slight increase in CdSe core diameters as was evidenced by ~20 nm red-shift in PL wavelengths of CdSe(ZnS) core-shell QDs.

Perhaps the most important measure of QD nanocrystal quality, generated from any synthesis process, is the fluorescence quantum yield as defined as the ratio of the number of photons emitted to the number of photons absorbed. The quantum yield of QDs, Φ_{QD}, generated in this work was measured relative to the quantum yield of Rhodamine 6G (R6G) standard dye, $\Phi_s = 0.95$, having an emission maximum at 540 nm using a procedure developed by Tønnesen *et al*. [116] In this Φ_{QD} is measured using the absorbance and PL (emission) values for both the QDs and the standard R6G dye as follows:

$$\frac{\Phi_{QD}}{\Phi_s} = \frac{\left(\frac{I_{QD}}{A_{QD}}\right)\eta_{QD}^2}{\left(\frac{I_s}{A_s}\right)\eta_s^2} \qquad \text{Equation 4.1}$$

Where, I_{QD} and I_s are the PL intensities of the QD and the standard respectively; A_{QD} and A_s are measured absorbance values of the QD and the standard, respectively; and η_{QD} and η_s are refractive indices of the solvent containing QD and the standard. For

accurate quantum yield measurements the following specific considerations should be made:

- Absorbance at excitation wavelength, for both the QDs and R6G standard should be in the region of 0.02 – 0.07 (and certainly less than 0.1). Also, absorbance at the excitation wavelength for the standard dye and QDs should be matched as much as possible. While Equation 4.1 accounts for changes in absorbance, a matched absorbance yields more accurate values.
- The slit width (bandpass) of the excitation monochromator and absorbance should be the same. (if possible)
- The excitation wavelengths for both the standard dye and QDs should be identical, if possible. If different excitation wavelengths are used, the emission units should be converted to energy units by multiplication with wavelength.
- QDs and the standard R6G dye should be suspended in the same solvents, if possible. If different solvents are used, accurate values of the refractive indices of the solvent, at excitation wavelengths used, should be known.

CdSe(ZnS) QDs produced by microwave-assisted heating exhibit high quantum yields of ~58% as measured against R6G, as discussed above. This is a marked increase from CdSe QDs (cores only) which exhibit quantum yields of ~30%. Quantum yields of CdSe(ZnS) core-shell QDs can be further increased by annealing of the ZnS shell at a temperature of 100 °C for a period of ~2 hours.

4.2.2 Synthesis of NIR emitting QDs

In recent years, one of the most notable advancements in biomedical research has been the use of NIR-emitting QDs for *in vivo* optical imaging and sensing. The NIR window of the electromagnetic spectrum, from 650 – 900 nm, is biologically relevant as hemoglobin and water, the major absorbers of visible and infrared light encountered during *in vivo* studies, have their lowest absorption coefficients in this region.[117] The synthesis of NIR-emitting QDs can be achieved by generation of larger sized CdTe nanocrystals, ~7-8 nm in diameter, using modified organometallic procedures. As a part of this work, a novel protocol for one-pot synthesis of CdTe(ZnS) NIR-emitting QDs using microwave-assisted synthesis was developed.[108] Microwave heating provides significant improvement over convectional metal or sand bath reactors vis-à-vis having more dynamic control over various reaction parameters of the reaction system.

A one-pot synthesis for generation of NIR CdTe(ZnS) QDs can be achieved, by modification of the nucleation and growth rate kinetics in an organometallic synthesis reaction. As discussed in the background section 4.1, during organometallic synthesis, QD nanocrystal growth occurs in two phases, namely, an instant nucleation phase between Cd^{2+} and Se^{2-} or Te^{2-} precursor and a crystal growth phase. While reaction temperature and time, which control reaction kinetics during the growth phase, can be used for size tuning of QDs, there are limitations for their use. An extremely long reaction time or high temperature, which can theoretically be used for generation of larger CdTe cores, can lead to QD size defocusing and degradation of precursor reactants proving detrimental to QD quality. The most important reaction parameters

that control the size, other than time of reaction and temperature, are concentration of the heavy metal precursors and the concentration of stabilizing ligands like TDPA.

An increase in Cd and Te precursor concentration has been known to increase the rate of growth of the QD nanocrystal and can generate larger CdTe QDs as is required for NIR emitting wavelengths.[118] Figure 4.2 shows the effect of an increase in Cd and Te precursor concentration on the PL wavelength of the resulting CdTe QDs. A recipe previously reported by Peng *et al.* was adapted for generation of CdTe QDs in a microwave reactor.[119] For this, 0.1 mmol (12.8 mg) of CdO and 0.2 mmol of TDPA was dissolved in 4.98 ml of 1-octadecene (ODE, analytical grade >95% Fluka) at 300 °C under an inert argon atmosphere. A Te stock solution, consisting of 0.05 mmol Te powder (6.4 mg) and 69 µL of TOP dissolved in 1.7 ml of ODE, was swiftly injected to the Cd precursor to yield CdTe QDs emitting at 570 nm after 10 minutes of reaction time. An increase in Cd (and Te) concentration from ~2.5 mg/ml, as used in the recipe above, to ~5 mg/ml shows a marked increase in CdTe diameter upon heating for an identical amount of time. As shown in Figure 4.2, upon doubling Cd and Te precursor concentration, CdTe PL red shifts to yield 640 nm emitting QDs. A further increase in Cd (and correspondingly Te) concentration to ~7.5 mg/ml yields CdTe QDs exhibiting PL at 655 nm. Further increase in Cd (and Te) precursor concentration did not affect the QD PL significantly.

Another parameter that could be tweaked to facilitate one-pot synthesis of NIR emitting CdTe dots is the concentration of the stabilizing TDPA ligand. In organometallic synthesis, two molecules of TDPA covalently bind to every atom of

metallic cadmium during the nucleation step.[98] An increase in the TDPA concentration from a ratio greater than 1:2, as has been used in the synthesis recipe so far, can serve to inhibit the CdTe nucleation during synthesis thus effectively increasing the concentration available for growth of CdTe QD and resulting in larger diameter QDs. For the above mentioned parameters, with Cd concentrations at 7.5 mg/ml, CdTe QDs emitting at 715 nm, as shown in Figure 4.2, were generated by increasing Cd:TDPA ratio to 1:4.

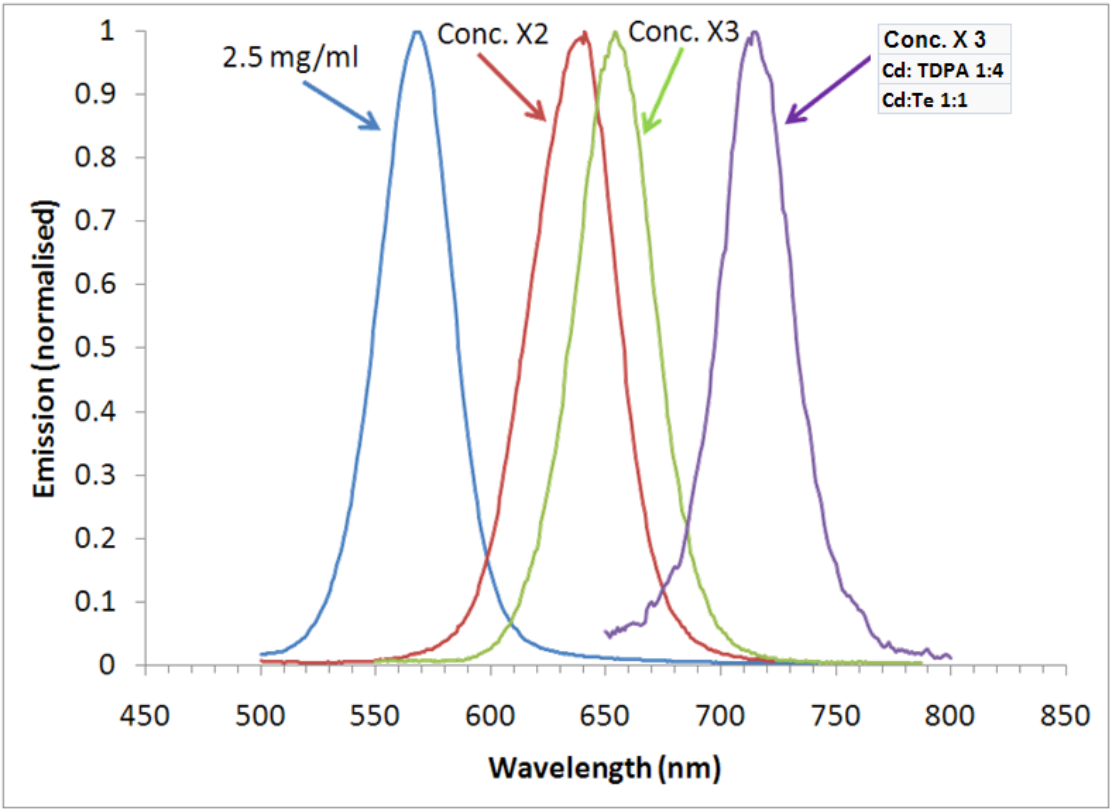

Figure 4.2 A plot showing PL spectra of CdTe QDs generated in this work.

4.3 Summary

In this chapter, a one-pot microwave-assisted approach for the generation of CdSe, CdTe and CdSe(ZnS) core(shell) QDs was demonstrated. Microwave-assisted methods provide an efficient alternative to chemical baths for synthesis of high quality QDs. The QDs generated in this study collectively span the visible and NIR range of the electromagnetic spectrum and lead onward to applications as optical sensors.

5 ON THE DESIGN OF COMPOSITE PROTEIN·QD BIOMATERIALS VIA SELF-ASSEMBLY

5.1 Introduction

One of the most significant applications of QDs is their use in optical sensing and imaging. In recent years, multiple strategies for the use of QDs in sensor design have been employed. Notable advancements for sensor design include the use of QDs embedded in polymer matrices such as thermoresponsive hydrogels,[113,120] polymer microbeads,[121] and hollow polymer microcapsules,[114] which insulate them from the external environment while maintaining their optical sensing motifs. In a similar approach, QDs could be incorporated into functional polymeric protein materials for the design of QD-based sensors. Polymeric protein materials, like collagen or elastin, have intrinsic chemical or mechanical capabilities which can complement optical properties of QDs.[122] In addition they can be functionalized with a variety of biological entities like antibodies or fluorescent proteins, thus imparting the resulting sensor with selectivity and mutlifunctionality.[123] Composite materials designed with QDs embedded in macroscale polymeric proteins have a unique potential to combine the functionality of proteins and optical properties of QDs to serve as biocompatible sensors.

Polymeric protein fibers made of recombinant Ultrabithorax (Ubx) is one potential material which can be used to design functional protein·QD composites as sensors. Monomers of recombinant Ubx protein have been shown to self assemble with relative ease under ambient conditions to form polymeric biomaterials in the form of films, fibers, sheets and tethered capsules.[124] Polymeric Ubx materials, like fibers, have

favorable mechanical properties, with high mechanical strength and elasticity,[125] and can be incorporated with functional moieties, like Enhanced Green Fluorescent Protein (EGFP).[123] Such properties of Ubx biomaterials makes them suitable candidates for study of protein·QD composites and their applications towards biochemical sensors.

5.2 Properties of the Ultrabithorax (Ubx) protein

Ubx is a 380 amino acid *Drosophila melanogaster* Hox transcription factor containing a structured DNA-binding homeodomain.[124,126,127] The amino acid sequence of Ubx is represented schematically in Figure 5.1, with negatively charged amino acids of aspartic acid and glutamic acid marked in red and positively charged arginine and lysine marked in blue. The Ubx monomer contains a net positive charge of +10 at the working pH of 8, due to an excess of arginine and lysine amino acids in the DNA binding homeodomain.

Bondos *et al.* have previously reported on the production of recombinant Ubx in *E. coli* cells, an organism with well established molecular biology protocols.[124,127] Recombinant Ubx also enables incorporation of full-length functional proteins, like EGFP, into the amino acid sequence via gene fusion, in which the gene encoding the functional protein and the *ubx* gene are placed in tandem without intervening stop codons. Expression of such a fusion gene in *E. coli* creates a single polypeptide, as schematically represented in Figure 5.1, which maintains the functionality of the appended protein and enables manipulation of the Ubx amino acid sequence to create functional materials such as EGFP-functionalized Ubx (EGFP-Ubx).[123]

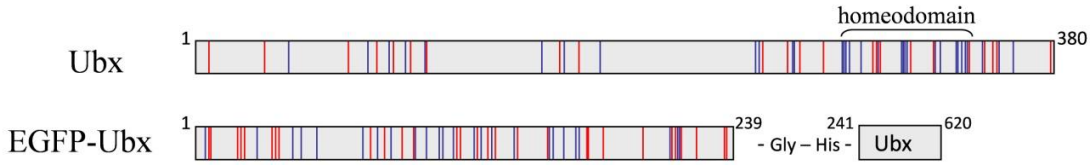

Figure 5.1 Schematic diagram of the Ubx and EGFP-Ubx protein sequences showing distribution of charges across the amino acid backbone, represented as bars. Negative charge marked in red (aspartic acid and glutamic acid), positive charges marked in blue (Arginine and Lysine).

Functionally, Hox proteins instigate position-specific developmental programs during animal growth to differentiate repeated segments into unique body structures.[126] A large fraction, >60%, of the 380 amino acid chain sequence of Ubx is disordered, potentially forming amyloid. While Ubx does not form extended aggregates as part of its native function,[124] the disordered region of the amino acid sequence presumably results in rapid self-assembly of the recombinant Ubx monomer suspended in an aqueous buffer upon exposure to air under ambient conditions. Such self-assembly of recombinant Ubx leads to generation of polymeric macroscale materials in the form of fibers, ropes and sheets and is of interest for the generation of Ubx·QD composites.[124]

5.2.1 Self-assembly of EGFP-Ubx

Previously, Bondos *et al.* have reported on the self-assembly of recombinant Ubx protein (non-EGFP) under gentle conditions at the air-water interface to form nanometer-scale fibrils and films.[124] In this, the surface of Ubx monomer containing buffer, incubated at room temperature for 2-4 hours, was reported to acquire a "matte" type appearance due to formation of a surface film. Films were drawn into robust and highly extensible fibers by means of a needle or a pipette tip.[123-125] Unlike most other

techniques, the method reported by Bondos and co-workers allows for facile synthesis of the Ubx protein in *E. coli* cells, purification to near homogeneity, and subsequent self-assembly under mild conditions in aqueous buffer. Although later stages of (non EGFP) Ubx self-assembly have been previously observed by Bondos *et al.*,[124] the generation of Ubx·QD composite materials requires a greater understanding of the oligomeric state of EGFP-Ubx at early assembly stages. Thus as a part of this work, the self-assembly of EGFP-Ubx was studied in greater detail.

5.2.2 Materials and methods: generation of EGFP-Ubx

EGFP-Ubx fusion protein was synthesized using protocols previously reported by Bondos and co-workers.[123]§ Briefly, EGFP-Ubx1a was cloned into the pET19b vector (Novagen), which appends a His-tag to the N-terminus of Ubx1a. The plasmid construct was then transformed into BL21 (DE3) pLysS *E. coli* cells. *E. coli* cultures were grown in Luria broth containing 50 μg/ml carbenicillin and 30 μg/ml chloramphenicol (LB) at 37 °C. Eight ml of an overnight culture, inoculated from a single colony, was used to inoculate a 1 L LB culture. Cultures were grown to an optical density of 0.6-0.8, at 600 nm, and subsequently cooled to 26 °C. EGFP-Ubx1a protein expression was induced with 1 mM IPTG and grown for an additional 105 minutes. Cells were harvested by centrifugation at 3500*g* for 30 min at 4 °C. Cell pellets corresponding to 1L of culture were aliquoted and stored at -20 °C. Each aliquot was thawed at room temperature, as needed, and lysed in 10 ml of lysis buffer (50 mM sodium phosphate buffer, pH 8.0, 5% glucose w/v, 500 mM NaCl, 1 protease inhibitor

§ Synthesis of EGFP-Ubx used in this work was done by members at the lab of Dr Sarah E. Bondos

tablet (Roche), 0.8 mg/L DNase I). Cell lysates were centrifuged at 17000*g* for 30 min at 4 °C. The supernatant was loaded on a nickel-nitrilotriacetic acid (Ni-NTA) agarose resin column (Qiagen), which was equilibrated with 30 ml of equilibration buffer (5% glucose w/v, 500 mM NaCl, 50mM sodium phosphate buffer, pH 8.0). The column was then washed with 50 ml volumes each of W1 buffer, W2 buffer, and W3 buffer, and 25 ml of W4 buffer (equilibration buffer containing 0mM, 20 mM, 40 mM, and 80 mM imidazole, respectively). Protein was eluted with 14 ml of elution buffer (200 mM imidazole dissolved in equilibration buffer). Concentrations of the purified EGFP-Ubx1a protein samples were determined using the BioRad protein assay (BioRad). Approximately 2 mg of dithiothreitol (DTT) was added to each 2 ml elution volume to maintain the protein in the reduced state.

5.2.3 Hierarchical self-assembly of EGFP-Ubx

EGFP-Ubx purification generates protein concentrations ≥ 0.75 mg/ml. At such concentrations, the EGFP-Ubx protein is expected to self-assemble at the air-water interface under ambient conditions. In order to study the self-assembly of EGF-Ubx under ambient conditions, the 'sessile drop' technique was used. In this approach, drops of EGFP-Ubx protein (100 μl) were placed on a strip of Parafilm™. After 15 minutes, 1 hour, and 2 hours, the surface film was sampled by floating a 100 nm thick carbon film (on previously unsampled drops), which were subsequently lifted using TEM grids, stained with phospotungstic acid (PTA, 2% w/v), and imaged by a JEOL 1200 TEM.

Upon exposure of the EGFP-Ubx protein monomers to air, the protein monomers interact with each other and initiate self-assembly. After 15 minutes of incubation, the

surfaces of the protein drops show the formation of small globular protein aggregates, typically sub-25 nm in size (Figure 5.2). These aggregates interact to form small proto-fibrils ~ 50 nm in length (Figure 5.2). Proto-fibrils further interact to form fibrils on the order of a few hundred nanometers in diameter and tens of microns in length as observed on the protein drop incubated for 2 hours (Figure 5.2).

These above observations identified three new stages in EGFP-Ubx 'hierarchical' self-assembly. In this expanded hierarchy, monomers coalesce to globular aggregates, which rearrange to form proto-fibrils and subsequently fibrils. Fibrils then form lateral associations to generate macroscopic films, which are the building blocks for various EGFP-Ubx architectures such as fibers, sheets, ropes and EGFP-Ubx bundles.[124] The presence of nanoscale order in macroscale materials makes EGFP-Ubx fibers and films attractive substrates and presents unique opportunities for incorporating nanoparticles such as luminescent QDs.

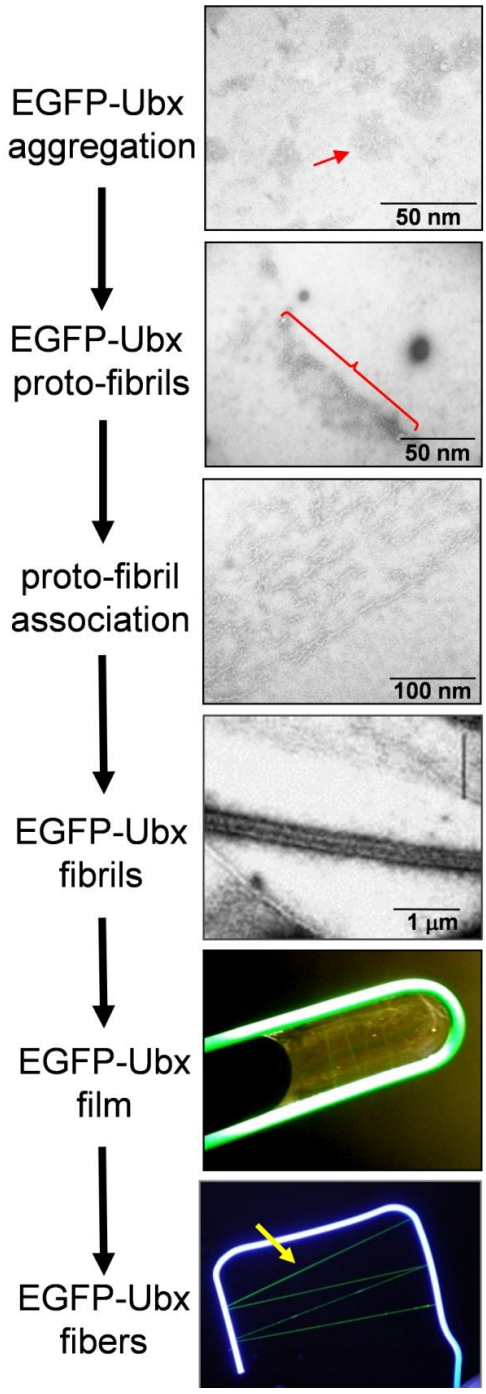

Figure 5.2 TEM images and micrographs showing hierarchical bottom-up self-assembly of EGFP-Ubx protein at the air-water interface.

5.2.4 Mechanical properties of Ubx fibers

Polymeric macroscale materials generated by the hierarchical self-assembly of the recombinant Ubx monomer have favorable mechanical properties in terms of mechanical strength and elasticity. Detailed studies on the mechanical properties of Ubx fibers by Bondos and co-workers reveal that Ubx fibers possess high extensibility, comparable to elastin, and moderate values of mechanical strength (as compared to dragline silk) making them unique materials for engineering applications. Specifically, Ubx fibers show a diameter dependent mechanical behavior in which narrow fibers, defined as having diameters less than 10 μm, show an elastic behavior with a linear stress-strain curve. The breaking stress for such elastic fibers was found to be ~40%. Conversely, the stress-strain curves of wide fibers (diameter > 15 μm) show a plastic-like behavior and have a yield point indicative of an elastic-to-plastic transition. The breaking strain of such wide fibers was found to reach up to ~150%.[125]

The differences in the mechanical behavior of Ubx fibers in correlation to fiber diameter is presumed to be a difference in fibril packing which occurs during the later stages of the Ubx self-assembly. Ubx fibers are presumed to have a central elastic core with tight fibril packing surrounded by an annular plastic region with higher disorder or lower fibril packing. According to this model, narrower fibers would have a smaller percentage of the annular plastic region inducing them with an elastic behavior. Conversely, wider fibers would have a larger annulus giving them plastic-like characteristics. This model is strongly supported by observation of surface morphology

of Ubx fibers of varying diameters before and after extensibility studies reported by Huang *et al*.[125]

Additional evidence for the above model comes from electron microscopy studies of Ubx fiber cross-sections, done as a part of this work. To observe the structure of Ubx fiber cross-section, fibers of various diameters were vapor fixed with acrolein in a closed chamber for a period of two hours.[128,129] The fibers were then transferred onto scotch tape and infiltrated overnight by a transitional solvent Quetol 651, a low viscosity aliphatic epoxide. Samples were subsequently embedded in resin by incubating at 55 ºC overnight. Thick sections (1-2 μm) of the sample containing resin block were taken for imaging on the SEM (JEOL JSM-7500F).

Cross sections of narrow fibers reveal a closely packed interior evidenced by a smooth surface observed in SEM, shown in Figure 5.3A. In contrast, cross sectional SEM images of wide fibers reveal smooth islands, similar in diameter to narrow fibers (~7 - 10 μm), surrounded by disordered regions containing fissures as shown in Figure 5.3B. Such fissures may occur naturally in wide fibers, or they may be an artifact induced by sectioning. Even if they are an artifact, their presence would still indicate a difference in fibril packing that enables fissures to form, since the narrow fibers and the cores of wide fibers both lack fissures. Thus, the plastic nature of the large fibers appears to correlate with the presence of poorly packed regions surrounding elastic, tightly packed cores.

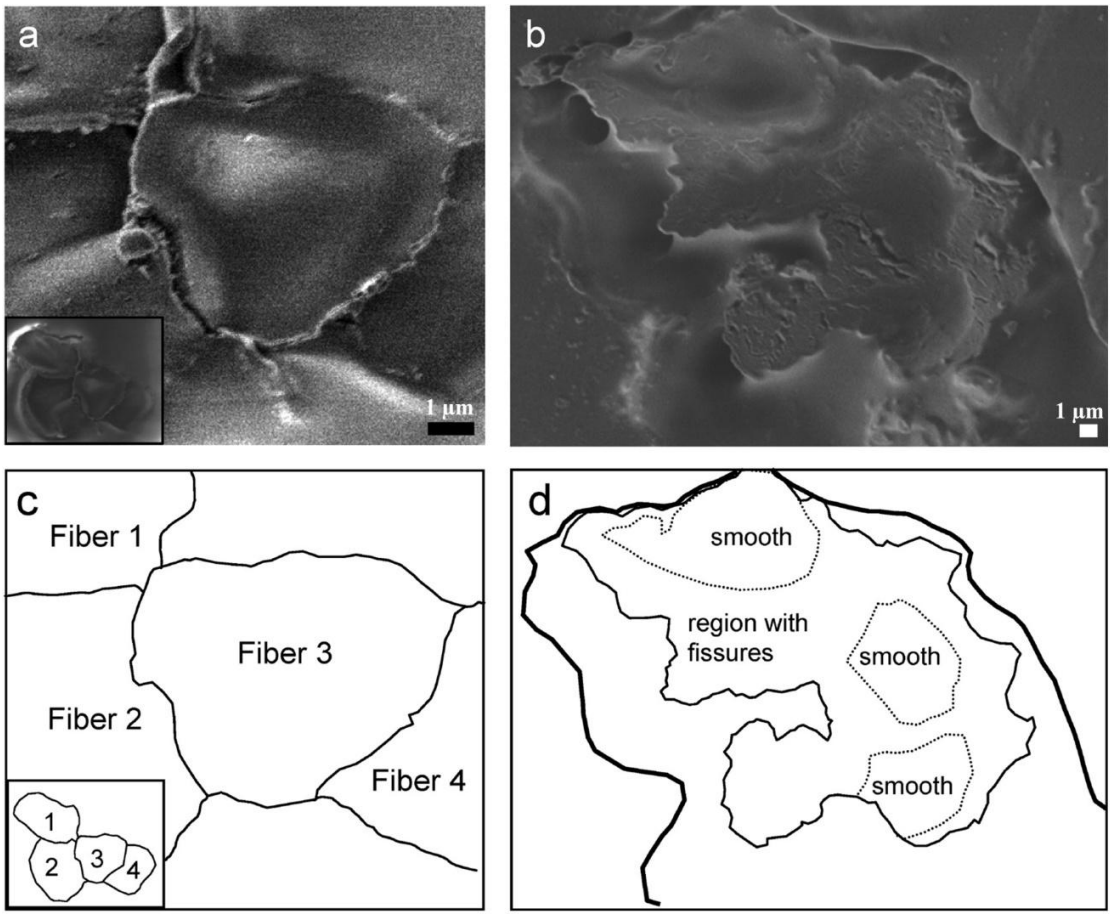

Figure 5.3 SEM of Ubx fiber cross-sections reveals fissures only in wide fibers. Cross section of a narrow fiber, part of a four fiber bundle (a, inset), is smooth and tightly packed. (a,c) In contrast, a cross-section of a wide fiber reveals three tightly packed cores surrounded by regions with gaps or fissures. (b,d)

5.3 Motifs for design of Ubx·QD composite biomaterials

The design of experiments for the generation of Ubx·QD composite biomaterials require the following considerations:

1. Dynamics of self-assembly: The nanoscale structure of EGFP-Ubx varies over time, given the hierarchical bottom-up self-assembly as observed in Figure 5.2. Thus

composite materials with different structures could potentially be generated by varying the time at which the QDs are added to EGFP-Ubx materials. QDs can either be mixed with EGFP-Ubx before the self-assembly process is initiated or added to the surface of the protein film at the air-water interface after self-assembly. When mixed with the protein monomer before self-assembly, QDs will interact individually with the EGFP-Ubx monomers to form conjugates. The extent to which such conjugates will affect and alter the hierarchical self-assembly of EGFP-Ubx is unclear owing to complexities of the EGFP-Ubx·QD system. However, it is reasonable to expect that EGFP-Ubx·QD conjugates would self-assemble under ambient conditions and generate macroscale composite materials. Conversely, QDs could also be introduced into EGFP-Ubx materials post self-assembly. In this case QDs, dropped onto the buffer meniscus after allowing for EGFP-Ubx self-assembly, would be templated above the EGFP-Ubx film which can subsequently be pulled to form EGFP-Ubx·QD fibers or sheets.

2. Ubx – QD interactions: Engineering a macroscale protein·QD composite biomaterial requires a thorough understanding of the forces that influence interactions between them. Current research efforts to understand protein-nanoparticle interactions use specific case-studies, with protein monomers coating the nanoparticle surface, and are still in its nascent stage with investigations conducted only at the nanoscale. In such cases, it has been suggested that factors such as nanoparticle size, hydrophobicity, surface charge, and surface functional groups affect protein-nanoparticle interactions.[130-134] While a study of factors affecting protein-

nanoparticle interactions at the nanoscale are important, they contribute very little to understanding of the extent to which such factors would affect material properties and design of a macroscale polymeric protein·QD composite, as is required in this study.

Given various considerations, as laid out above, for the generation of Ubx·QD composites, two different methods for synthesis of EGFP-Ubx·QD composite materials are designed and schematically represented in Figure 5.4. Primarily, two different time points, pre and post self-assembly are chosen for the generation of EGFP-Ubx·QD composites. The technique involving generation of composites when QDs are mixed with EGFP-Ubx pre self-assembly is referred to as a 'Conjugate Self-Assembly', owing to the formation of EGFP-Ubx·QD conjugates. Similarly, the technique involving 'templating' QDs on EGFP-Ubx film post self-assembly for the generation of composite materials is called 'Template Self-Assembly'.

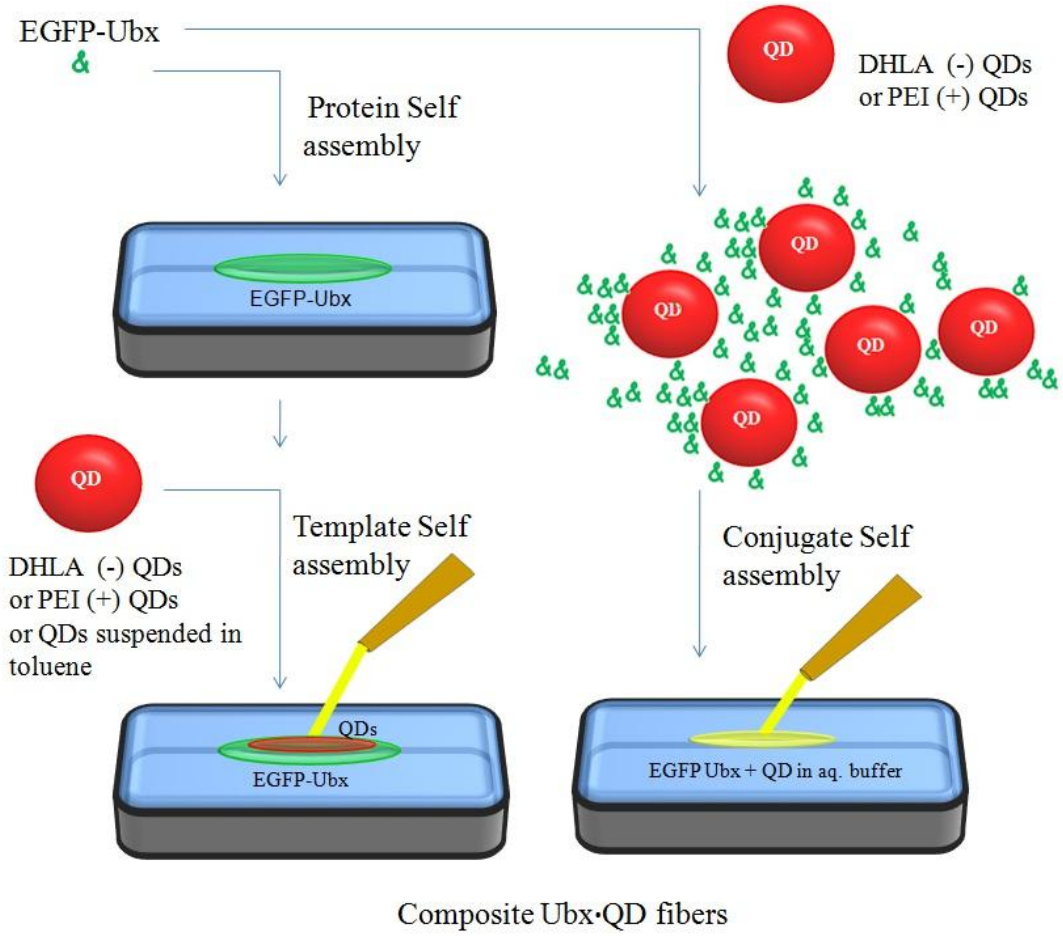

Figure 5.4 Schematic diagram representing the experimental design for generation of EGFP-Ubx·QD composite materials.

Additionally, factors perceived to be important in governing protein–nanoparticle interactions, such as nanoparticle surface charge and hydrophobicity, are evaluated in this work in terms of their effect on the composite material on a micro- to macroscale. QDs can be functionalized with a wide variety of surface chemistries commonly used with other nanoparticles. In this work, positively charged polyethyleneimine (PEI)

coated QDs (PEI-QDs)[135] exhibiting amine surface groups (-NH_2) and negatively charged dihydrolipoic acid (DHLA) coated QDs (DHLA-QDs)[136] presenting carboxylic surface groups (-COOH) are used for generation of composite EGFP-Ubx·QD materials during conjugate self-assembly. Template self-assembly offers the opportunity to incorporate hydrophobic trioctylphosphine oxide (TOPO) coated QDs (TOPO-QDs)[11,110] exhibiting hydrophobic alkane surface groups, in addition to PEI-QDs and DHLA-QDs during the generation of EGFP-Ubx·QD composites. The effect of QD surface charge and surface hydrophobicity will be evaluated in terms of resulting EGFP-Ubx·QD composite fiber surface morphology and QD distribution within the fiber. SEM and confocal microscopy will be used to evaluate these, respectively. In this work, CdSe-ZnS core-shell QDs emitting at 620 nm were chosen to be incorporated with EGFP-Ubx (emission maximum at 509 nm) to form composite materials. QDs with a narrow red PL are chosen so that the emission does not overlap that of the EGFP protein and enable an accurate evaluation of QD distribution in EGFP-Ubx·QD composite materials.

Changing surface chemistries (and simultaneously surface charges) on the QDs allows for simple optical evaluation of surface charge and hydrophobicity on the structural and mechanical properties of the resulting composite materials. *Such an understanding would be a first and important step towards the design of functional polymeric protein-nanoparticle composites for their use as biochemical sensors and is the subject of study in this dissertation.* While these studies are specific to Ubx·QD composite materials, it is believed that similar design motifs can be applied, to any self-

assembling protein and nanoparticles with similar surface chemistries, to generate polymeric protein-nanoparticle composites.

5.4 Synthesis of surface functionalized QDs

As a first step towards the generation of EGFP-Ubx·QD composites, TOPO coated QDs, synthesized by a microwave-assisted method as described in Chapter 4, were either functionalized with DHLA, giving them a negative surface charge, or coated with PEI, giving them a positive surface charge. Protocols for said functionalization were adapted from previously reports currently available in literature. Brief descriptions of each are as follows:

5.4.1 Materials and methods: DHLA coating of TOPO-QDs

Hydrophobic TOPO-CdSe(ZnS) QDs, synthesized using methods already discussed, were coated with DHLA resulting in an aqueous suspension of QDs to be used for generation of Ubx·QD composites. To increase coating efficiencies and stability of DHLA QDs, the ZnS shell on QDs was not annealed. DHLA was freshly prepared by reduction of Lipoic acid in accordance with previously reported procedures.[136] The following recipe was used:

- A, 100 ml, 0.25 M $NaHCO_3$ aqueous buffer was prepared. The buffer was deaerated by bubbling argon through it for ~1 hour to remove any dissolved oxygen and subsequently chilled to 4 °C under argon blanket for use.
- Four grams of (±)α-Lipoic acid (98%, Sigma) was added to the buffer under constant mixing. It is to be noted that lipoic acid does not completely dissolve in the aqueous buffer.

- About 2.96 g of Sodium borohydride ($NaBH_4$, 98%) was s*lowly* sprinkled in the lipoic acid solution under constant mixing. The reaction mixture foams and care should be taken to avoid spilling. Special consideration should be made for the storage of $NaBH_4$ in a moisture free environment (dessicator). Also, it is of importance that a fresh stock of $NaBH_4$ is used for the reaction.
- The mixture was allowed to react for 2 hours at 4 °C under constant mixing and an argon blanket. The resultant mixture after 2 hours should be slightly milky.
- About 15 ml of 12 M hydrochloric acid was *slowly* added to the reaction mixture to ensure complete reduction of unreacted $NaBH_4$.
- DHLA in the reaction mixture was extracted by the addition of fresh toluene. The extraction was carried out in two stages, with 50 ml of toluene in each stage. The toluene and water phases were separated using a separating funnel. An excess of anhydrous $MgSO_4$ was added to the toluene phase to remove excess water. The resulting mixture was filtered. The filtrate should be colorless and clear and contains DHLA.
- The resulting DHLA solution in toluene was concentrated by evaporating off the toluene under vacuum in a rotavapor. The boiling point of DHLA at atmospheric pressure is ~150 °C, much higher than the boiling point of toluene (110 °C). A rotavapor (IKA®) operated at 20 mm Hg vacuum pressure at a water bath temperature of 80 °C effectively separates DHLA and toluene. Care should be taken not to expose the hot DHLA to air. DHLA has a tendency to quickly oxidize back to

lipoic acid giving it a yellowish tinge in a few hours if this happens at any stage. Yellow DHLA is not ideal for QD functionalization and should be discarded.

- Evaporation of toluene should leave around 3-5 ml of pure DHLA sample. The DHLA sample may be milky. Presumably, this is due to borate salts left over from lipoic acid reduction. These salt crystals interfere with the surface exchange of DHLA on the QDs. Salt crystals, if present, can be removed by centrifugation.
- Pure DHLA is colorless, clear and viscous like oil. *Always* use a clear solution of DHLA for coating QDs (preferably after 12-24 hrs of preparation, making sure that salt crystals are not present). Pure DHLA should be stored under argon blanket at 4 °C.

TOPO-QDs were functionalized with DHLA as follows:

- About 0.5 ml of pure DHLA was added to few hundred milligrams of dry QDs and heated at ~80 °C for 10-12 hours on a hot plate with continuous stirring.
- After the reaction, the mixture was suspended in 2-3 ml of methanol. Approximately 1 g of potassium tert-butoxide (K-tBuO) was subsequently added to the mixture. K-tBuO deprotonates the carboxylic groups of DHLA on the surface of the QDs and imparts ionic stability to the nanocrystals in a basic aqueous buffer. K-tBuO should be stored in a moisture free environment. The pH of the reaction mixture at this stage should be very high (pH 10-12).
- The reaction mixture is centrifuged to pellet the QDs which are resuspended in phosphate buffer at pH 8 (9.4 mg of NaH_2PO_4 and 249.7 mg of Na_2HPO_4 in 100 ml

of DI water). The QD solution is then purified by filtration through a 0.2 µm syringe filter (Nalgene®, PES 0.2µm).

- (Optional step) For further purification to ensure the removal of excess free floating K-tBuO in the DHLA-QD solution, the DHLA-QD solution can be filtered using 100 KDa centrifuge filters. QDs were resuspended back into phosphate buffer at pH 8.

DHLA-QDs synthesized by the functionalization of TOPO-QDs, as described above, are negatively charged with a zeta potential of -12.8 ± 7.59 mV, measured using a Zeta Sizer Nano Series ZEN 3600 Spectrometer (Malvern Instruments Ltd, Malvern, Worcestershire, UK) at the working pH 8. The as synthesized DHLA-QDs had concentrations ranging from 1-3 µM. DHLA-QD concentration was measured using an empirical relationship between first exciton absorbance and CdSe nanoparticle concentration as described by Peng *et al*.[137] The PL quantum yield of DHLA-QDs, estimated using procedure previously described in section 4.2.1, was found to be ~10.1%

5.4.2 Materials and methods: PEI coating of TOPO-QDs

TOPO-QDs were coated with high molecular weight branched polyethyleneimine (PEI) (Aldrich, MW 25,000) using a modified procedure previously reported by Nann *et al*.[135] Briefly, 1 ml of 10 mg/ml solution of PEI in chloroform was mixed with 1 ml of 4-5 µM QDs solution in chloroform. The mixture was tumbled overnight at room temperature. QDs were precipitated from the mixture by addition of excess cyclohexane (Sigma-Aldrich, >99%) followed by centrifugation and resuspension in DI water. Excess PEI was extracted from the aqueous QD solution by addition of fresh chloroform. Chloroform and water, being immiscible, can be phase separated, a

process which can be accelerated by centrifugation. PEI-QDs, suspended in the lighter aqueous phase, were removed by pipetting. PEI-QDs generated by this technique have concentrations ranging from 1-3 μM and PL quantum yield of 11.1% The $–NH_2$ terminated PEI-QDs are positively charged with a zeta potential of +29.7 ± 6.2 mV.

5.5 Generation of EGFP-Ubx·QD composites by conjugate self-assembly

5.5.1 Materials and methods

The generation of EGFP-Ubx·QD composites by conjugate self-assembly, which involves mixing of functionalized QDs suspended in aqueous buffers, is discussed in this section. To generate EGFP-Ubx·QD fibers, the buffer reservoir method is used.[123] In this approach, the EGFP-Ubx protein fraction is diluted in buffer and incubated for 4 hours in a Teflon-coated tray. This technique extends the self-assembly time and surface area of the EGFP-Ubx protein, as compared to the sessile drop method, used earlier in section 5.2.1, thereby allowing greater opportunities for EGFP-Ubx/QD interaction.

In the conjugate self-assembly technique, 1-2 ml of 2-4 μM QDs (DHLA or PEI functionalized) were mixed with ~600 ml of equilibration buffer (5% glucose w/v, 500 mM NaCl, 50 mM sodium phosphate buffer, pH 8.0). EGFP-Ubx protein fractions (0.6-1.2 mg) were then added dropwise to the QD-buffer mixture contained in Teflon-coated trays. The tray was loosely covered and allowed to incubate for 4 hours under ambient conditions. A rectangular plastic bar was placed across the back of the tray surface and slowly advanced to the front one-third of the tray. Islands of composite EGFP-Ubx·QD film on the tray surface were effectively concentrated in this area, facilitating the harvest of composite fibers using a U-bend in a partially unfolded paper clip (hereafter termed

‘metal wire’ as shown in Figure 5.2). The conjugate self-assembly technique was been employed for the generation of composite EGFP-Ubx·QD fibers and sheets for DHLA-QDs as well as PEI-QDs.

5.5.2 Analysis of EGFP-Ubx·QD composites via conjugate self-assembly

Composite EGFP-Ubx·QD sheets can be lifted from trays having higher protein concentrations using a metal wire. Figure 5.5 shows the room temperature PL spectra for one such sheet containing DHLA-QDs. EGFP-Ubx·QD sheets were used instead of fibers to facilitate data collection in a commercial PTI spectrofluorometer (PTI QuantaMaster™ with a Xe Arc lamp excitation). As seen in Figure 5.5, when excited at 488 nm, the QDs and EGFP emit at 620 and 510 nm, respectively. No significant spectral shift was observed for either material. QDs have a broad absorption, whereas the absorption maximum of EGFP is at 488 nm. Under 400 nm light excitation, where EGFP has a very low extinction coefficient, the QD emission dominates and their presence inside the composite sheets can be identified.

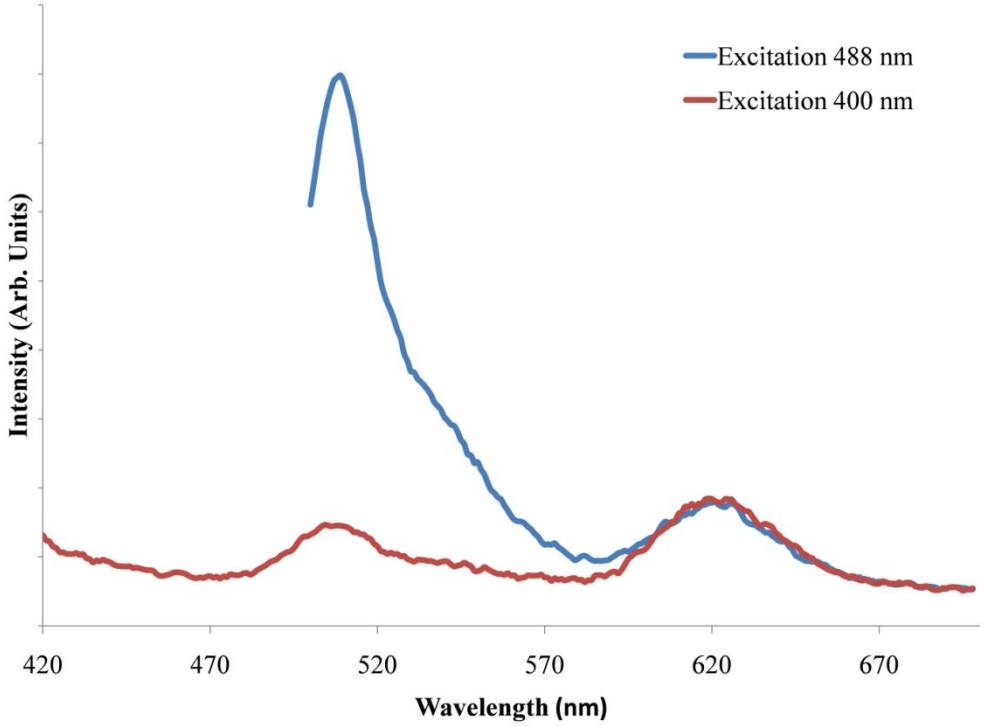

Figure 5.5 Emission spectrum of composite EGFP-Ubx·DHLA-QD films excited at 488 nm (blue line) and 400 nm (red line). Only QDs emit when excited at 400 nm thus, confirming their presence in the composite materials.

Confocal microscopy (Leica TCS SP5) has been used to confirm the presence of QDs in the composite fibers. For confocal microscopy of EGFP-Ubx·QD fibers, EGFP-Ubx was excited using a 488 nm laser with emission collected from 510 nm - 560 nm. QDs emitting at 620 nm were excited with a 458 nm laser with emission collected from 590 – 650 nm. The above confocal settings allow for very little crosstalk between the EGFP and QD channels, thus facilitating evaluation of QD distribution in the composite fibers. Figure 5.6 shows single plane confocal images, of the QD channel inside the composite fibers showing a homogeneous QD distribution for both PEI- and DHLA-QD composite fibers. It is worth noting that nanomolar concentrations of Ubx can associate with both the negatively and positively charged QDs, also at nanomolar concentrations, in the incubation buffer (1-2 ml of 2-4 μM QDs in 600 ml of incubation buffer).

For composite fibers generated with the conjugate self-assembly technique, SEM images show consistent variation in surface morphology for EGFP-Ubx·DHLA-QD and EGFP-Ubx· PEI-QD fibers across multiple samples. Axial ridges, separated by smooth regions, are seen consistently along the length of EGFP-Ubx·PEI-QDs composite fibers, shown in Figure 5.7A. In contrast, EGFP-Ubx·DHLA-QD fibers show a rougher morphology diameter with pronounced ridges, shown in Figure 5.7B. The surface of EGFP-Ubx fibers (with no QDs) is comparatively smooth, as shown in Figure 5.7C. Thus, mixing the QDs with the incubation buffer increases surface roughness of the composite fiber for both cases. Additionally, variations in fiber morphology are also observed between the EGFP-Ubx·PEI-QDs fibers and EGFP-Ubx·DHLA-QDs fibers

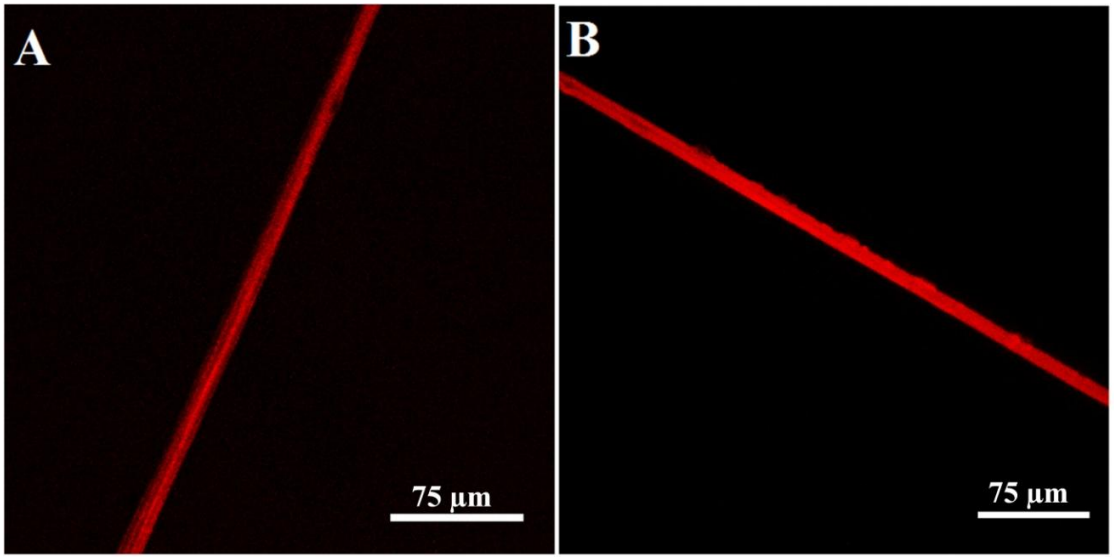

Figure 5.6 Confocal images (QD channel only) of composite EGFP-Ubx·QD fibers generated by the conjugate self assembly technique with PEI- QDs (A) and DHLA-QDs (B) showing homogeneous QD distribution.

The combination of functional groups and charge on the surface of the quantum dots, which is known to affect protein-nanoparticle interactions,[130,132-134] appears to impact the surface morphology of the composite EGFP-Ubx·QD fibers. At the working pH 8 of the incubation buffer, the –COOH terminated DHLA-QDs are negatively charged (zeta potential: -12.8 mV) while the $–NH_2$ terminated PEI-QDs are positively charged. (zeta potential: +29.7 mV). Nanoparticle size, another factor known to play an important role in protein-nanoparticle interactions,[133] is not a contributing factor in this case since the hydrodynamic diameters of the QDs are similar.[135,138] The differences between the two systems of aqueous QDs and the effect of surface charge can be observed clearly in confocal images of the composite films in Figure 5.8. The composite

film, formed on the meniscus of the buffer during the conjugate self-assembly, was sampled with a glass cover slip. The EGFP-Ubx·QD composite film crystallized on the glass coverslip while drying and was subsequently imaged by confocal microscopy. Negatively charged DHLA-QDs (in red, Figure 5.8A) seem to systematically associate within the EGFP-Ubx protein crystals (in green, Figure 5.8A), at times disrupting the crystalline structure. The DHLA-QDs align along the 'backbone' of the protein crystals, a pattern observed across entire samples spanning several hundred microns in length. However, the positively charged PEI-QDs (in red, Figure 5.8B) are conspicuously absent within the protein crystals (in green, Figure 5.8B) and instead concentrate in inhomogeneous 'halos' surrounding the crystals. This selective inclusion/exclusion of QDs within the EGFP-Ubx protein could be attributed to both a difference in surface charge and surface functional groups on the nanoparticles.

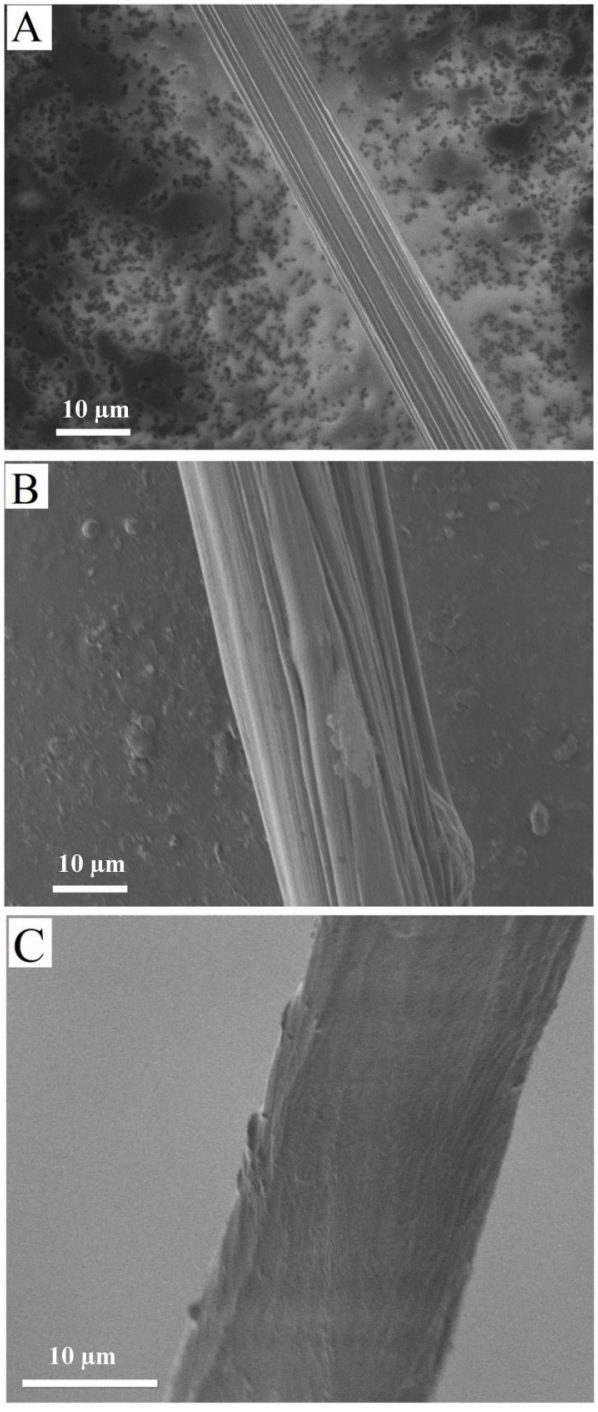

Figure 5.7 SEM images of composite EGFP-Ubx·QD fibers pulled via the conjugate self-assembly technique showing EGFP-Ubx·PEI-QDs fibers, (A) EGFP-Ubx·DHLA-QDs fibers (B) and EGFP-Ubx fibers. (C)

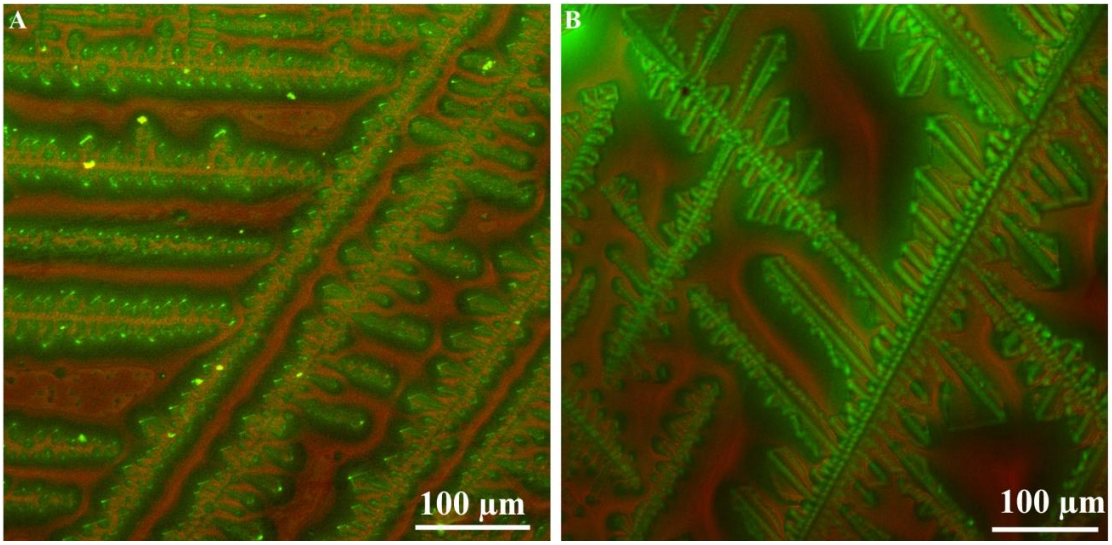

Figure 5.8 Confocal images of the surface of the buffer containing composite EGFP-Ubx·QD films during conjugate self-assembly. Green areas correspond to crystallized EGFP-Ubx and Red to QDs. EGFP-Ubx·DHLA-QD, (A) EGFP-Ubx·PEI-QD. (B)

5.6 Generation of EGFP-Ubx·QD composites by template self-assembly

In this work, EGFP-Ubx·QD composites are also generated by the template self-assembly method. For this, using the buffer reservoir method, EGFP-Ubx protein is diluted in ~600 ml of incubation buffer and allowed to self-assemble for a period of 4 hours. A rectangular plastic bar, placed across the back of the tray, is used to concentrate the protein film to one-third the initial surface area. QDs are gently added dropwise onto the EGFP-Ubx film at the air-water interface and rest above the meniscus. Composite fibers are generated by drawing the templated composite film upwards, through the QD drop, by means of a metal wire. In this template self-assembly, both the time and surface

area over which the QDs interact with the EGFP-Ubx protein is smaller compared to the conjugate self-assembly method.

In addition to QDs in aqueous buffers, QDs suspended in toluene – an apolar solvent – were also used to generate composite fibers. Hydrophobic TOPO-QDs suspended in toluene also rest above the meniscus of the self-assembled protein-containing buffer. Although EGFP-Ubx fibers can easily be pulled from areas on the buffer meniscus where QDs in toluene were not added, the apolar solvent and TOPO-QDs increases the degree of difficulty of pulling EGFP-Ubx·QD composite fibers through the toluene-water interface. TOPO-QDs in toluene appear to disrupt Ubx self-assembly: Ubx fibers snap when pulled through a toluene drop containing QDs from the air-water interface. Consequently, composite EGFP-Ubx·TOPO-QD fibers were pulled from the meniscus after evaporation of the apolar solvent.

5.6.1 Analysis of EGFP-Ubx·QD composites via template self-assembly

Fiber morphology and QD distribution were studied for all EGFP-Ubx·QD fibers generated by the template self-assembly technique. Both EGFP-Ubx·DHLA-QD and EGFP-Ubx·PEI-QD fibers appear smoother (Figure 5.9A&B) than their corresponding counterparts obtained via the conjugate self-assembly method (Figure 5.7A&B respectively). When compared to EGFP-Ubx fibers (Figure 5.7C), subtle variations are observed as small ridges for EGFP-Ubx·PEI-QD fibers and uneven surface morphology for EGFP-Ubx·DHLA-QD fibers. The template self-assembly technique, which reduces Ubx·QD interactions due to both a smaller surface area and a shorter interaction time, appears to cause fewer disruptions to EGFP-Ubx self-assembly. Thus, the extent of

nanoscale interactions between the EGFP-Ubx protein and the QDs is reflected on the microscale by the surface morphology of the Ubx-QD fibers.

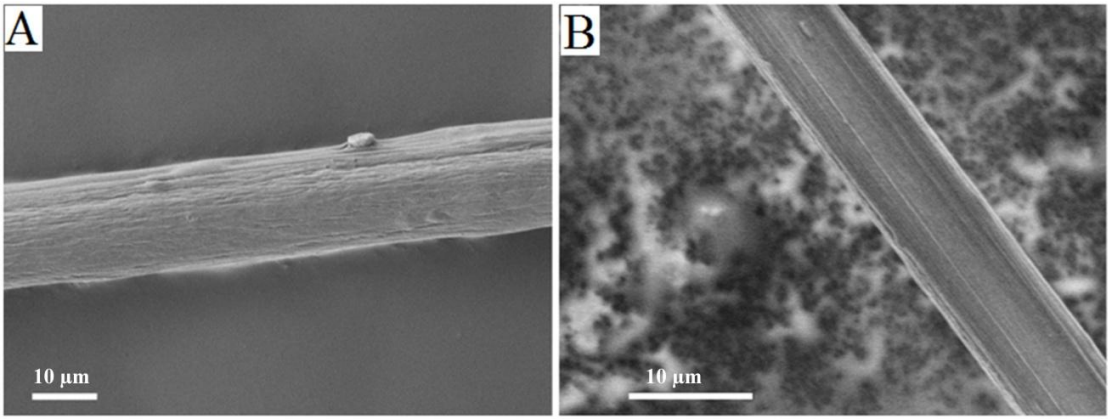

Figure 5.9 SEM image of EGFP-Ubx·DHLA-QD fiber (A) and (B) EGFP-Ubx·PEI-QD fiber pulled via the template self-assembly technique.

Despite these morphological similarities, QD distribution inside the EGFP-Ubx·DHLA-QD and EGFP-Ubx·PEI-QD fibers reveals interesting differences. Single plane confocal images, obtained using identical instrument settings as earlier experiments, inside the composite fibers show that QD distribution in EGFP-Ubx·DHLA-QD fibers is homogeneous on the microscale (Figure 5.10A, inset showing emission from QDs only). While the QDs are distributed throughout the protein component of EGFP-Ubx·PEI-QDs composite fibers, they also pack in a protein-depleted central core along the length of the fiber (Figure 5.10B). Inhomogeneously distributed pockets of such PEI-QD cores, occupying areas ranging from 0 to 60% of the fiber diameter, are frequently observed for multiple samples. Again, differences in QD distribution between EGFP-Ubx·PEI-QD and EGFP-Ubx·DHLA-QD fibers could be

attributed to the different surface charge and functional groups on the coated QDs. Evidence that DHLA-QDs and PEI-QDs interact differently with EGFP-Ubx was presented in Figure 5.8. The formation of QD-rich cores for the EGFP-Ubx·PEI-QD fibers formed by the template self-assembly technique thus reflects the nanoscale effects of nanoparticle surface charge.

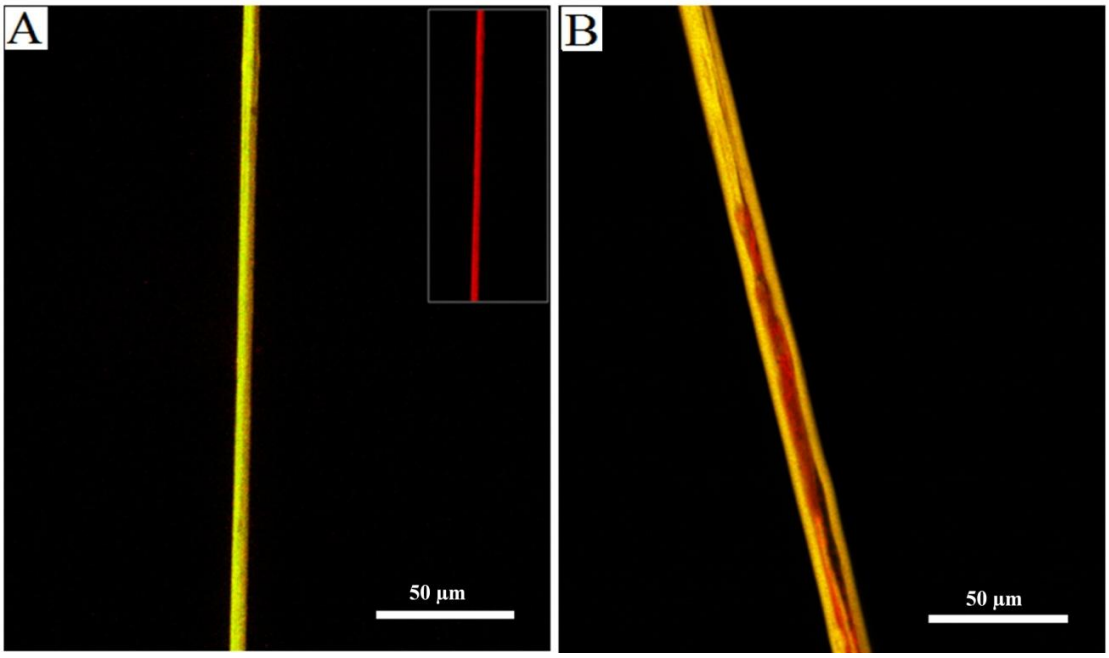

Figure 5.10 A single plane confocal image of EGFP-Ubx·DHLA-QD fiber (A) showing homogeneous QD distribution. (Inset, QD emission only) Confocal image of EGFP-Ubx·PEI-QD fiber showing an inhomogeneous QD distribution with QD concentrated cores. (B)

For EGFP-Ubx·TOPO-QD fibers, SEM images reveal large fissures along the length of the fiber (Figure 5.11A). Single plane confocal images of the composite fiber show a very heterogeneous distribution of TOPO·QDs in the composite fiber (Figure 5.11B). Similar fissure-containing fibers are obtained by the action of toluene in absence of nanoparticles, demonstrating that the introduction of toluene, and not the TOPO-QDs, primarily disrupts EGFP-Ubx self-assembly (Figure 5.11C). The lack of such fissures in the EGFP-Ubx·PEI-QD or EGFP-Ubx·DHLA-QD fibers described so far confirms that the alteration in protein structure is primarily due to the apolar solvent rather than interactions with the QDs. Consistent with such observations, organic solvents of different polarities are known to alter protein structure and mechanical properties in cases of elastomeric proteins like dragline silk.[139] The ability to create composite EGFP-Ubx materials using hydrophobic nanoparticles greatly extends the range of potential inorganic nanoparticles that could be incorporated into protein materials.

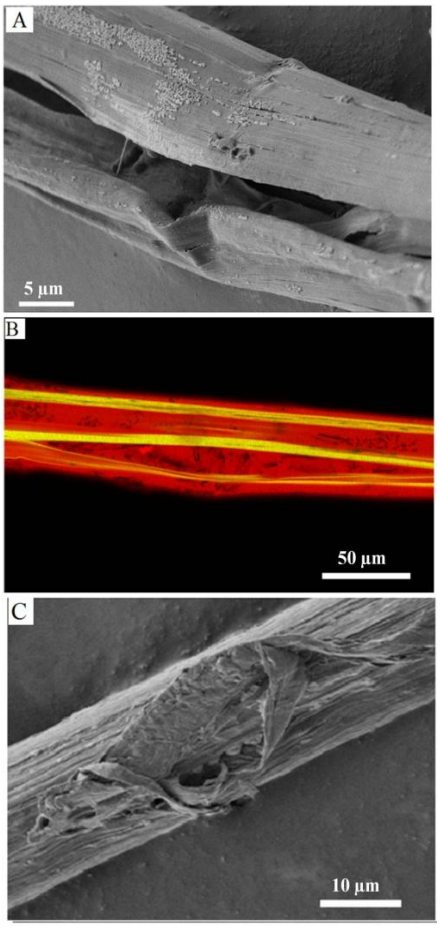

Figure 5.11 SEM image of EGFP-Ubx·TOPO-QD fiber pulled by the template self assembly technique with QDs in toluene (A) Confocal image of the same fiber showing heterogeneous distribution of QDs in which regions with only QDs (Red) are interspersed with regions containing QDs and EGFP-Ubx (yellow) (B). A SEM image of EGFP-Ubx fibers drawn by addition of toluene on the air-water interface containing EGFP-Ubx film. (C)

5.7 Comparison between conjugate and template self-assembly techniques and effect of QD surface charge

In the experiments described thus far, variations in the surface morphology and QD distribution have been observed between the two techniques of composite fiber generation. These results are summarized in Table 5.1. Nanoscale interactions between EGFP-Ubx and QDs, spanning an extended time period and large surface area in the conjugate self-assembly technique, result in microscale variations of surface morphology of composite fibers. Such changes in fiber surface morphology are absent in materials generated by template self-assembly. This represents a unique design motif wherein the surface roughness of a protein fiber can be altered by varying the time of introduction of nanoparticles during the hierarchical self-assembly process of the Ubx protein.

	Ubx fibers	Composite Ubx·QD by conjugate self-assembly		Composite Ubx·QD by template self-assembly		
QD coating	N/A	PEI-QDs	DHLA-QDs	PEI-QDs	DHLA-QDs	TOPO-QDs
QD distribution	N/A	Homogeneous	Homogeneous	Inhomogeneous	Homogeneous	Heterogeneous
Surface Morphology	Smooth	Rough	Rough	Smooth. (with small ridges)	Smooth	Very Rough
Ease of synthesis	Easy	Easy	Easy	Easy	Easy	Difficult

Table 5.1 Summary of observations of EGFP-Ubx·QD composite fibers generated in this work.

Differences in QD surface chemistry and charge seem to affect EGFP-Ubx·QD interactions. Composite fibers generated by the conjugate self-assembly technique, which allows for maximum nanoscale interaction between the QDs and the EGFP-Ubx protein, appears to have a homogeneous QD distribution using QDs with either surface charge. This occurs despite the differences between films as observed by confocal microscopy in Figure 5.8. Therefore, it is plausible that differences in QD distribution do exist in composite fibers generated by conjugate self-assembly, but on a scale which falls below the resolution of confocal microscopy. Attempts to image the internal structure of composite fibers at the nanoscale were inconclusive due to the mechanical properties of the fibers, which precluded thin sectioning.[125]

The EGFP-Ubx sequence** has a net charge of +1 at the working pH 8. While the protein has positively charged amino acids (R and K, arginine and lysine) and negatively charged amino acids (D and E, aspartic acid and glutamic acid) distributed across the sequence, predominant negatively and positively charged regions do exist within the EGFP-Ubx sequence. EGFP, fused to the N terminus of the Ubx, carries a net negative charge (-8) at the working pH, whereas the homeodomain, a portion of the Ubx sequence, has a net charge of +10. Such charged regions suggest that the negatively charged DHLA-QDs could associate with the positively charged homeodomain to a greater degree than the rest of the sequence. By the same logic, the positively charged PEI-QDs may associate with EGFP or the negatively charged D and E amino acids in the remainder of the Ubx sequence, which largely lacks secondary structure.[127] Due to

** The Ubx sequence is given in Appendix B

charge repulsion, such interactions are most likely to happen outside of the homeodomain. Control experiments were conducted to determine if QD surface charge affects which portion of the protein sequence is bound, and thereby deduce whether it impacts composite fiber formation by conjugate self-assembly.

Composite fibers were generated using Ubx lacking the EGFP fusion to test whether EGFP is required for interactions with PEI-QDs. Confocal images of Ubx·QD fibers (PEI-QDs and DHLA-QDs) do not show any significant differences, as observed in Figure 5.12, indicating the disordered region of Ubx is sufficient for PEI-QD interaction. Composite fibers were also generated by the conjugate self-assembly technique for both DHLA-QDs and PEI-QDs using N216-Ubx. N216-Ubx is a minimal materials-forming region within the Ubx sequence. This construct lacks the negatively charged EGFP fusion as well as the first 215 amino acids of the Ubx sequence.[124] The charge of N216-Ubx is dominated by the positively charged homeodomain which accounts for ~37% of the N216-Ubx amino acid sequence. Fibers constructed of N216-Ubx retain normal morphology and are robust to handling. Single plane images of N216-Ubx·QD (both Pei-QDs and DHLA-QDs) were obtained at identical confocal microscope settings, as shown in Figure 5.13. The images were imported into MATLAB® and signal intensity per pixel corresponding to the fiber was calculated. Signal intensity per pixel for N216-Ubx·DHLA QDs fibers was found to be 2.5x higher than that of N216-Ubx·PEI QDs. Therefore, the differences in QD interaction can be attributed, at least in part, to the C-terminal 165 amino acids (43%) of Ubx. This

validates the hypothesis that surface charge and functional groups on the nanoparticle do play a significant role in the nanoparticle-protein conjugate self-assembly process.

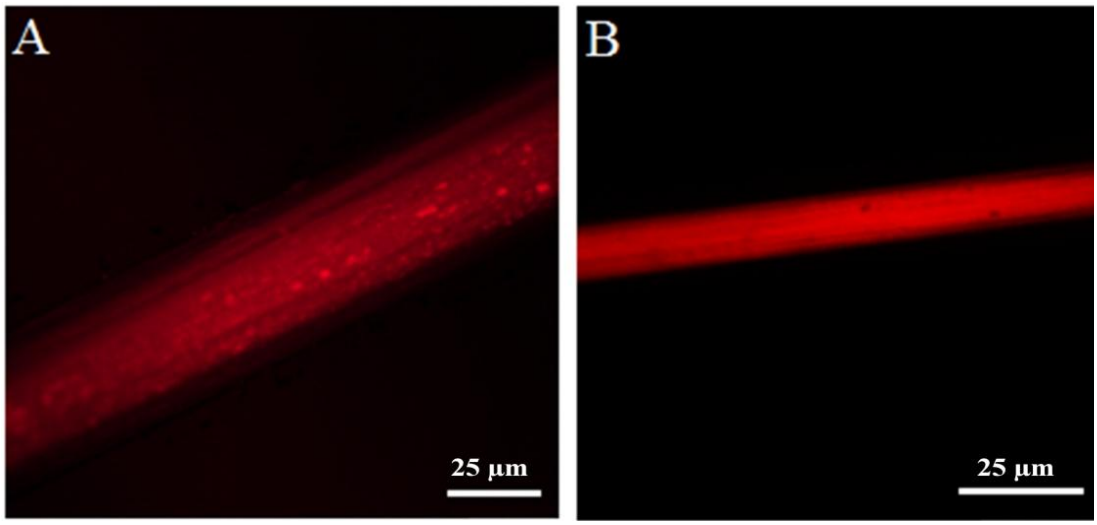

Figure 5.12 A single plane confocal images of (non EGFP tagged) Ubx·DHLA-QD (A) and Ubx·PEI-QD (B) fibers pulled via the conjugate self-assembly technique.

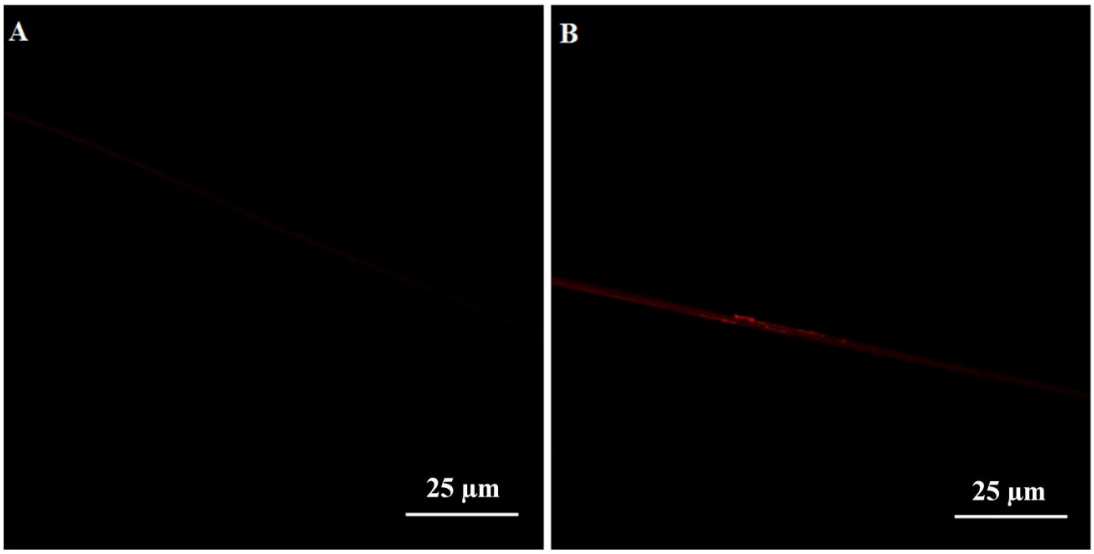

Figure 5.13 A single plane confocal images taken at identical confocal settings of N216-Ubx·PEI QDs (A) and N216-Ubx·DHLA QDs fibers (B) pulled via the conjugate self assembly technique.

5.8 Summary

In this work, an array of Ubx·QD composite fibers with different fiber morphologies and varying nanoparticle distributions have been synthesized by a bottom-up self-assembly process. QDs introduced at different stages of the EGFP-Ubx hierarchical self-assembly process controllably vary fiber morphology. QDs introduced prior to the initiation of the EGFP-Ubx protein self-assembly introduce a higher amount of surface roughness as compared to introduction of nanoparticles post self-assembly. This represents a unique strategy to induce surface roughness in protein materials generated by bottom-up self-assembly techniques. Furthermore, differences in QD surface functional groups and surface charge affects self-assembly leading to varying nanoparticle distributions within macroscale materials. Positively charged QDs, which

interact differently than negatively charged QDs, partake in inhomogeneous nanoparticle distributions observed both in films, formed at the air-water interface, and in fibers. Further investigations, using the minimal materials-forming region within the Ubx sequence, show that the amine-terminated positively charged QDs associate themselves to a lesser degree with the positive charge carrying Ubx homeodomain than the carboxyl terminated negatively charged QDs. While these studies are specific to Ubx·QD composite materials, it is believed that similar design motifs can be applied to any self-assembling protein and nanoparticles with similar surface chemistries to generate polymeric protein-nanoparticle composites.

6 CONCLUSIONS AND FUTURE WORK

In this dissertation, the applicability of a microwave-assisted approach for the generation of II-VI semiconductor nanoparticles was evaluated. Specific case-studies demonstrating the use of a microwave-based approach for the generation of quasi 1-D multi-legged ZnO nanopods with sub-20 nm diameters and 0-D Cd-based QDs were a part of this dissertation. Further, optical sensing studies including a first ever sub-20 nm ZnO nanostructure optical humidity sensor was done as a part of this study. Additionally, the design of EGFP-Ubx·QD fibers, a macroscale polymeric bionanocomposite with potential optical biosensing opportunities, via hierarchical self-assembly was realized in this work.

Multiple research opportunities which could not be pursued in great detail, due to practical resource limitations, presented themselves over the course of this work. The following sections include notable research directions which may be pursed as a consequence of results presented in this dissertation.

6.1 Continuous flow design for microwave-assisted methods

A high power density inside a single-mode microwave cavity accompanied by uniform molecular-level heating gives impetus to the use of microwave irradiation for reaction systems requiring a high degree of control over reaction parameters, such as the ones designed to synthesize nanoparticles. The use of a microwave-assisted approach is favorable for many reasons which include generation of high quality nanocrystals, shorter reaction times, and fewer post-processing reaction steps. These advantages come

in addition to the versatility offered by solution-based reaction systems making the use of microwaves for nanoparticle generation a commercially-viable prospect.

While a microwave-based approach for nanoparticle synthesis, as demonstrated in this work, provides numerous advantages, it faces one minor drawback. Single-mode microwave cavity is volume-limited by design.[29] This restricts sample volume, consequently making large-scale nanoparticle synthesis cumbersome. Process scale-up for generation of ZnO nanopods and Cd-based QDs is limited by the volume of the single-mode microwave cavity. A potential solution for large scale synthesis of nanoparticles, like ZnO and QDs, is the use of continuous-flow systems. A continuous-flow system designed to mix desired reactants and provide appropriate residence heating times inside the microwave-cavity can potentially generate nanomaterials at a larger scale while keeping actual reaction volumes small. Such a system would circumvent a long standing challenge with large-scale nanoparticle synthesis, the loss of nanoparticle size monodispersity, and simultaneously maintain a high degree of control over reaction process parameters. Modifications in the design of microwave-based reaction systems for the use of continuous-flow processes is an attractive area of research with significant potential for technology commercialization

6.2 Future research directions with ZnO nanostructures

6.2.1 Heterogonous nucleation with changes in ZnO seed concentration

ZnO nanopods generated in this work utilized 100 µL of a 2.9 µM solution of ~4 nm 0-D ZnO seeds for heterogeneous nucleation. While the presence of seeds has been clearly shown to affect resulting ZnO nanostructure morphology, a detailed study varying seed concentration was not done. A preliminary analysis of the variation in ZnO nanostructure (nanorod) diameter versus seed concentration used for synthesis, with nanostructure measurements made using TEM, reveals almost a quadratic trend between the two, as observed in Figure 6.1. For this, ZnO nanostructures were generated at a reaction time of 20 minutes at 170 °C. A further increase in seed concentration shows the presence of unreacted seeds, indicating incomplete nucleation stage after 20 minutes. A detailed analysis at higher seed concentrations, to determine the feasibility of further reduction in resulting 1-D ZnO nanostructure diameters, remains to be done. Such a study would involve longer reaction times which are not feasible given the undesirable role of Zn silicates in the CEM microwave system. Longer reaction times would involve the use of Teflon-lined reaction vessels and would require significant redesign of the microwave reactor.

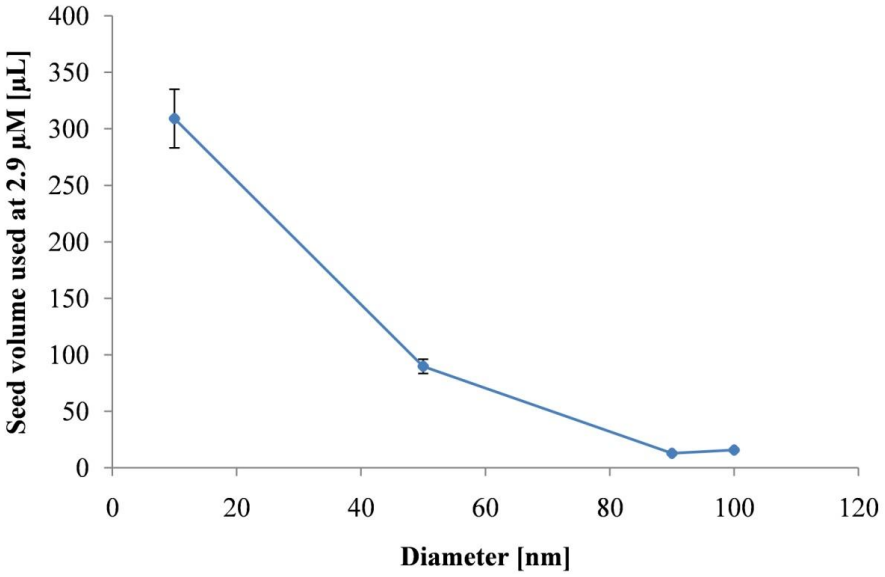

Figure 6.1 ZnO nanorod diameters as a function of amount of seeds used during heterogeneous nucleation

6.2.2 Optical gas sensing with ZnO nanopods

The use of ZnO nanopods as optical humidity sensors, as presented in this work, serves as a proof of concept for the use of ZnO nanostructures in chemical gas sensing. As mentioned earlier, very few reports demonstrating the use of ZnO nanostructures as optical sensors can be currently found in the literature. A detailed study on the dynamics and sensitivity of ZnO nanostructures as optical sensors for environmentally relevant gases like CO, CO_2 and NO_x is of high interest.

A potential roadblock for the use of ZnO nanostructures as optical sensors is the loss of PL signal upon UV excitation due to surface charging effects. As demonstrated earlier, photobleaching, occurring due to surface charge accumulation, is reversible and

can be circumvented by the use of periodic excitation at low fluence in case of ZnO nanopods. A preliminary study to estimate the extent of photobleaching in various ZnO structures generated in this work, namely, microrods generated by homogeneous synthesis, nanopods generated by heterogeneous synthesis and 0-D seeds, shows that photobleaching has a strong relationship with the overall dimensions of the ZnO structure. ZnO seeds, with diameters of ~4 nm, lose ~68% of their PL upon continuous 350 nm excitation at fluence of ~30 mW/cm^2 for a period of 5 minutes. (Figure 6.2) Meanwhile microrods, with diameters of 380 nm, lose only ~12% of their signal under identical experimental conditions. Thus the advantages of a high surface area to volume ratio, which provides ZnO nanostructures with higher sensitivity, are offset by such photobleaching effects. This study indicates that 1-D ZnO nanostructures with diameters in the 10-20 nm range provide an reasonable trade off and are ideally suited for optical chemical gas sensing studies.

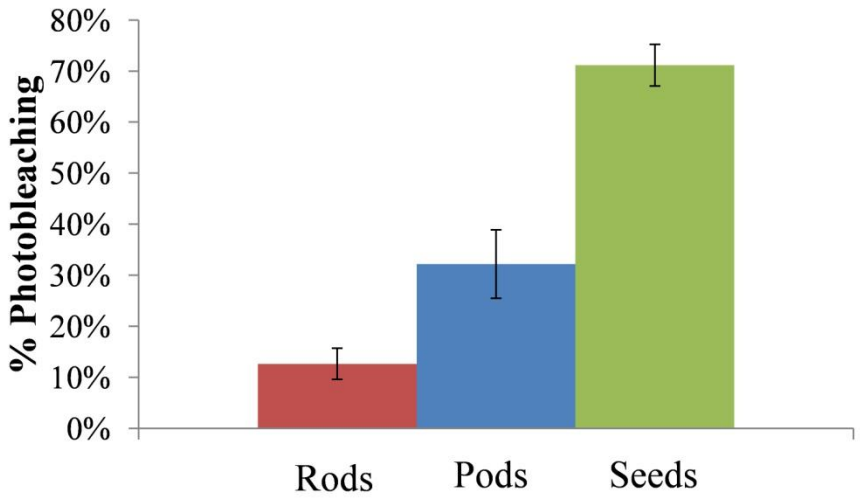

Figure 6.2 Photobleaching observed in different ZnO structures after 5 minutes of continuous UV excitation

6.3 Future research directions with Ubx·QD biomaterials

6.3.1 Mechanical properties of Ubx·QD biomaterials

One of the more favorable properties of Ubx fibers are their mechanical properties, as previously discussed in section 5.2.4. Specifically, a diameter dependent breaking strain (0.25-0.55) combined with moderately high Young's modulus makes Ubx fibers an interesting material for use as stress-strain sensors. Naturally, a study evaluating the effect of nanoparticles, such as QDs, to the mechanical properties of Ubx-based composite materials is of high interest. Such a study would be a significant step in evaluating the applicability of Ubx nanocomposites as materials for sensor applications.

In order to evaluate the effect of QDs on the mechanical properties of EGFP-Ubx, preliminary experiments were conducted as a part of this work. To generate fibers

for these experiments, identical concentrations (0.5 mg/ml) of EGFP-Ubx protein monomer was used with both PEI- and DHLA-QDs in separate Teflon-coated trays. EGFP-Ubx·QD fibers with lengths ranging from 0.2-0.4 cm were manually pulled using conjugate self-assembly technique. Breaking strains measured as a ratio of change in length per unit original length were measured for each fiber.

EGFP-Ubx·PEI-QD fibers with diameters of 7.77 ± 0.2 μm were generated and had a breaking strain of 3.25 ± 0.89. For EGFP-Ubx·DHLA-QD fibers, the diameter was 4.76 ± 0.22 μm and had a breaking strain of 2.35 ± 1.12. Previous experiments on Ubx fibers indicate that the breaking strain of fibers in this diameter range are not dependent on fiber diameter.[125] Therefore both types of composite EGFP-Ubx·QD fibers demonstrate significantly greater breaking strains than Ubx fibers (0.25-0.55) in this diameter range.[125] A significant increase in extensibility as is observed in preliminary experiments validates the potential of Ubx·QD composites. Changes in mechanical properties could be attributed to a variety of factors, including a variation in nanoparticle homogeneity within composite materials, and would require a detailed study.

6.3.2 Nanoparticle distribution in Ubx·QD composites

The distribution of PL QDs inside EGFP-Ubx ·QD composites, with respect to QD surface charge and method of nanoparticle addition (conjugate or template methods) was studied in great detail as a part of this work. However, the data presented in this dissertation, with respect to nanoparticle distribution, was restricted to sub-micron level owing to the choice of characterization technique (i.e., confocal microscopy). A quantitative study of the differences in levels of homogeneity between negatively

charged DHLA-QDs and positively charged PEI-QDs in Ubx·QD composites at the nanoscale is of potential interest. Such a study would provide clues about the nature of interaction between nanoparticles (QDs) and Ubx monomers during initial stages of hierarchical self-assembly and help in design of polymeric macroscale composite biomaterials. This study would require STEM (scanning transmission electron microscopy) and EDS studies on Ubx·QD composites during and/or after the self-assembly process.

6.3.3 Optical sensing with Ubx·QD biomaterials

The synthesis and design aspects of composite Ubx·QD biomaterials presented in this work lead onwards to the use of these functional biomaterials as optical sensors. Given the high extensibility observed for Ubx materials,[125] luminescent QDs embedded in fluorescent EGFP-Ubx materials have a potential to be used as such FRET (Förster resonance energy transfer) sensors.

FRET is defined as a non-radiative transfer of excited-state energy from an initially excited donor to an acceptor.[140] In this, energy transfer occurs without the appearance of a photon and is the result of long-range dipole-dipole interactions between the donor and acceptor. The efficiency of energy transfer depends on the extent of spectral overlap, between the emission of the donor and absorbance of the acceptor, in addition to the relative orientation of donor-acceptor dipoles. These factors, for a given donor-acceptor pair, are represented by a Förster distance, R_o. An important characteristic of FRET is that the rate of energy transfer, κ_T, strongly depends on distance, r, between the donor and acceptor. This relationship is given as so:

$$\kappa_T = \frac{1}{\tau_D}\left(\frac{R_o}{r}\right)^6 \qquad \text{Equation 6.1}$$

where τ_D is the decay time of the donor in absence of the acceptor

Non-radiative energy transfer between photoluminescent quantum dots and fluorescent proteins has been previously shown to form the basis for sensor design.[26,27,122,141,142] From a device design aspect, changes in the PL of QDs or EGFP in response to extension/compression of EGFP-Ubx·QD fibers resulting due to non-radiative energy transfer between two luminescent species could serve as a motif for a stress/strain sensor.[143] Design of such experiments would require a customized optical system, as schematically represented in Figure 6.3, for excitation and PL detection from composite fibers mounted on a high precision piezo-stage such as a Gatan Microtest™ tensile tester to extend the fibers. The Gatan Microtest, a highly sensitive mechanical tester with a force sensitivity of 0.1 mN and displacement resolution of 0.001 mm, would be suitable for such experiments. The design of experiments for the proof of concept would involve detection in changes of QD PL and EGFP PL, upon UV excitation, in response to a constant stress applied to composite EGFP-Ubx·QD fibers. The high extensibilities shown by EGFP-Ubx·QD fibers in the course of these studies demonstrate the applicability of these materials as functionalizable optical sensors.

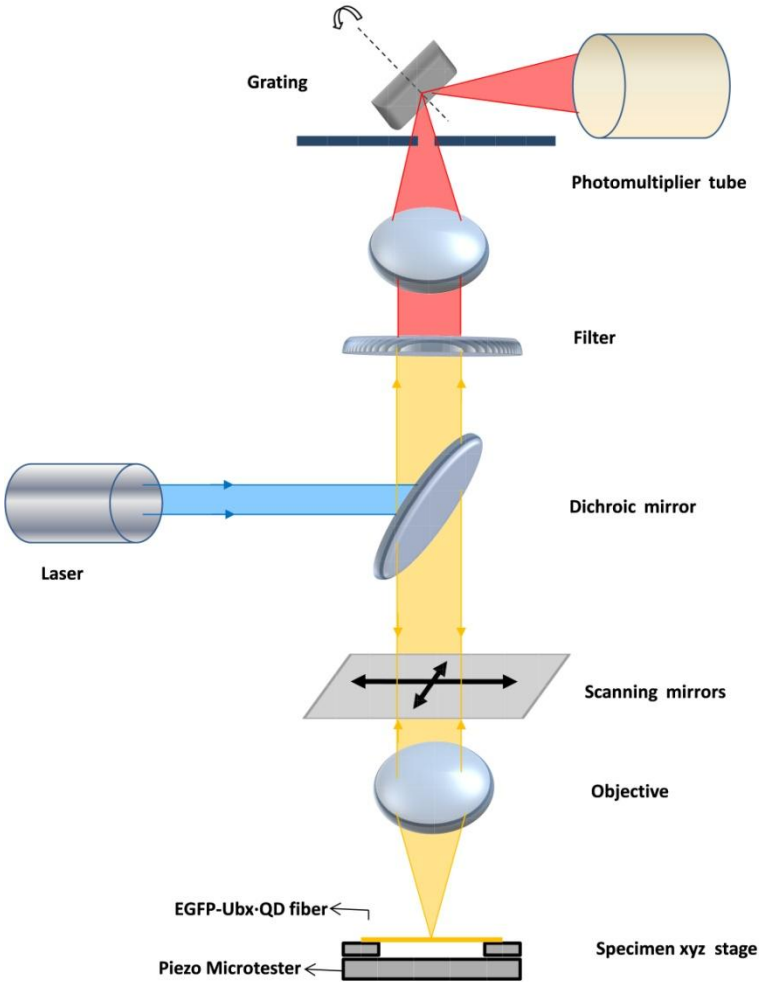

Figure 6.3 A schematic showing optical setup for proof of concept study for the use of EGFP-Ubx·QD fibers as optical FRET sensors.

REFERENCES

[1] J. I. Gersten, F. W. Smith, *The Physics and Chemistry of Materials*, John Wiley & Sons, New York 2001.

[2] C. Kittel, *Introduction to Solid State Physics*, John Wiley & Sons, Hoboken, NJ 2005.

[3] A. B. Denison, L. J. Hop-Weeks, R. W. Meulenberg, in *Introduction to Nanoscale Science and Technology*, Vol. 6 (Eds: M. Di Ventra, S. Evoy, J. R. Heflin Jr), Springer, 2004, 183-198.

[4] A. P. Alivisatos, *Science* **1996**, *271*, 933-937.

[5] V. I. Klimov, *Los Alamos Science* **2003**, *28*, 214-220.

[6] L. Brus, *Quantum Electronics, IEEE Journal of* **1986**, *22*, 1909-1914.

[7] A. B. Djurišic , Y. H. Leung, *Small* **2006**, *2*, 944-961.

[8] Z. L. Wang, *Adv. Funct. Mater.* **2008**, *18*, 3553-3567.

[9] C. B. Murray, D. J. Norris, M. G. Bawendi, *J. Am. Chem. Soc.* **1993**, *115*, 8706-8715.

[10] X. Peng, J. Wickham, A. P. Alivisatos, *J. Am. Chem. Soc.* **1998**, *120*, 5343-5344.

[11] Z. A. Peng, X. Peng, *J. Am. Chem. Soc.* **2000**, *123*, 183-184.

[12] M. A. Verges, A. Mifsud, C. J. Serna, *J. Chem. Soc., Faraday Trans.* **1990**, *86*, 959.

[13] L. Vayssieres, *Adv. Mater.* **2003**, *15*, 464-466.

[14] L. E. Greene, M. Law, J. Goldberger, F. Kim, J. C. Johnson, Y. Zhang, R. J. Saykally, P. Yang, *Angew. Chem. Int. Ed.* **2003**, *42*, 3031-3034.

[15] L. E. Greene, B. D. Yuhas, M. Law, D. Zitoun, P. Yang, *Inorg. Chem.* **2006**, *45*, 7535-7543.

[16] L. Schmidt-Mende, J. L. MacManus-Driscoll, *Mater. Today* **2007**, *10*, 40-48.

[17] B. Weintraub, Z. Zhou, Y. Li, Y. Deng, *Nanoscale* **2010**, *2*, 1573.

[18] Q. Wan, Q. H. Li, Y. J. Chen, T. H. Wang, X. L. He, J. P. Li, C. L. Lin, *Appl. Phys. Lett.* **2004**, *84*, 3654-3656.

[19] J. Zhou, Y. Gu, Y. Hu, W. Mai, P. H. Yeh, G. Bao, A. K. Sood, D. L. Polla, Z. L. Wang, *Appl. Phys. Lett.* **2009**, *94*, 191103.

[20] Z. L. Wang, *Adv. Mater.* **2007**, *19*, 889-892.

[21] B. Weintraub, Y. Wei, Z. L. Wang, *Angew. Chem. Int. Ed.* **2009**, *48*, 8981-8985.

[22] R. C. Somers, M. G. Bawendi, D. G. Nocera, *Chem. Soc. Rev.* **2007**, *36*, 579.

[23] K. E. Sapsford, T. Pons, I. L. Medintz, H. Mattoussi, *Sensors* **2006**, *6*, 925-953.

[24] W. C. Chan, *Science* **1998**, *281*, 2016-2018.

[25] M. Han, X. Gao, J. Z. Su, S. Nie, *Nat. Biotechnol.* **2001**, *19*, 631-635.

[26] H. Mattoussi, J. M. Mauro, E. R. Goldman, G. P. Anderson, V. C. Sundar, F. V. Mikulec, M. G. Bawendi, *J. Am. Chem. Soc.* **2000**, *122*, 12142-12150.

[27] I. L. Medintz, H. T. Uyeda, E. R. Goldman, H. Mattoussi, *Nat. Mater.* **2005**, *4*, 435-446.

[28] L. Vayssieres, K. Keis, S.-E. Lindquist, A. Hagfeldt, *J. Phys. Chem. B* **2001**, *105*, 3350-3352.

[29] L. Nicholas, C. McGowan, *Clean, Fast Organic Chemistry: Microwave-assisted Laboratory Experiments*, CEM Publisihing, 2006.

[30] J. A. Gerbec, D. Magana, A. Washington, G. F. Strouse, *J. Am. Chem. Soc.* **2005**, *127*, 15791-15800.

[31] Z. L. Wang, *Mater. Today* **2004**, *7*, 26-33.

[32] U. Özgür, Y. I. Alivov, C. Liu, A. Teke, M. A. Reshchikov, S. Doğan, V. Avrutin, S. J. Cho, H. Morkoç, *J. Appl. Phys.* **2005**, *98*, 041301.

[33] A. B. Djurišić, Y. H. Leung, *Small* **2006**, *2*, 944-961.

[34] A. B. Djurišić, X. Chen, Y. H. Leung, A. M. C. Ng, *J. Mater. Chem.* **2012**, *22*, 6526-6535.

[35] X. Wang, J. Song, J. Liu, Z. L. Wang, *Science* **2007**, *316*, 102-105.

[36] M. McCune, W. Zhang, Y. Deng, *Nano Lett.* **2012**, *12*, 3656-3662.

[37] Ü. Özgür, Y. I. Alivov, C. Liu, A. Teke, M. Reshchikov, S. Do an, V. Avrutin, S. J. Cho, H. Morkoc, *J. Appl. Phys.* **2005**, *98*, 041301.

[38] L. Wischmeier, T. Voss, S. Börner, W. Schade, *Appl. Phys. A: Mater. Sci. Process.* **2006**, *84*, 111-116.

[39] L. Wischmeier, T. Voss, I. Rückmann, J. Gutowski, A. Mofor, A. Bakin, A. Waag, *Physical Review B* **2006**, *74*, 195333.

[40] L. Liao, H. B. Lu, J. C. Li, H. He, D. F. Wang, D. J. Fu, C. Liu, W. F. Zhang, *The Journal of Physical Chemistry C* **2007**, *111*, 1900-1903.

[41] D. Stichtenoth, C. Ronning, T. Niermann, L. Wischmeier, T. Voss, C. J. Chien, P. C. Chang, J. G. Lu, *Nanotechnology* **2007**, *18*, 435701.

[42] Z. W. Pan, *Science* **2001**, *291*, 1947-1949.

[43] X. W. Xudong Wang, C. J. Summers, Z. L. Wang, *Nano Lett.* **2004**, *4*, 423-426.

[44] Y. Li, G. W. Meng, L. D. Zhang, F. Phillipp, *Appl. Phys. Lett.* **2000**, *76*.

[45] Z. R. Tian, J. A. Voigt, J. Liu, B. McKenzie, M. J. McDermott, M. A. Rodriguez, H. Konishi, H. Xu, *Nature Materials* **2003**, *2*, 821-826.

[46] S. Xu, Z. L. Wang, *Nano Res.* **2011**, *4*, 1013-1098.

[47] X. M. Sun, X. Chen, Z. X. Deng, Y. D. Li, *Mater. Chem. Phys.* **2003**, *78*, 99-104.

[48] X. Gao, X. Li, W. Yu, *J. Phys. Chem. B* **2005**, *109*, 1155-1161.

[49] K. Govender, D. S. Boyle, P. B. Kenway, P. O'Brien, *J. Mater. Chem.* **2004**, *14*, 2575-2591.

[50] M. Ashfold, R. Doherty, N. Ndiforangwafor, D. Riley, Y. Sun, *Thin Solid Films* **2007**, *515*, 8679-8683.

[51] B. Liu, H. C. Zeng, *J. Am. Chem. Soc.* **2003**, *125*, 4430-4431.

[52] D. W. Bahnemann, C. Kormann, M. R. Hoffmann, *J. Phys. Chem.* **1987**, *91*, 3789-3798.

[53] C. Pacholski, A. Kornowski, H. Weller, *Angew. Chem. Int. Ed.* **2002**, *41*, 1188-1191.

[54] J. F. Banfield, S. A. Welch, H. Zhang, T. T. Ebert, R. L. Penn, *Science* **2000**, *289*, 751-754.

[55] A. Chemseddine, T. Moritz, *Eur. J. Inorg. Chem.* **1999**, *1999*, 235-245.

[56] R. A. McBride, J. M. Kelly, D. E. McCormack, *J. Mater. Chem.* **2003**, *13*, 1196-1201.

[57] K. Elen, H. Van den Rul, A. Hardy, M. K. Van Bael, J. D'Haen, R. Peeters, D. Franco, J. Mullens, *Nanotechnology* **2009**, *20*, 055608.

[58] A. Aimable, M. T. Buscaglia, V. Buscaglia, P. Bowen, *J. Eur. Ceram. Soc.* **2010**, *30*, 591-598.

[59] K. Lu, J. Zhao, *Chem. Eng. J.* **2010**, *160*, 788-793.

[60] A. P. A. Oliveira, J.-F. Hochepied, F. Grillon, M.-H. Berger, *Chem. Mater.* **2003**, *15*, 3202-3207.

[61] S. Mridha, D. Basak, *physica status solidi (a)* **2009**, *206*, 1515-1519.

[62] Y. Sun, R. Zou, Q. Tian, J. Wu, Z. Chen, J. Hu, *CrystEngComm* **2011**, *13*, 2273-2280.

[63] K. H. Tam, C. K. Cheung, Y. H. Leung, A. B. Djurišić, C. C. Ling, C. D. Beling, S. Fung, W. M. Kwok, W. K. Chan, D. L. Phillips, L. Ding, W. K. Ge, *J. Phys. Chem. B* **2006**, *110*, 20865-20871.

[64] J. Goldstein, D. E. Newbury, D. C. Joy, C. E. Lyman, P. Echlin, E. Lifshin, L. Sawyer, J. R. Michael, *Scanning Electron Microscopy and X-ray Microanalysis*, Springer, 2003.

[65] Z. Li, Y. Khimyak, A. Taubert, *Materials* **2008**, *1*, 3-24.

[66] L. M. Cook, *J. Non-Cryst. Solids* **1990**, *120*, 152-171.

[67] R. K. Iler, *Chemistry of Silica - Solubility, Polymerization, Colloid and Surface Properties and Biochemistry*, John Wiley & Sons, 1979.

[68] B. Liu, H. C. Zeng, *Langmuir* **2004**, *20*, 4196-4204.

[69] R. T. Senger, K. K. Bajaj, *Physical Review B* **2003**, *68*, 045313.

[70] Y. Gu, I. L. Kuskovsky, M. Yin, S. O'Brien, G. Neumark, *Appl. Phys. Lett.* **2004**, *85*, 3833.

[71] N. S. Pesika, K. J. Stebe, P. C. Searson, *Adv. Mater.* **2003**, *15*, 1289-1291.

[72] N. S. Pesika, K. J. Stebe, P. C. Searson, *J. Phys. Chem. B* **2003**, *107*, 10412-10415.

[73] Y. Lv, L. Guo, H. Xu, L. Ding, C. Yang, J. Wang, W. Ge, S. Yang, Z. Wu, *J. Appl. Phys.* **2006**, *99*, 114302.

[74] B. Meyer, H. Alves, D. Hofmann, W. Kriegseis, D. Forster, F. Bertram, J. Christen, A. Hoffmann, M. Straßburg, M. Dworzak, *physica status solidi (b)* **2004**, *241*, 231-260.

[75] V. Travnikov, A. Freiberg, S. Savikhin, *J. Lumin.* **1990**, *47*, 107-112.

[76] J. Grabowska, A. Meaney, K. Nanda, J. P. Mosnier, M. O. Henry, J. R. Duclère, E. McGlynn, *Physical Review B* **2005**, *71*, 115439.

[77] A. van Dijken, E. A. Meulenkamp, D. Vanmaekelbergh, A. Meijerink, *J. Phys. Chem. B* **2000**, *104*, 1715-1723.

[78] Y. Chen, Q. Qiao, Y. Liu, G. Yang, *The Journal of Physical Chemistry C* **2009**, *113*, 7497-7502.

[79] L. Spanhel, M. A. Anderson, *J. Am. Chem. Soc.* **1991**, *113*, 2826-2833.

[80] M. Haase, H. Weller, A. Henglein, *J. Phys. Chem.* **1988**, *92*, 482-487.

[81] B. D. Cullity, S. R. Stock, *Elements of X-ray Diffraction*, Vol. 3, Prentice hall Upper Saddle River, NJ, 2001.

[82] W. Zhong Lin, *J. Phys.: Condens. Matter* **2004**, *16*, R829.

[83] H. J. Fan, R. Scholz, F. M. Kolb, M. Zacharias, *Appl. Phys. Lett.* **2004**, *85*, 4142-4144.

[84] A. B. Djurišić, Y. H. Leung, K. H. Tam, Y. F. Hsu, L. Ding, W. K. Ge, Y. C. Zhong, K. S. Wong, W. K. Chan, H. L. Tam, K. W. Cheah, W. M. Kwok, D. L. Phillips, *Nanotechnology* **2007**, *18*, 095702.

[85] K. J. Choi, H. W. Jang, *Sensors* **2010**, *10*, 4083-4099.

[86] A. Wei, L. Pan, W. Huang, *Materials Science and Engineering: B* **2011**, *176*, 1409-1421.

[87] P. Feng, Q. Wan, T. H. Wang, *Appl. Phys. Lett.* **2005**, *87*, 213111-213113.

[88] A. Kolmakov, M. Moskovits, *Annu. Rev. Mater. Res.* **2004**, *34*, 151-180.

[89] C. C. Li, Z. F. Du, L. M. Li, H. C. Yu, Q. Wan, T. H. Wang, *Appl. Phys. Lett.* **2007**, *91*, 032101.

[90] T. Gao, T. H. Wang, *Appl. Phys. A: Mater. Sci. Process.* **2005**, *80*, 1451-1454.

[91] A. Creti, D. Valerini, A. Taurino, F. Quaranta, M. Lomascolo, R. Rella, *J. Appl. Phys.* **2012**, *111*, 073520.

[92] D. Valerini, A. Cretì, A. P. Caricato, M. Lomascolo, R. Rella, M. Martino, *Sensors and Actuators B: Chemical* **2010**, *145*, 167-173.

[93] C. Baratto, S. Todros, G. Faglia, E. Comini, G. Sberveglieri, S. Lettieri, L. Santamaria, P. Maddalena, *Sensors and Actuators B: Chemical* **2009**, *140*, 461-466.

[94] E. Comini, C. Baratto, G. Faglia, M. Ferroni, G. Sberveglieri, *J. Phys. D: Appl. Phys.* **2007**, *40*, 7255.

[95] O. L. Stroyuk, V. M. Dzhagan, V. V. Shvalagin, S. Y. Kuchmiy, *The Journal of Physical Chemistry C* **2009**, *114*, 220-225.

[96] Z. A. Peng, X. Peng, *J. Am. Chem. Soc.* **2001**, *123*, 1389-1395.

[97] Z. A. Peng, X. Peng, *J. Am. Chem. Soc.* **2002**, *124*, 3343-3353.

[98] X. Peng, *Adv. Mater.* **2003**, *15*, 459-463.

[99] D. V. Talapin, A. L. Rogach, A. Kornowski, M. Haase, H. Weller, *Nano Lett.* **2001**, *1*, 207-211.

[100] I. Mekis, D. V. Talapin, A. Kornowski, M. Haase, H. Weller, *J. Phys. Chem. B* **2003**, *107*, 7454-7462.

[101] L. Qu, Z. A. Peng, X. Peng, *Nano Lett.* **2001**, *1*, 333-337.

[102] B. Dickerson, D. Irving, E. Herz, R. Claus, W. Spillman, K. Meissner, *Appl. Phys. Lett.* **2005**, *86*, 171915-171915-171913.

[103] W. W. Yu, X. Peng, *Angew. Chem. Int. Ed.* **2002**, *41*, 2368-2371.

[104] C. R. Bullen, P. Mulvaney, *Nano Lett.* **2004**, *4*, 2303-2307.

[105] B. Pan, R. He, F. Gao, D. Cui, Y. Zhang, *J. Cryst. Growth* **2006**, *286*, 318-323.

[106] Q. Dai, S. Kan, D. Li, S. Jiang, H. Chen, M. Zhang, S. Gao, Y. Nie, H. Lu, Q. Qu, G. Zou, *Mater. Lett.* **2006**, *60*, 2925-2928.

[107] X. Peng, L. Manna, W. Yang, J. Wickham, E. Scher, A. Kadavanich, A. P. Alivisatos, *Nature* **2000**, *404*, 59-61.

[108] R. Majithia, K. E. Meissner, "One pot microwave assisted synthesis of CdTe/ZnS quantum dots emitting in the Near-IR region", presented at *26th Annual Houston Conference on Biomedical Engineering Research (HSEMB)*, Houston, March 19, 2009.

[109] B. O. Dabbousi, J. Rodriguez-Viejo, F. V. Mikulec, J. R. Heine, H. Mattoussi, R. Ober, K. F. Jensen, M. G. Bawendi, *J. Phys. Chem. B* **1997**, *101*, 9463-9475.

[110] M. A. Hines, P. Guyot-Sionnest, *J. Phys. Chem.* **1996**, *100*, 468-471.

[111] J. Ziegler, A. Merkulov, M. Grabolle, U. Resch-Genger, T. Nann, *Langmuir* **2007**, *23*, 7751-7759.

[112] A. L. Washington, G. F. Strouse, *Chem. Mater.* **2009**, *21*, 2770-2776.

[113] A. R. Juriani, in *Department of Biomedical Engineering*, Vol. Master of Science, Texas A&M University College Station 2010, 60.

[114] A. Romoser, D. Ritter, R. Majitha, K. E. Meissner, M. McShane, C. M. Sayes, *PLoS One* **2011**, *6*, e22079.

[115] R. Majithia, J. Patterson, S. E. Bondos, K. E. Meissner, *Biomacromolecules* **2011**, *12*, 3629-3637.

[116] R. A. Velapoldi, H. H. Tønnesen, *J. Fluoresc.* **2004**, *14*, 465-472.

[117] R. Weissleder, *Nat Biotech* **2001**, *19*, 316-317.

[118] H. Seo, S. Kim, *Bulletin-Korean Chemical Society* **2007**, *28*, 1637.

[119] W. W. Yu, Y. A. Wang, X. Peng, *Chem. Mater.* **2003**, *15*, 4300-4308.

[120] J. Li, X. Hong, Y. Liu, D. Li, Y. W. Wang, J. H. Li, Y. B. Bai, T. J. Li, *Adv. Mater.* **2005**, *17*, 163-166.

[121] W. C. W. Chan, S. Nie, *Science* **1998**, *281*, 2016.

[122] C. M. Niemeyer, *Angew. Chem. Int. Ed.* **2003**, *42*, 5796-5800.

[123] Z. Huang, T. Salim, A. Brawley, J. Patterson, K. S. Matthews, S. E. Bondos, *Adv. Funct. Mater.* **2011**, *21*, 2633-2640.

[124] A. M. Greer, Z. Huang, A. Oriakhi, Y. Lu, J. Lou, K. S. Matthews, S. E. Bondos, *Biomacromolecules* **2009**, *10*, 829-837.

[125] Z. Huang, Y. Lu, R. Majithia, J. Shah, K. Meissner, K. S. Matthews, S. E. Bondos, J. Lou, *Biomacromolecules* **2010**, *11*, 3644-3651.

[126] C. L. Hughes, T. C. Kaufman, *Evol. Dev.* **2002**, *4*, 459-499.

[127] Y. Liu, K. S. Matthews, S. E. Bondos, *J. Biol. Chem.* **2008**, *283*, 20874-20887.

[128] W. J. Landis, M. C. Paine, M. J. Glimcher, *Journal of Ultrastructure Research* **1980**, *70*, 171-180.

[129] M. Grote, *J. Histochem. Cytochem.* **1991**, *39*, 1395-1401.

[130] T. Cedervall, I. Lynch, S. Lindman, T. Berggård, E. Thulin, H. Nilsson, K. A. Dawson, S. Linse, *Proc. Natl. Acad. Sci. U. S. A.* **2007**, *104*, 2050.

[131] L. F. Drummy, H. Koerner, D. M. Phillips, J. C. McAuliffe, M. Kumar, B. L. Farmer, R. A. Vaia, R. R. Naik, *Mater. Sci. Eng., C* **2009**, *29*, 1266-1272.

[132] J. Klein, *Proc. Natl. Acad. Sci. U. S. A.* **2007**, *104*, 2029-2030.

[133] M. Lundqvist, J. Stigler, G. Elia, I. Lynch, T. Cedervall, K. A. Dawson, *Proc. Natl. Acad. Sci. U. S. A.* **2008**, *105*, 14265-14270.

[134] I. Lynch, K. A. Dawson, *Nano Today* **2008**, *3*, 40-47.

[135] T. Nann, *Chem. Commun.* **2005**, 1735-1736.

[136] A. R. Clapp, E. R. Goldman, H. Mattoussi, *Nat. Protocols* **2006**, *1*, 1258-1266.

[137] W. W. Yu, L. Qu, W. Guo, X. Peng, *Chem. Mater.* **2003**, *15*, 2854-2860.

[138] T. Pons, H. T. Uyeda, I. L. Medintz, H. Mattoussi, *J. Phys. Chem. B* **2006**, *110*, 20308-20316.

[139] Z. Shao, R. J. Young, F. Vollrath, *Int. J. Biol. Macromol.* **1999**, *24*, 295-300.

[140] J. R. Lakowicz, *Principles of Fluorescence Spectroscopy*, Vol. 1, Springer, 2006.

[141] A. R. Clapp, I. L. Medintz, J. M. Mauro, B. R. Fisher, M. G. Bawendi, H. Mattoussi, *J. Am. Chem. Soc.* **2003**, *126*, 301-310.

[142] A. M. Dennis, G. Bao, *Nano Lett.* **2008**, *8*, 1439-1445.

[143] R. Majithia, J. A. Jamison, J. Patterson, S. Ritter, M. Holmes, S. E. Bondos, K. E. Meissner, "Optical Biosensor based on Protein-Nanoparticle Composite Biomaterials: An Analysis", presented at *Biomedical Engineering Society Meeting*, Austin, October,2010.

APPENDIXES

Appendix A: Estimated values of zinc oxide nanoparticle diameter as a function of absorption onset using Effective mass model calculations

ZnO Nanoparticle Radius (nm)	Absorption onset (nm)
0.5	113.5996
0.6	146.3394
0.7	176.8329
0.8	204.2418
0.9	228.3155
1	249.1576
1.1	267.0525
1.2	282.3538
1.3	295.4213
1.4	306.589
1.5	316.1523
1.6	324.3651
1.7	331.4419
1.8	337.562
1.9	342.8752
2	347.5055
2.1	351.5562
2.2	355.1131
2.3	358.2479
2.4	361.0202
2.5	363.4803
2.6	365.6704
2.7	367.6262
2.8	369.3779
2.9	370.9511
3	372.368
3.1	373.6472
3.2	374.8049
3.3	375.8551

ZnO Nanoparticle Radius (nm)	Absorption onset (nm)
3.4	376.8099
3.5	377.6798
3.6	378.4738
3.7	379.2
3.8	379.8654
3.9	380.4761
4	381.0375
4.1	381.5544
4.2	382.0311
4.3	382.4713
4.4	382.8784
4.5	383.2553
4.6	383.6048
4.7	383.9291
4.8	384.2305
4.9	384.5109
5	384.772

Appendix B

Ubx Sequence: Homeodomain underlined

MNSYFEQASGFYGHPHQATGMAMGSGGHHDQTASAAAAAYRGFPLSL
GMSPYANHHLQRTTQDSPYDASITAACNKIYGDGAGAYKQDCLNIKADAVNG
YKDIWNTGGSNGGGGGGGGGGGGAGGTGGAGNANGGNAANANGQNNPAG
GMPVRPSACTPDSRVGGYLDTSGGSPVSHRGGSAGGNVSVSGGNGNAGGVQS
GVGVAGAGTAWNANCTISGAAAQTAAASSLHQASNHTFYPWMAIAGKIRSDLT
QYGGISTDMGKRYSESLAGSLLPDWLGTNGLRRRGRQTYTRYQTLELEKEFHT
NHYLTRRRRIEMAHALCLTERQIKIWFQNRRMKLKKEIQAIKELNEQEKQAQAQ
KAAAAAAAAAAVQGGHLDQ